INVESTIGATION OF TOOL WEAR IN DIAMOND TURNING OF CU-NI ALLOYS USING SINGLE CRYSTAL DIAMOND TOOLS

by

Alex Blum

A dissertation submitted to the faculty of
The University of North Carolina at Charlotte
in partial fulfillment of the requirements
for the degree of Doctor of Philosophy in
Mechanical Engineering

Charlotte

2020

Approved by:

_____
Dr. Chris Evans

_____
Dr. Matthew Davies

_____
Dr. Angela Davies Allen

_____
Dr. John Taylor

_____
Dr. Yongge Wang

ABSTRACT

ALEX BLUM. Investigation of tool wear in diamond turning of Cu-Ni alloys using single crystal diamond tools. (Under the direction of DR. CHRIS EVANS)

Goods manufactured using single point diamond turning (SPDT) are commonplace in everyday life in products from cell phones to street signs. Diamond turning is the process of using single crystal diamond (SCD) tools mounted on extremely precise machine tools to manufacture optical surfaces. The use of diamond tools to manufacture diffraction gratings dates back more than a century, but modern diamond turning was first used in the 1940s to manufacture infrared optics. In the 1960s manufacturing expanded into components such as laser optics, parabolic reflectors, and electron microscope parts. Since then, both private and publicly funded research and development has continued to expand to the materials available, and manufacturing techniques used to diamond turn parts. As the search for new materials and processes continues tool wear is a constant concern. Despite the broad array of available measurement techniques and substantial body of literature on the subject, there are still gaps in both the theory of diamond tool wear and experimental validation of that theory. The research presented here consists of three experiments: investigation of the relationship between wear and oxygen partial pressure, measurement of chemical activation energy, and investigation of tool wear as a function of crystallographic orientation. An uncertainty analysis of the measurement method used is also presented. The goal of this work is to improve the model of chemical wear in SPDT of metal alloys.

DEDICATION

This dissertation is dedicated to my wife, Elisabeth, and my dogs, Punky and Zoey, whom collectively dragged me across the finish line.

ACKNOWLEDGEMENTS

This dissertation would not have been possible without Chris Evans and innate ability to provoke thoughtful analysis, John Taylor for making sure I left no stone unturned, and Ed Paul and Tom Childs for their guidance and tutelage in data analysis. I would also like to thank Harish Cherukuri, Jimmy Miller, Brian Dutterer, and many others for their help and guidance. You all gave important, unique insights and assistance that were fundamental to the completion of this research.

Supported in part by NSF grant 530602.

TABLE OF CONTENTS

LIST OF TABLES x

LIST OF FIGURES xi

LIST OF ABBREVIATIONS 1

CHAPTER 1: INTRODUCTION 3

1.1. Diamond turning and optics manufacturing 3

1.2. Measurement of wear in single crystal diamond cutting tools 7

CHAPTER 2: BACKGROUND 10

2.1. Physics of single crystal diamond tool wear 10

2.2. Measurement and characterization of chemical wear in single crystal diamond tools 12

2.3. Proposed model for anisotropy of chemical wear rates 15

CHAPTER 3: PLUNGE CUT RESIDUAL MEASUREMENT METHOD 18

3.1. Overview of diamond tool wear measurement 18

3.2. Basic experimental setup and process 20

3.3. Plunge measurement and preliminary processing 22

3.4. Final plunge alignment and residual calculation 23

3.4.1. Slope alignment method 23

3.4.2. Sag equation alignment method 26

3.4.3. Residual calculation 27

CHAPTER 4: MEASUREMENT UNCERTAINTY AND OUTLIER ROOT-CAUSE ANALYSIS FOR PLUNGE CUT RESIDUAL MEASUREMENTS 29

4.1. Horizontal resolution limits of the coherence scanning interferometer 30

4.2. Surface topography repeatability of interferometer 32

4.3. Monte Carlo uncertainty analysis of plunge cut residual measurements 34

4.3.1. Input distributions for Monte Carlo uncertaintuy analysis of cutting edge measurement 36

4.3.2. High frequency surface feature near plunge edge 37

4.3.3. Results of Monte Carlo analysis 38

4.3.4. Discussion of measurement uncertainty results 39

4.4. Investigation of experimental outliers 40

CHAPTER 5: CUTTING FORCES WHEN DIAMOND TURNING CU-NI ALLOYS 43

5.1. Cutting mechanics and force model for diamond turning metals 43

5.2. Collection of cutting force data 45

5.3. Processing of cutting force data 46

5.4. Measurement of thrust and cutting force with tool normal to workpiece 48

5.5. Investigation of the relationship between wear rates, cutting force, and edge sharpness 48

5.6. Discussion of cutting force data 59

CHAPTER 6: DIAMOND EDGE RECESSION AS A FUNCTION OF CUTTING DISTANCE 60

6.1. Expected relationship between wear and cutting distance 60

6.2. Analysis of nose and leading edge wear as a function of cutting distance 61

6.3. Discussion of edge recession analysis 63

CHAPTER 7: DIAMOND TOOL WEAR AS A FUNCTION OF CRYSTALLOGRAPHIC ORIENTATION 66

7.1. Literature review for anisotropy of diamond tool wear 66

7.2. Crater wear and crystal orientation 66

7.3. Edge recession and crystal orientation 70

7.4. Discussion of angular orientation experiment results 79

CHAPTER 8: DIAMOND TOOL WEAR AS A FUNCTION OF OXYGEN PARTIAL PRESSURE 81

8.1. Historical research on wear and gaseous environment 81

8.2. Experimental setup, data collection and processing 82

8.3. Collection and analysis of data 83

8.4. Discussion of wear rates and oxygen partial pressure 86

8.4.1. Elevated enclosure temperatures and Joule-Thomson cooling 88

8.4.2. Langmuir surfaces and wear rates 90

CHAPTER 9: CONCLUSIONS 92

CHAPTER 10: FUTURE WORK: PROPOSED TOOL WEAR CHARACTERIZATION EXPERIMENTS 95

10.1.Measurement of activation energy 95

10.2.Measurement of temperatures at the cutting interface 96

10.3.Improved characterization of edge recession 97

REFERENCES 99

APPENDIX A: MATLAB CODE 105

A.1. Script for plunge processing 105

A.2. Script for Monte Carlo analysis 106

A.3. Class for surface data type and manipulation methods 108

A.4. Class for Monte Carlo methods 110

A.5. Class for plunge processing methods 113

APPENDIX B: EXPERIMENTAL PROCEDURE 119

APPENDIX C: CNC CODE 120

APPENDIX D: SENSORS AND DATA ACQUISITION 122

LIST OF TABLES

TABLE 1.1: Tool wear measurement techniques 8

TABLE 3.1: Standard parameters for tool wear experiments 21

TABLE 4.1: Table of input distributions for Monte Carlo simulation 37

TABLE D.1: Table of sensors used during experiments and their properties. 122

LIST OF FIGURES

FIGURE 1.1: Single crystal diamond tool facing a Monel workpiece. 4

FIGURE 2.1: Reaction coordinate diagram for metal-carbon and metal-oxygen-carbon pathways [1]. 14

FIGURE 2.2: Relationship between bond density and orientation. At 0 degrees the tool is normal to the workpiece and the $< 100 >$ direction on diamond blank is also normal to the workpiece. Theta is the angle between $< 100 >$ on the diamond blank and the workpiece's normal vector. 17

FIGURE 3.1: Illustration of coordinate system and sign convention for tool rotation with respect to workpiece normal. 20

FIGURE 3.2: Layout for experimental setup (plan view). 21

FIGURE 3.3: Measuring the plunges from an experiment. This ring contains six separate experiments, each with six plunges. 22

FIGURE 3.4: Rotating the height map to correct misalignment. The two dots represent the plunge edge located by the edge finding algorithm. Since the vertical and horizontal distance between the points in pixels is known, θ can be calculated. 23

FIGURE 3.5: Column averaged plunge phasemaps, before and after final alignment. 24

FIGURE 3.6: Shifting and subtracting plunges to create residuals. Angle of the residual increses with greater pixel shift. 24

FIGURE 3.7: Relationship between pixel shift and residual slope. 26

FIGURE 3.8: Schematic description of the sag alignment process. Starting at z_0, x_{dist} is compared to f. z_0 is incremented down until x_{dist} is less than f, at which point the plunge is trimmed. 27

FIGURE 3.9: Typical residual obtained by subtracting a best-fit circle from the column averaged, aligned plunge data. 28

FIGURE 4.1: Pointwise standard deviation of twenty repeat measurements of one plunge, taken at ten second intervals. 33

FIGURE 4.2: Surface topography repeatability of a typical plunge measurement. The spikes around ± 100 µm indicate the plunge edges. 34

FIGURE 4.3: 1. Seed measurement used to create distribution of inputs, 2. Add piston, tilt, rotation, and shift, with the amount of each pseudo-randomly drawn from it's respective statistical distribution, take residual of each of these with respect to the seed measurement, 3. Find pointwise standard deviation of all residuals. 36

FIGURE 4.4: Profile from 50x measurement of a plunge where a burr was present on the plunge edge. Both the burr and the material bunching up below can be seen. 38

FIGURE 4.5: Results of Monte Carlo uncertainty evaluation ($k = 2$). 39

FIGURE 4.6: Example of alignment quality with real data from an experiment. This tool has a 'rough' edge but aligns to 30 nm or better. 40

FIGURE 4.7: Side view of diamond. Cutting edge sharpness refers to the nanometer-scale radius of the cutting edge emphasized by the black circle. 41

FIGURE 4.8: The first (unworn) plunge from an experimental data set and the corresponding edge recession measurements. The tool was normal to the workpiece for this experiment. A large piece missing from the trailing edge appears to have not caused excessively high edge recession, but does make decent final alignment impossible. 42

FIGURE 4.9: The results of repeating the experiment, using the same tool shown in Figure 4.8, after being relapped and reconed. There is still error visible, but it is on the order of 10 nm. 42

FIGURE 5.1: Cutting mechanics of single point diamond turning [2] and coordinate system for cutting (F_y), thrust (F_z), and feed (F_x) forces. 44

FIGURE 5.2: Uncut chip thickness increases with θ. 45

FIGURE 5.3: Setup for force measurement. The dynamometer is inserted into the tool post structural loop using an adapter plate. The tool is also clamped from the top and side. 46

FIGURE 5.4: Typical plunge cut force measurement before drift correction and the associated drift correction process. The drift is *not* linear over long δt. Each plunge only lasts for three seconds so the problem is minimal, but must be considered. 49

FIGURE 5.5: The first and final facing passes from Figure 5.6a, before filtering, and the power spectrum associated with each. The low-frequency peaks may be associated with noise in the spindle drive current. 50

FIGURE 5.6: Typical thrust and cutting forces when facing Monel at 5 µm depth of cut and a feed rate of 2 µm/rev. 51

FIGURE 5.7: Absolute value of average cutting and average thrust force for each facing pass from Figure 5.6. Absolute value is used so that the rate trends can be compared on the same plot. Each data point represents the average from two to four seconds. 52

FIGURE 5.8: Typical thrust and cutting forces when plunging into UBAC copper at 50 nm/rev. 53

FIGURE 5.9: Absolute value of peak cutting and peak thrust force for each plunge from Figure 5.8. Absolute value is used so that the rate trends can be compared on the same plot. Each data point represents largest force value recorded during each plunge. 54

FIGURE 5.10: Tool wear residual from the experiment where the force data in Figures 5.6 through 5.9 was recorded. 55

FIGURE 5.11: AFM measurement used to measure cutting edge radius. 55

FIGURE 5.12: Profile of cutting edge from previous figure. 56

FIGURE 5.13: SEM measurement of the unworn cutting edge. There is a defect in the middle of the field of view. 56

FIGURE 5.14: SEM measurements of the worn cutting edge. Leading edge wear is to the left, and nose wear is to the right. 57

FIGURE 5.15: Peak cutting and thrust forces when plunging into copper as a function of cutting distance, from Figure 5.10. 57

FIGURE 5.16: Plots of the relationship between cutting edge recession and measured forces. 58

FIGURE 5.17: Residual for experiment described in this section. 58

FIGURE 6.1: Nose recession on the final cutting pass for various Cu-Ni alloys, adapted from Browy [3]. For Cu-Ni alloys, the relationship between recession and d-index is extremely nonlinear. The inset shows the relationship between nose recession and nickel content below 64.6% Ni. 60

FIGURE 6.2: As the uncut chip thickness increases, higher cutting forces lead to more work performed and higher local temperatures. This causes higher local wear rates as the chip thickness increases. 62

FIGURE 6.3: Residual from Figure 3.9, after filtering, with locations along the cutting edge where wear rates will be calculated marked. 63

FIGURE 6.4: Edge recession and edge recession rates at x_{1e} through x_{4e}. 64

FIGURE 6.5: Nose recession and nose recession rates at x_n. 64

FIGURE 7.1: Crystal lattice geometry for the diamond tools used in these experiments. 67

FIGURE 7.2: Custom tools with the diamond blank brazes on at an angle. 67

FIGURE 7.3: Typical measurement of the rake face. This measurement is of a tool rotated to 15 degrees. 68

FIGURE 7.4: Cropped and filtered interferograms of the rake face crater after six experiments at a variety of angles. Crater depth for the first two measurements is significantly greater than for the final four, so the first two are presented on their own z scales. All others are on a matching z scale. 69

FIGURE 7.5: Volume of material removed from the rake face over the course of one experiment, as a function of angle. 69

FIGURE 7.6: Selected recession plots at 0, 7.5, -15, and -22.5 degrees. The nose recession increases in a gradual manner, then jumps at 22.5 degrees - the y axis must be changed to accomodate the higher recession. 71

FIGURE 7.7: Nose and leading edge recession for the residuals in Figure 7.6. 71

FIGURE 7.8: Outliers at higher angles of rotation. Both have edge recession to such a large degree that nose wear cannot be differentiated from leading edge wear. 72

FIGURE 7.9: Angle data from all experiments, before and after outliers have been identified and removed from the data set. 73

FIGURE 7.10: Maximum nose and leading edge recession, averaged at each angle of rotation. 73

FIGURE 7.11: Bond distance as a function of crystallographic orientation before and after normalization. 74

FIGURE 7.12: Comparison of maximum edge recession to the predictive theory for angles of tool rotation between 0 and 25 degrees. The model is Equation 2.3, the dashed line is a cubic fit to that model from 0 to 55 degrees. 75

FIGURE 7.13: Edge recession residual plots from experiments conducted using custom tools at 10 degrees and +/- 25 degrees. The final two plots are on a larger vertical scale. 76

FIGURE 7.14: Edge recession residual plots from experiments conducted using custom tools at 55 degrees and 90 degrees. 77

FIGURE 7.15: The analysis developed for standard tools (shown in Figure 7.12), applied to the custom tools shown above. Negative angles of rotation are omitted. 78

FIGURE 8.1: Varation of oxygen partial pressure with time when controlling over the course of an experiment. 83

FIGURE 8.2: Enclosure used to control oxygen partial pressure while conducting wear experiments. A Lexan lid with rubber gaskets sits on top the aluminum rails during the experiment. 84

FIGURE 8.3: Detail view of the enclosure, showing the cutting setup and helium injection locations. 84

FIGURE 8.4: Section view of gap between spindle and aluminum plate. Pressurizes gas flows preferentially towards the enclosure interior and forms a gasket. 85

FIGURE 8.5: Residuals at lower levels of oxygen partial pressure. 86

FIGURE 8.6: Residuals at higher levels of oxygen partial pressure. 87

FIGURE 8.7: Wear rate with changing oxygen partial pressure. 88

FIGURE 8.8: Temperature close to and away from the tool tip for four experiments. 89

FIGURE 8.9: Temperature in the room where the diamond turning machine is located, over one twenty four hour period. The temperature varies cyclically by 1.5 degrees on a seven hour cycle. The right-hand plot shows a shorter period. A thirty-minute cycle over a half degree range is seen. 89

FIGURE 8.10: Langmuir curves for selected values of k 91

FIGURE 10.1: Setup for conducting wear rate experiments while controlling the workpiece temperature. 96

FIGURE 10.2: Two possible methods of measuring temperature at the cutting interface. The thermocouples allow essentially infinite lateral resolution by plunging repeatedly, moving the tool laterally each time. 97

FIGURE 10.3: Experiment designed to measure V_b, cutting edge sharpness, and edge recession as a function of cutting distance. 98

PREFACE

The research objectives of this project are:

1. Measure the effect of oxygen partial pressure on diamond tool wear during single point diamond turning. These effects could include alteration of the magnitude, shape, or location of wear along the cutting edge.

2. Measure the effect that crystallographic orientation has on recession of the cutting edge, and crater wear of the rake face.

3. Enable developent of models for chemical diamond tool wear using the methods, models, and data from the proposed experiments. This will be done by systematically varying the process conditions *crystallographic orientation*, *oxygen partial pressure*, and *workpiece temperature*.

The hypotheses tested are:

1. Edge recession will vary with crystallographic orientation, but crater wear and cutting edge temperature will not. The magnitude of edge recession at a given orientation can be predicted by the average distance between bonds at that plane.

2. Lower oxygen partial pressure will result in lower edge recession.

3. The wear experienced by a single crystal cutting tool when machining Cu-Ni alloys is nearly entirely chemical in nature.

Testing these hypotheses using the methods described serves two goals. One is to develop a quantitative model that can predict chemical wear rates of SCD turning tools. Models that predict temperature and activation energy have been made [4][5], but experimental measurements that directly validate these models are difficult. The

other is to develop practical approaches to reducing tool wear in difficult-to-diamond-turn materials by lowering the tool temperature at the cutting edge. This could be done by using special high-conductivity diamonds, optimizing the crystallographic orientation of the SCD tool, or machining in inert-gas environments.

CHAPTER 1: INTRODUCTION

1.1 Diamond turning and optics manufacturing

This introduction presents an overview of diamond turning, the analysis and measurement of wear of single crystal diamond tools, and the techniques commonly used to measure diamond tool wear.

Diamond turning is the process of using single crystal diamond cutting tools mounted on extremely precise machine tools to manufacture optical surfaces. Modern turn-key machines provide the following capabilities [6]:

- the ability to generate precisely defined three-dimensional contours,
- general accuracy of one part in 10^6,
- accuracy of one part in 10^8 along a single axis in ideal conditions, and
- surface finish of 5 nm R_a or better.

The diamond turning process can be the final step in creating a finished optic, or post-polishing operations may be used to improve surface finish or figure [7]. Diamond turning can produce surfaces which are difficult or impossible to manufacture through other processes, such as large off-axis aspheres, freeform optical surfaces, and some structured surfaces [8][9]. Alignment datums and features can also be integrated into parts, allowing for more effective metrology and post-processing of the optic [10], allowing for the design of 'snap-together' optical systems that require no alignment adjustments after assembly [11].

All of these characteristics make diamond turning an efficient, cost-effective method of manufacturing certain types of optical surfaces. It has become a commodity tech-

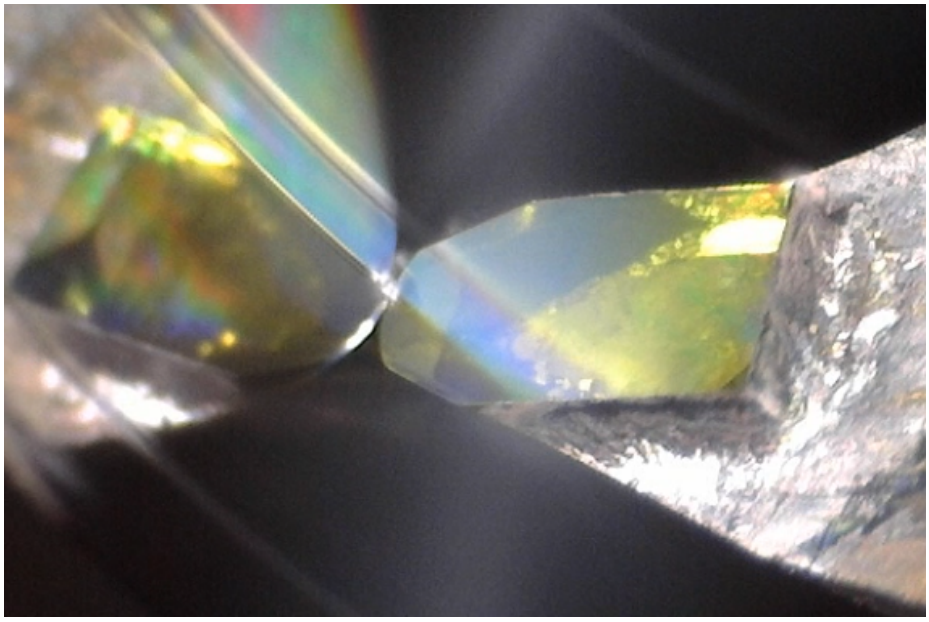

Figure 1.1: Single crystal diamond tool facing a Monel workpiece.

nology, dominating the market for items such as Fresnel lens molds and off-axis aspheres [1]. New applications are still being explored and developed. The manufacture of micro-photonics is currently dominated by lithographic processes, but this approach limits designers to two dimensions and relatively low aspect ratio configurations [6]. The ability of SPDT to create three-dimensional such as manufacturing of precision glass molding to mass produce freeform optics [12][13][14], and the manufacture of compact [15], high performance 'snap-together' freeform telescope systems [11].

Despite market dominance in some areas and increasing influence in others, SPDT is still limited to small range of metals and a few other materials which are considered 'diamond-turnable'. This term implies an innate property of the material, but actually refers to two possible cases. A material can wear tools so rapidly that it is not economical or practical to manufacture optics with, or tool-workpiece interactions can produce unacceptable surface finishes. The former criteria is actually an economic one–if the parts are sufficiently valuable, materials which cause high wear rates will still be used. An example of this is silicon aspheres, which cause considerable wear on diamond tools but are still commonly manufactured using them to generate the

final surface.

Diamond turning in its modern incarnation has been evolving for nearly 70 years [16], discussions of diamond-turnability have alwasy illustrated the practical, pragmatic approach generally taken when investigating tool wear and the diamond-turnability of materials. Early publications discussing optics fabrication using SPDT tended to provide lists of, or statements about, which materials where 'diamond-turnable'. Electroless nickel (eNi) was discovered (as an SPDT manufaturing process) by Casstevens in 1978 [17], the heat treatment and phosphorus percentage needed to minimize wear were investigated by Taylor et. al. in 1986 [18], and processes for the use of electrodeposited nickel in SPDT manufacturing were developed by Dini et. al. in 1990 [19]. A detailed model explaining the relationship between phosphorus content and reduced tool wear was not proposed until 1996 [1]. Detailed models of thermo-chemical wear have only begun to emerge recently [5].

The material limitations of diamond-turning are one of its greatest drawbacks, so they are being constantly being pushed against [20]. Some of the most desirable materials for optics manufacturing, such as steel, silicon, and certain polymers, pose significant challenges from a tool wear perspective. The manufacture of optics using steel injection molds requires the use of pre-hardened steel molds which are then pre-machined, and finally polished to optical quality. This process provides good surface finish but inferior form tolerance. The use of diamond tools to manufacture molds allows for tighter form tolerances and the ability to superimpose micro-structures onto the mold surface. This process is currently limited to materials such as brass, certain aluminum alloys, and steel molds with electroless nickel platings. The ability to exchange aluminum for hardened steel in a typical mold can increase the mold lifetime by an order of magnitude [21].

Silicon is difficult to diamond turn but has substantial applications in optics manufacturing – it is chemically inert, has high hardness, is lightweight, and has good

optical propterties. Success has been found using laser assisted machining (LAM) to reduce tool wear when diamond turning both silicon and silicon-carbide optical surfaces. The proposed hypothesis is that the laser 'thermally softens' the material at the tool-chip interface, increasing ductility and reducing tool wear [22][23][24]. Polymers such as Polymethyl methacrylate (PMMA) and Polycarbonate (PC) are commonly used to manufacture optical surfaces, but tribo-electric and tribo-chemical wear can both cause surprisingly high rates of tool wear [2][25][26].

The development of electroless nickel platings as a hard coating which produces negligible tool wear in diamond tools was a significant breakthrough. Previous to this SPDT was limited to soft, fcc metals, primarily copper and aluminum. These materials are both susceptible to corrosion from cleaning fluids and damage from handling. The phosphorus content of eNi coatings ranges from 2 to 22%. Sufficiently high phosphorus levels results in a hard, corrosion-resistant surface that causes negligible wear of diamond tools [17]. The discovery of eNi as a coating that produces low wear in diamond tools was followed by systematic research investigating the the effects of phosphorus content and heat treatment [18], the manufacture of nickel-phosphorus alloys by electrodeposition [19], and the chemical model which describes the effect [1].

Researchers have been attempting to generate a similar breakthrough regarding ferrous metals for nearly half a century, but with limited success. Reduction of contact time between the tool and workpiece by ultrasonic vibration has had some success [27][28], but techniques which reduce or inhibit the rate of chemical reactions have generally either been ineffective, difficult to reproduce [29], or hampered by serious practical concerns.

An interesting example of the latter is cryogenic diamond turning of steel [30], which offers substantial reductions in wear rates at the expensive of extreme temperature differentials in the machine tool– and the corresponding impact on accuracy [31]. One approach to reducing chemical wear of diamond tools when cutting high-wear

metals that has found some success is modification of the workpiece [32][33]. In 2006 Brinksmeier et. al. reduced the wear when diamond turning steel three orders of magnitude by nitriding the workpiece to change the chemistry of the surface and subsurface [34].

Research along these lines will continue, because new materials open the door to new applications and new markets. Increased insight into cutting mechanics and tool wear mechanisms in diamond turning is integral for enabling new applications- both the ones described here and others yet to be discovered- and wear measurement plays a key role.

1.2 Measurement of wear in single crystal diamond cutting tools

Wear of diamond tools has been of interest to precision engineers since the 19th century diffraction grating 'boom' following the Industrial Revolution, when William Rogers discovered the relationship between diamond hardness and crystal orientation [16].

While economics and 'unlocking' new materials and processes is the primary driving force, motivations for measuring tool wear can be broken into the following categories:

- a methodology for investigating wear mechanisms or behavior at the cutting interface;
- testing or enabling new manufacturing processes or materials; and
- developing or refining measurement technology or techniques.

Diamond turning as a manufacturing technique was developed in the 1940s; a large body of research on the properties of diamond emerged in the following decades [35][36].

Research on wear in SPDT began in the late 1970s with machinability tests on electroless nickel (eNi) platings [17], and an investigation of the chemical wear in SPDT of mild steel [37][38]. These papers highlight the primary themes of the subse-

Table 1.1: Tool wear measurement techniques

	Measurement Method	On Machine?[a]
Indirect Methods	Surface parameters	N[b]
	Part acceptance	Y
	Tool life	Y
	Cutting force	Y
Direct Methods	Wear land (V_b)	N[b]
	Witness sample plunge cut	Y
	Atomic force microscopy	N
	Electron beam induced deposition	N

[a] Can the measurement be performed without removing the tool or part from the machine?

[b] Measurement can be done by replicating the cutting edge, allowing tool to remain in-situ.

quent two decades: enabling the use of electroless nickel as an optical material, and understanding why steel is so difficult to diamond turn.

There are at least six different viable methods of tool wear measurement (Table 1.1); these can be classified as direct or indirect. The former provide a physical measurement, while the latter infers wear through some other parameter, such as surface finish. Investigating wear mechanisms often requires the use of multiple techniques to develop insight into different aspects of the process being studied [39]. Methods can be further delineated as on-machine or off-machine: does the tool or workpiece need to be removed from the machine in order to conduct a measurement? On-machine measurement systems are advantageous in that multiple measurements can be performed during one experiment, providing information about how wear is evolving over time. It should be noted that this is not a clear cut demarcation–a part surface can be replicated without removing it from the spindle, and a scanning electron microscope (SEM) could be integrated into a diamond turning machine with sufficient engineering effort. This has already been done on a limited scale [40][41].

The primary direct, high resolution methods of tool wear measurement are SEM

imaging, Electron Beam Induced Deposition (EBID) [42], plunge cut measurement, and atomic force microscope (AFM) measurement [43] of the cutting edge. SEM images provide fine detail at high magnification, but are primarily valuable for qualitative inspection of the cutting edge. Built up edge and defects in the cutting edge can both be easily identified this way. EBID allows for precise measurement of cutting edge radii, but has effectively zero lateral resolution. AFM measurements of wear are extremely high resolution along the cutting edge and tool radius, but are time consuming and must be performed off-machine. Plunge residuals give high-resolution measurement of edge recession along the tool radius, allow for on-machine measurement, but provide no information about cutting edge sharpness.

Despite the broad array of available measurement techniques and substantial body of literature on the subject, there are still gaps in both the theory of diamond tool wear and experimental validation of that theory. For example, the relationship between atmospheric composition, pressure, and diamond wear has been investigated by multiple researchers, with conflicting results. In the mainstream tribology literature, considerable work has been expended understanding "running in" evolution of wear mechanisms as wear increases. Little has been done on the early stages of wear of single crystal diamond tool. A 'running-in' effect was observed in the vast majority of experiments performed during this work; closer investigation of this phenomenon would be a good candidate for future research. The detailed surface chemistry involved in C-C bond breaking in the presence of clean metal surfaces is not well understood. There is some literature on diffusion of carbon into work pieces–but this does not explain the bond breaking mechanism that causes wear.

Attempting to move questions like this towards conclusive answers is the goal of this research. Continued refinement of existing measurement techniques, and development of new approaches, is integral to continued progress in this field.

CHAPTER 2: BACKGROUND

This chapter presents an overview of wear in diamond turning from the perspectives of oxygen partial pressure, crystallographic orientation and chemical activation energy. The models used to analyze results of the experiments described in Chapters 3 through 8 are developed.

2.1 Physics of single crystal diamond tool wear

While this work is primarily concerned with chemical wear, the wear of diamonds can be caused by multiple phenomena and is often dependent on multiple external (or difficult to measure and account for) variables. Examples include variation in quality between diamond tools [44], environmental temperature control, and workpiece imhomogeneity. These phenomena and other variables that impact wear rates are discussed *infra*. A useful schema for classification of tool wear defined by Paul [1] and Evans [30] is:

- mechanical abrasion of the diamond surface;
- chipping or fracture typically caused when inclusions in the workpiece impact the tool;
- built up edge causing adhesion between the diamond and workpiece; and
- tribothermal/tribochemical wear.

Even inside of these discrete categories the morphology of worn tools and behavior of the mechanical system can vary substantially. For mechanical abrasion, the behavior is highly dependent on the crystal facet being abraded. The resistance of diamond to abrasion is anisotropic on all three of the primary crystal planes, and also

varies substantially between crystal planes [35]. Adhesions cause damage to the tool when the chip sticks to the diamond surface, creating an overturning moment that repeatedly puts the tool edge under tension, ultimately resulting in failure. Chipping or fracture may be caused by single, large inclusions, or fatigue caused by a great number of lower energy impacts.

Wear of diamond tools depends on many factors:

- spindle speed, feed rate, and depth of cut [3];
- environmental variables such as coolant and chip clearing [45];
- geometry and local variations in composition of the cutting tool [46];
- bulk properties and local composition of workpiece; and
- orientation of the diamond crystal structure to workpiece [37].

Observed wear is also sensitive to experimental design, and external variables such as temperature control, machine stiffness, and operator skill, because small process variations can have large effects on wear rates. The complex nature of the system and wide variety of observed results means that there is not one evaluation method that can be used to analyze all aspects of tool wear; multiple mechanisms may be contributing in any given circumstance and all of them must be accounted for. For example, an approach well suited to identifying chips or grooves in the tool may be poorly suited to measuring cutting edge sharpness, and vice versa.

The materials used as stock for diamond turning optical surfaces include pure metals, alloys, and ionic crystals. Both wear rates and mechanisms vary tremendously across this range of materials. Aluminum generally cause low levels of wear, but this is not true of all aluminum alloys. The primary mechanism of wear is generally abrasion and chipping of the diamond when it contacts impurities in the aluminum at the grain boundaries, but adhesion between the diamond and workpiece surface

may also contribute [47]. In iron and steel, rapid wear is induced through built up edge [45], chemical effects and the impact of carbides against the tool edge. Plastics such as Polylmethyl methacrylate (PMMA) and Polycarbonate (PC) cause high tool wear despite being much softer than diamond, primarily due to electrostatic discharge [26] [2].

If conditions (in this case, the workpiece material) are thoughtfully chosen, individual mechanisms of wear may be isolated and studied. To isolate and study chemical wear single-phase Cu-Ni alloys are used here. They are single-phase at all compositions and contain no intermetallic particles that could chip or abrade the tool, allowing the assumption that chemical wear is the dominant mechanism of edge recession. Spindle speed, feedrate and depth of cut are fixed for most experiments to allow inter-comparison between results.

2.2 Measurement and characterization of chemical wear in single crystal diamond tools

Several models have been proposed to describe chemical wear in single crystal diamond cutting tools. The simplest models attempt to relate hardness, crystal structure, or melting point to tool wear, More complex models attempt to describe wear in terms chemical mechanisms, such as diffusion, and graphitization via catalytic mechanisms.

Initial descriptions of chemical diamond tool wear describe the process as a form of graphitization– the reversion of carbon atoms in the diamond lattice to stable graphite form [38]. Under normal conditions the energy barrier for this reaction is very high; with no catalyst, graphitization of diamond requires temperatures of 800 degrees Celsius. The high wear rates observed when machining iron or steel were explained in terms of 'iron's affinity for diamond' [37], and this affinity was posited to involve a catlyst which raised the reaction rate. These assertions of 'chemical affinity' were broadly correct.

Paul, et. al. points out that attempts to relate wear to hardness, crystal structure, and melting point each have their own critical flaw. Broad trends are often easily identified, but upon closer inspection they fail to provide explanatory capacity. Melting point correlates well to diamond turnability, but it is difficult to identify a 'transitional' melting point, below which all materials are diamond turnable and above which none are. For instance, silicon and beryllium are diamond turnable, but have higher melting points that Uranium, which is not. Hardness has a similar problem in that general trends are observable, but significant exceptions occur. Electroless nickel stands out as a material which causes negligible diamond tool wear, while pure nickel has comparable hardness but induces rapid and massive tool wear. Crystal structure presents additional clues, but lacks full explanatory capacity. Most elements with bcc structures are not diamond turnable, but hcp, fcc, and other structures show no bias for or against tool wear.

The most complete model predicts chemical wear rates in diamond tools by defining the chemical relationship between elements which cause high wear and diamond.

A greater number of unpaired d-shell electrons in the workpiece correlates to low chemical activation energy, easier formation of carbon-metal complexes, and higher wear rates. For many common engineering materials wear rates also correlate strongly with hardness, and there with higher cutting temperatures. To ensure that unpaired d-shell electrons are the primary driver of chemical wear for elements, Paul et. al. experimentally demonstrated chemical wear when machining Cerium, a very soft metal with one unpaired d-shell electron. Using a soft metal removes the correlation with hardness from consideration, isolating the workpiece chemical composition as the primary cause of wear.

Chemical reactions have multiple pathways through a potential energy surface, leading from a starting state to some end state. The starting state for this process is carbon atoms on the surface of a diamond tool, and the end state is separation of

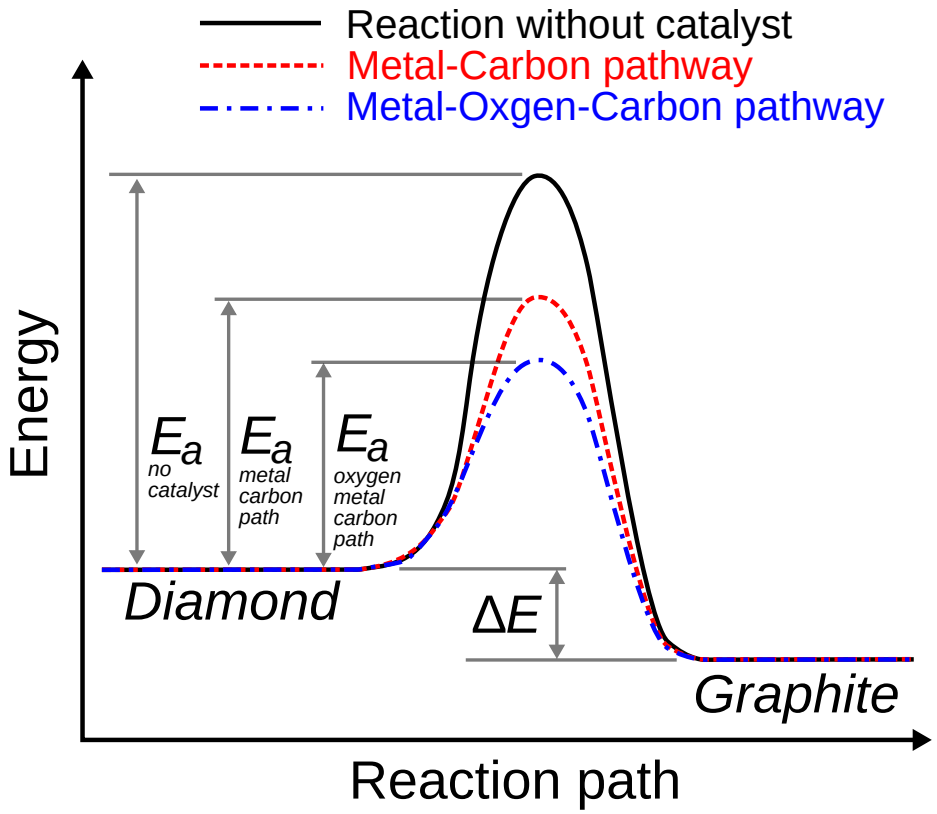

Figure 2.1: Reaction coordinate diagram for metal-carbon and metal-oxygen-carbon pathways [1].

those atoms from the bulk diamond through their attachment to a metal atom from the workpiece. Regardless of the path taken, the reaction must pass over an activation energy barrier E_a. The reaction rate can be related to the activation energy by the Arrhenius equation,

$$r = Ae^{\frac{-E_a}{RT}} \tag{2.1}$$

where r is the reaction rate, R is the ideal gas constant, and T is the system temperature. The pre-exponential factor A can be thought of as a scaling factor which is dependent on the specific conditions of any particular experiment.

There are two possible pathways for this system: with or without oxygen (Figure 2.1). Reaction rates along the aerobic path are hypothesized to be proportional to the oxygen partial pressure p_{o2}, so the wear rates can be written as the sum of both reaction pathways.

$$w = r_{aerobic} + r_{anaerobic} = p_{o2} A_{aerobic} e^{\frac{-E_a}{RT}} + A_{anaerobic} e^{\frac{-E_a}{RT}} \tag{2.2}$$

This model sits on strong foundations in fundamental chemistry, and presents an extensible model that, when used in conjunction with careful analysis and the large body of literature available on mechanical wear, presents a fairly complete theory of wear in single crystal diamond tools.

This work uses the model for two purposes. The first is to test the hypothesis that wear rates will decrease as oxygen partial pressure is lowered. Since one pathway for chemical reaction is 'cut off', it is expected that total wear will decrease as less oxygen is available to drive the reaction. The second is to measure the activation energy of chemical wear using Equation 2.1. By performing cutting experiments and multiple temperatures and fitting a curve to the results the activation energy E_a of the chemical reaction can be measured.

2.3 Proposed model for anisotropy of chemical wear rates

It has been obvious for some time that wear of diamonds is dependent on crystallographic orientation of the diamond lattice with respect to the workpiece [48] [49] [39], but a model that relates lattice geometry to chemical wear rates has not been developed. Chemical reaction rates are generally studied in terms of gas or solution based reactions, where isotropic conditions can be assumed. Surface reactions are significantly more difficult to study and understand because characteristics of the reaction depend on the specific characteristics of the surface being investigated. Chemical wear in diamond tools is a surface reaction system. In particular, the crystal face presented by the diamond tool to the workpiece is a critical parameter in understanding and predicting wear rates.

Assuming equal initial edge quality and crystal structure between all tools used, the proposed predictive model is that as the bond density per unit area decreases,

the rate of chemical wear increases. For the tools used in these experiments, this means that edge recession should change when the tool is rotated with respect to the workpiece, but the rate of crater wear should not. This is because the rake face bond density stays constant when the tool is rotated, but the bond density presented by the cutting edge changes. Areal bond density is defined by the equation

$$n_{hkl} = \frac{4}{d^2} \frac{max(h,k,l)}{\sqrt{h^2+k^2+l^2}} \tag{2.3}$$

where $d = 0.356\ nm$ is the lattice distance, and (hkl) is the miller indices of the crystal plane [50][51]. Taking the inverse of bond density and multiplying by bond length gives the volume of diamond cleared when a single carbon atom is removed from the lattice. Wear is the removal of carbon atoms either singly (chemical wear) or in clusters (mechanical wear); it follows that a greater volume of diamond cleared per carbon atom will result in higher rates of chemical wear.

Figure 3.1 shows the experiment coordinate system, and Figure 7.1 shows the diamond crystal structure. Lattice planes can be used to define rotation of the tool with respect to workpiece normal by mapping them onto the experiment coordinate system (Equation 2).

$$\theta = cos^{-1}\left(\frac{(001)\cdot(hkl)^T}{||001||\cdot||hkl||}\right) \tag{2.4}$$

The inverse of n_{hkl} multiplied by the bond length is plotted against θ in Figure 7.11a and predicts that maximum volume removed per carbon atom occurs at 55 degrees.

The model described here treats the crystal structure as a continuous function, sampled at discrete points. Surface terminations and variations in abrasion resistance may also effect the rate of wear. In particular, the intersection of two [110] planes is extremely soft. This may lead to difficulty in obtaining and keeping a sharp edge, and high rates of abrasive wear even with softer workpiece materials.

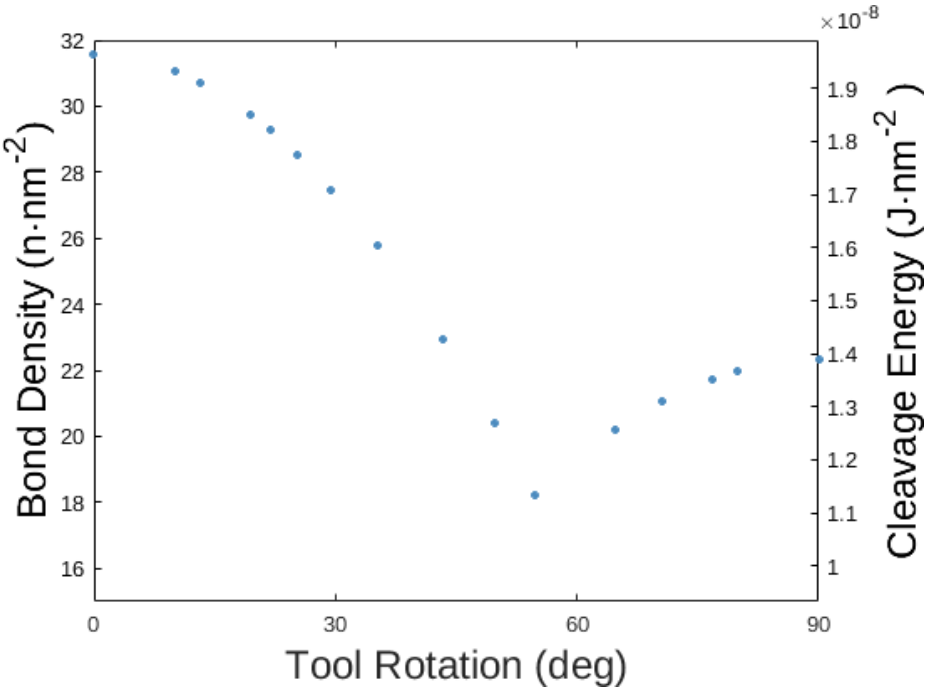

Figure 2.2: Relationship between bond density and orientation. At 0 degrees the tool is normal to the workpiece and the $< 100 >$ direction on diamond blank is also normal to the workpiece. Theta is the angle between $< 100 >$ on the diamond blank and the workpiece's normal vector.

CHAPTER 3: PLUNGE CUT RESIDUAL MEASUREMENT METHOD

All wear data produced during these experiments was analyzed using the plunge cut method described below. This chapter briefly describes the history of tool wear measurement, development of plunge cut measurement methods, and the fundamental experimental setup used in all experiments describes in subsequent chapters.

3.1 Overview of diamond tool wear measurement

Wear of diamond tools has been of interest to precision engineers since the 19th century diffraction grating 'boom' following the Industrial Revolution, when William Rogers discovered the relationship between diamond hardness and crystal orientation [16]. Diamond turning as a commercial manufacturing technique was developed in the 1940s; large body of research on the properties of diamond emerged shortly thereafter [35][36]. Research on the wear of diamond tools *when machining* began in 1973, when Verrill published the first recorded use of a profilometer to measure plunge cut shape on a diffraction grating [52][53]. It is unclear if later SPDT research drew inspiration from this work.

Around the same time, Casstevens was conducting machinability tests on electroless nickel platings [17], and Thornton was investigating chemical wear when diamond turning mild steel [37][38]. This highlights the primary themes of the following decades: enabling the use of electroless nickel as an optical material, and attempting to enable the use of ferrous metals as optical materials. The available methods of wear measurement were surface finish, tool life, optical measurement of flank wear, and SEM imaging. Wilks' 1980 paper relating the mechanical properties of diamond and tool wear rates deserves special mention for the use of all available techniques to

measure tool wear. Flank wear is used to calculate wear rates, surface finish for investigating variations between tools, SEM imaging to show cutting edge morphology, and statistical analysis of 'part acceptance' to evaluate tool quality [39].

The methods described above are all simple, effective, and easy to implement. Changing surface finish parameters indicate wear, can be measured interferometrically or with a profilometer, and can provide information about tool shape [44] . Tool life as a measurand is binary and slightly arbitrary, depending on where the cutoff between good and bad parts is set. However, a large amount of data can be generated quickly, making the process amenable to amenable to statistical analysis [54]. Optical flank wear measurement provides wear rate at the nose and information about edge morphology, but has no lateral resolution. Additionally, care must be taken to keep the wear rate linear if measurement results are to be extrapolated [38]. SEM imaging is excellent for viewing fine detail at the wear land and using that morphology to support or develop theory [55].

In the mid-80's measurement techniques began to evolve. In the spring of 1987 Syn et. al. [56] and Hurt [57] both published research that used tool plunges in low-wear materials to evaluate the shape of the tool. The former was investigating wear rates when machining eNi, while the latter was interested in evaluating tool quality before use in manufacturing.

The extension of this measurement method developed by Browy and Evans [58], and further extended in this work, allows measurement allows measurement of edge recession with sub-micrometer lateral resolution and measurement uncertainty under 50 nm. The lateral resolution this method provides allows nose and edge wear to be analyzed as separate parameters, and for small periodic structures to be identified and investigated.

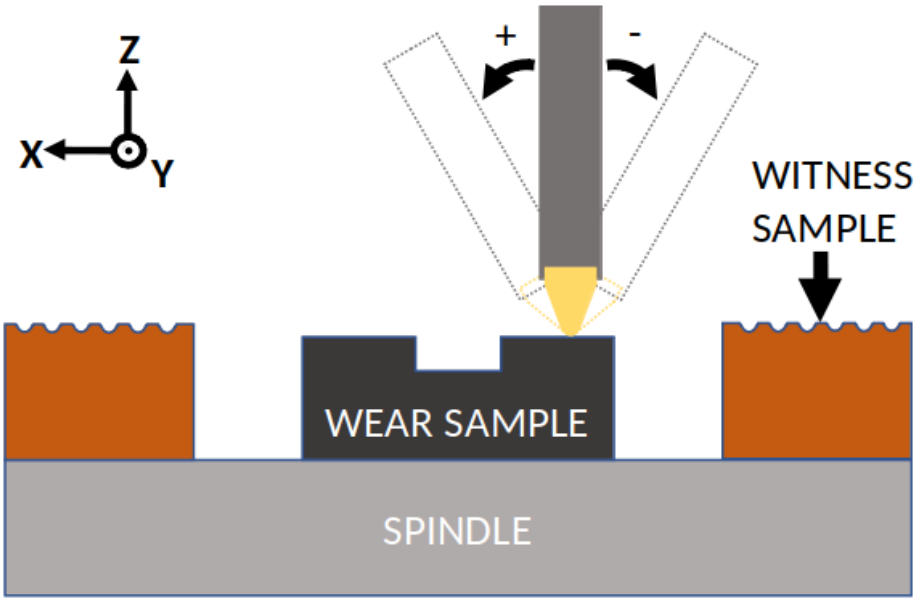

Figure 3.1: Illustration of coordinate system and sign convention for tool rotation with respect to workpiece normal.

3.2 Basic experimental setup and process

This section describes the process used to collect plunge cut measurements of the cutting tool. The description uses a facing process, but the general procedure is identical for experiments where the workpiece is turned instead of faced.

The wear and witness samples are set up as shown in the above figures and edge recession of the diamond tool is measured by plunging the diamond into the witness sample after each cutting pass, creating snapshots of the tool's shape after each cut. The wear sample is a Cu-Ni alloy, while the witness sample is an aluminum ring with a 100 µm thick Udylite Bright Acid Copper (UBAC) coating. The alloy is single-phase, and UBAC is fine grained, high purity copper. The tool post is set up to orient the tool at positive or negative ten degrees from normal to the part surface in order to allow each cutting tool to be used for two experiments before resharpening. Unless otherwise stated, all experiments described in this document are performed at positive or negative ten degrees. In some experiments, additional angles are used to investigate the effects of crystallographic orientation on tool wear.

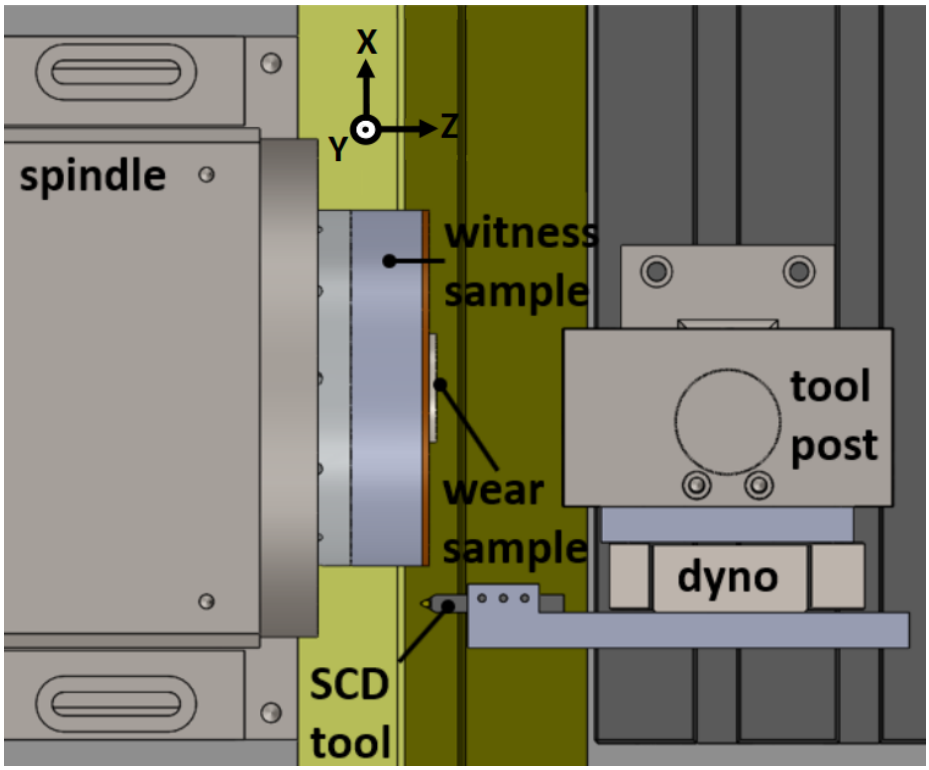

Figure 3.2: Layout for experimental setup (plan view).

Table 3.1: Standard parameters for tool wear experiments

Spindle speed (rpm)	Feed rate (mm/min)	DOC (µm)	DOP (µm)
1000	2	5	12
Tool radius (mm)	**Tool clearance (deg)**	**Tool rake (deg)**	**Plunge Infeed (mm/min)**
0.5	6	0	0.05

Both parts are turned using carbide tools after mounting to reduce spindle imbalance. Imbalance is measured using a Lion Precision C8 capacitance probe with CPL190 signal conditioner. Large radial errors cause the tool to wear on the leading and trailing edges, and also distort the plunge shape.

After setup is completed the spindle is run for 1-2 hours to minimize effects of spindle growth on the experiment. The wear sample is then faced with a carbide tool at 2 um/rev; the witness sample is faced with a SCD tool at 2 um/rev. Cutting parameters and tool geometry are shown in Table 3.1.

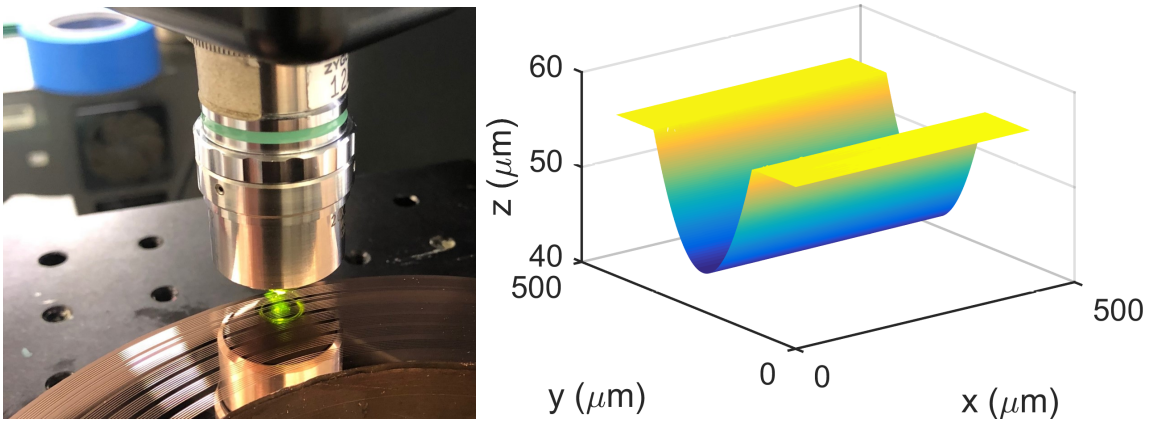

(a) Taking inteferogram of plunge.

(b) Result of typical plunge interferogram.

Figure 3.3: Measuring the plunges from an experiment. This ring contains six separate experiments, each with six plunges.

3.3 Plunge measurement and preliminary processing

After machining the witness sample is removed and cleaned in an ultrasonic acetone bath. The plunges are then measured using the ZeGage coherence scanning interferometer with the 20x objective.

These measurements are then imported into MATLAB® and processed into tool wear residuals. Before any addition processing, the plunge data is interpolated from 0.41 µm/pixel to 0.10 µm to allow finer correction of misalignment about the z axis. Piston and tilt are removed by subtracting a plane fit to flats on each side of the plunge from the data. Rotation is removed by algorithmically locating the left plunge edge near the front and back of the array, finding the angle between these locations with respect to the vertical axis, and rotating the matrix about this angle using the function `imrotate` (Fig. 3.4).

Once all plunges are aligned they are individually column averaged to create '1-D' data and a reference is created by least-squares fitting a circle to the unworn plunge.

The raw data is now roughly aligned, but is not sufficiently aligned to create the residuals. There are two algorithmic approaches that have been used at UNCC to

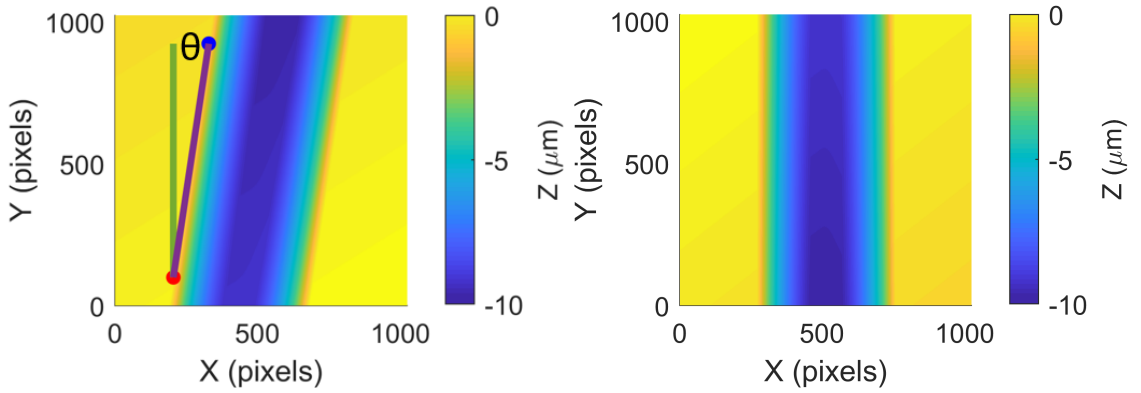

(a) Plunge phasemap before rotation correction. (b) Plunge phasemap after rotation correction.

Figure 3.4: Rotating the height map to correct misalignment. The two dots represent the plunge edge located by the edge finding algorithm. Since the vertical and horizontal distance between the points in pixels is known, θ can be calculated.

perform final alignment, the *slope alignment method* and the *sag alignment method*.

3.4 Final plunge alignment and residual calculation

Two methods of final plunge alignment are presented here. Both are viable methods of achieving sub-pixel alignment capable of aligning the plunges such that uncertainty in the edge recession measurement is less than 50 nanometers, but there are advantages and disadvantages to each approach. Some practical considerations are discussed below, and a detailed uncertainty analysis is presented in Chapter 4.

3.4.1 Slope alignment method

The method described here is summarized visually in Figure 3.6. Take two semicircles, shift one a small amount to the left or right and subtract it from the original; this will yield a straight line. The slope of this line depends on how much the semicircle was shifted, and the relationship is linear. This result can be used to develop a calibration for correcting plunge lateral misalignment.

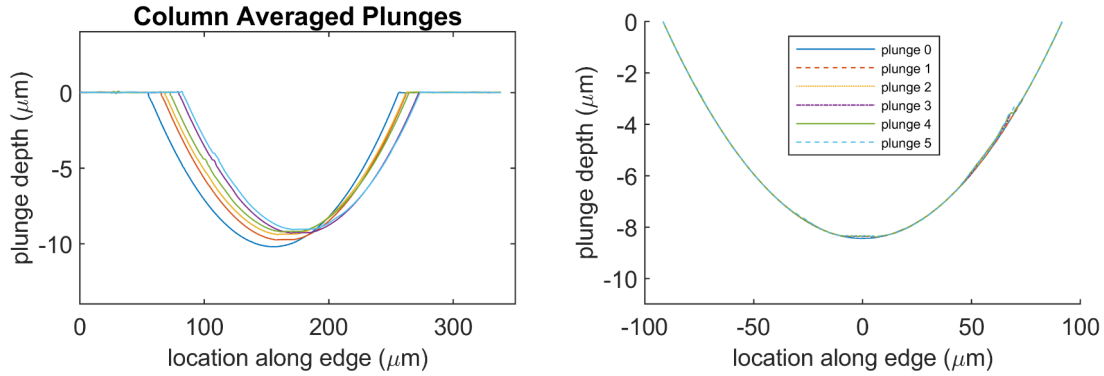

(a) Column averaged plunge phasemaps, before final alignment.

(b) Plunge phasemap after final alignment.

Figure 3.5: Column averaged plunge phasemaps, before and after final alignment.

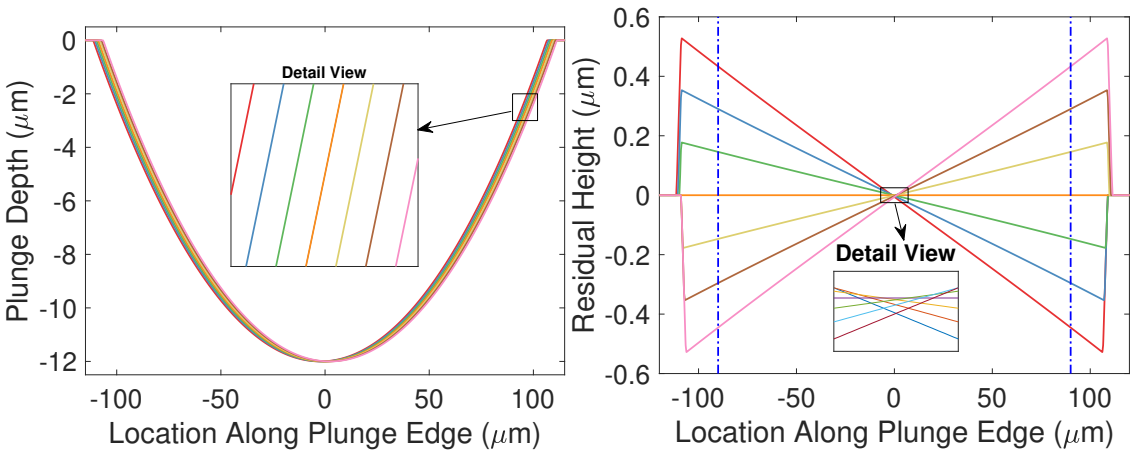

(a) Plunge phasemap before rotation correction.

(b) Plunge phasemap after rotation correction.

Figure 3.6: Shifting and subtracting plunges to create residuals. Angle of the residual increses with greater pixel shift.

1. Create a simulated plunge profile with the same nominal radius as the tool used in the experiment.

2. Interpolate this simulated plunge to a horizontal spacing of 0.10 µm.

3. Create an array of index shifts `[-N:1:N]`.

4. Loop through the index shift array and use `circshift` to create a series of shifted plunges, where the reference plunge is centered at zero (Fig. 3.6a).

5. Subtract the shifted plunges from the reference plunge.

6. Trim the result, keeping only the linear portion. This yields a series of straight lines through zero of varying slopes, where greater slope indicates more pixel shift. (Fig. 3.6b).

7. Find the slope of each residual and plot against the index shift array (Fig. 3.7).

8. Find the least squares fit to the data, this yields a formula that describes the relationship between residual slope and plunge lateral misalignment.

$$N = S \cdot \theta \tag{3.1}$$

Once developed, this formula is applied to plunge measurements. The simulated plunge is taken as a reference and subtracted from each plunge, creating a series of misaligned residuals. Each has an unworn portion, this is seen in Fig. 3.9 as values less than approximately -20 µm. Measuring the slope of this unworn portion and applying Eq. 3.1 gives the index shift each array needs to become aligned with the reference.

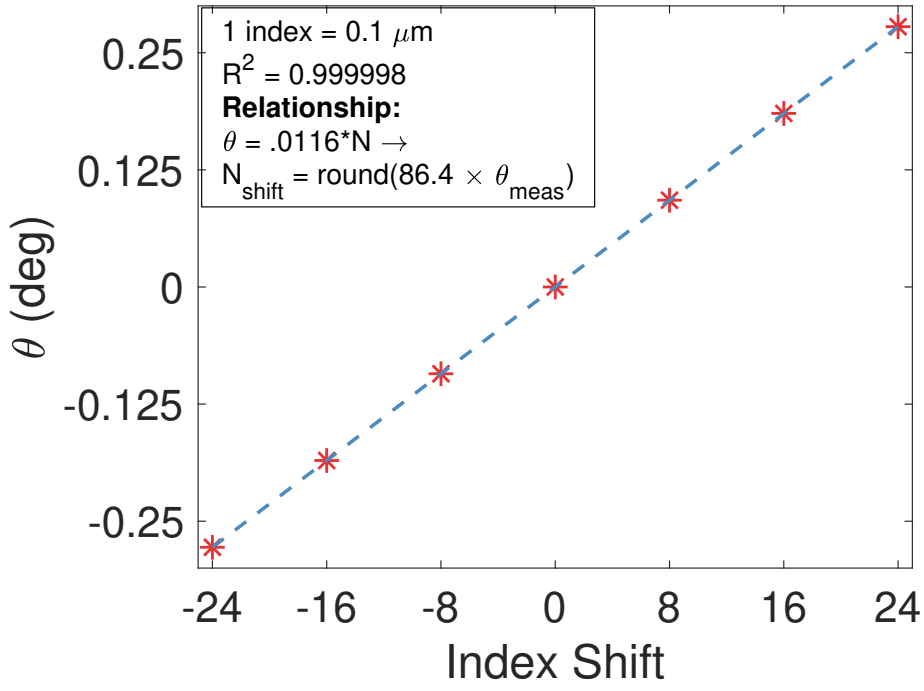

Figure 3.7: Relationship between pixel shift and residual slope.

3.4.2 Sag equation alignment method

The *sag equation alignment method* uses Equation 3.2 to trim each plunge at the same location, aligning them with sub-pixel precision.

$$h = \frac{f^2}{8R} \tag{3.2}$$

Using the tool radius for R and choosing some h smaller than the plunge depth but larger than the facing depth of cut the equation is rearranged and solved for f. A scan height z_0 is chosen to begin searching for the trim point. This position must be below the plunge edge, but above the z-height of f. This can be expressed as

$$z_0 \geq |\min(z)| - h \tag{3.3}$$

where z is the plunge array and z_0 must be less than zero. At this scan height the first and last x values (x_1, x_2) smaller than z_0 are found. If $|x_2 - x_1| <= f$, then

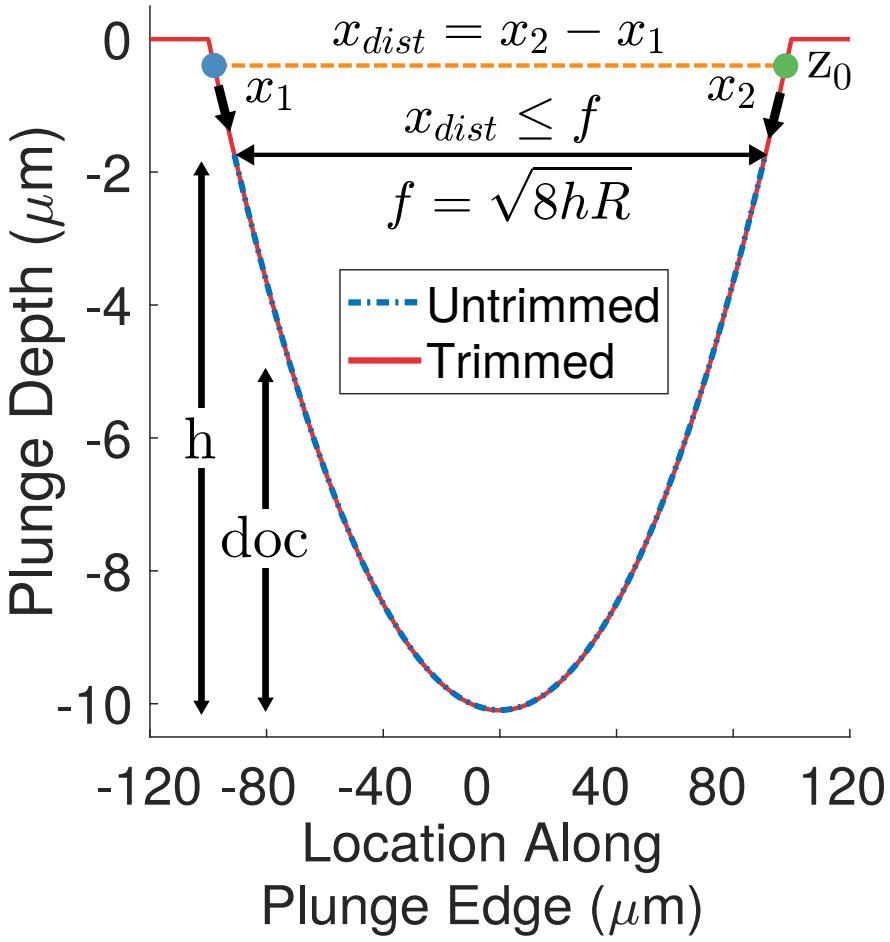

Figure 3.8: Schematic description of the sag alignment process. Starting at z_0, x_{dist} is compared to f. z_0 is incremented down until x_{dist} is less than f, at which point the plunge is trimmed.

the plunge is trimmed at this point. Otherwise $z0$ is decremented by some value dz and the process is repeated (Fig. 3.8). This procedure is repeated in a loop until the criteria is satisfied and the plunge has been trimmed. This algorithm is applied to all plunge measurements, trimming them to equal lengths.

3.4.3 Residual calculation

After final alignment the data is analyzed by preparing residuals. To create these residuals a reference circle is fit to the unworn tool shape and subtracted from each plunge, this "unwraps" the tool edge and gives a best estimate of tool shape as a

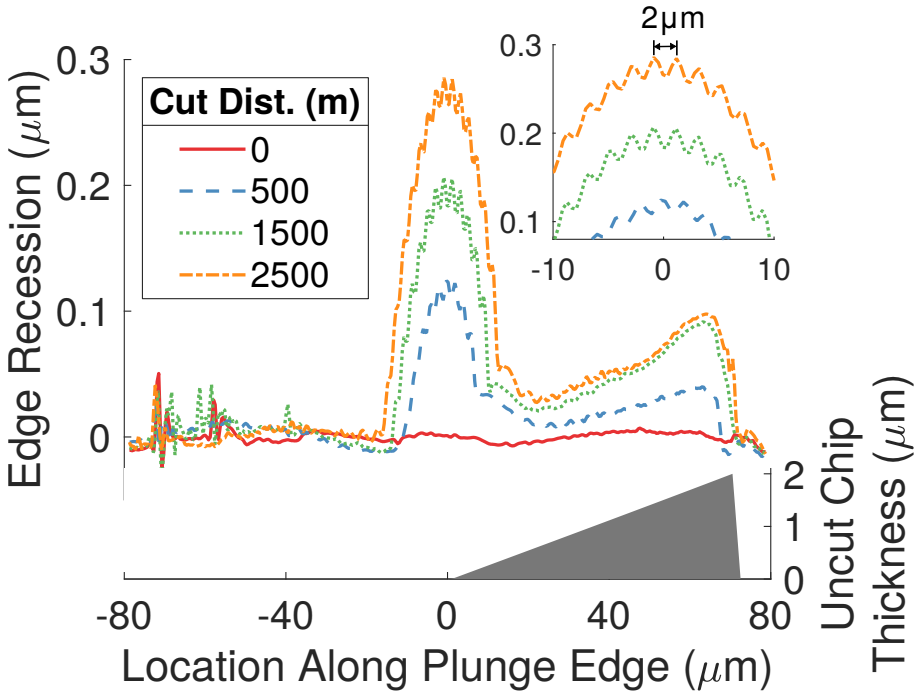

Figure 3.9: Typical residual obtained by subtracting a best-fit circle from the column averaged, aligned plunge data.

function of position along the tool edge. Using a circle means that form, waviness, and roughness information are all preserved in the residual. For the residuals shown in Figure 3.9 0 µm is the nose location, positive values indicate the leading edge, and negative values indicate the trailing (unworn) edge. The residual may also be plotted against uncut chip thickness. A significant amount of information can be extracted from this plot. The residual for plunge zero describes the shape of the unworn tool and each subsequent plunge residual describes the tool shape after N $\times$ 500 m of cutting distance, where N is the plunge number. Nose recession and edge recession can be seen as separate phenomena with their own characteristic shapes, unfiltered residuals show any high-frequency content in the tool edge, and all of this can be seen evolving as cutting distance increases.

CHAPTER 4: MEASUREMENT UNCERTAINTY AND OUTLIER ROOT-CAUSE ANALYSIS FOR PLUNGE CUT RESIDUAL MEASUREMENTS

Most of the experiments described in this document rely on plunge cut residual measurement, calculated as described in Chapter 3. Interpretation of these results relies on physical understanding of the systems involved, control of the experimental process and conditions, and an understanding of the range of values that could reasonably be attributed to the results of each measurement. Plunge cut edge recession measurements provide sub-micron lateral resolution, but if the z value at each position along the cutting edge could be attributed to a range of values micrometers wide the process would not be very useful. Understanding the range of values that can reasonably be attributed to the measurement is necessary to interpret the data.

This chapter includes an analysis of measurement uncertainty for the plunge cut residual measurement of edge recession, and a discussion of experimental outliers and their causes. The residuals which are the output of the experiments conducted here can be affected by two problems: measurement uncertainty inherent in plunge cut measurement and residual calculation, and outliers caused by experimental variables. An experiment can provide residuals with low measurement uncertainty but unexpectedly high wear rates due to an insufficiently sharp tool, error motions in the machine spindle, insufficient tool post stiffness, or other environmental variables, leading to unacceptable results that must be discarded. An example of this phenomenon is shown in Figure 4.8.

It is important to understand the root causes of these outliers, and the limitations inherent in the measurement method. Understanding the root causes of these outliers is important if they are to be discarded with confidence. Understanding the limita-

tions of the measurement method used is necessary to choose the best method, and for analyzing reported results. For example, if the edge recession for a tool is increasing by 20 nanometers per pass, but measurement uncertainty is 50 nanometers, that experiment does not provide useful information.

The main contributions to measurement uncertainty for each individual plunge cut residual measurement are: horizontal resolution and measurement noise of the interferometric plunge measurements, and the uncertainty contribution of the alignment algorithms. The former are analyzed below, then used as inputs to develop the Monte Carlo model used to evaluate measurement uncertainty.

4.1 Horizontal resolution limits of the coherence scanning interferometer

Creation of plunge residuals begins with coherence scanning interferometer (CSI) measurements of each plunge in the data set. CSI allows the application of interferometric techniques to surfaces which are complex in terms of surface topography, using a non-contact method. Profilometry could provide similar measurement quality, but requires a stylus in contact with the workpiece and is slower in terms of data acquisition, This lower speed also makes the system more susceptible to temperature-induced errors. The horizontal resolution of the system chosen to measure the plunge cuts is a limiting aspect of the system. No features smaller than the effective system resolution can be observed, and the measurement data must be interpolated to perform the alignment processes described in Section 3.3.

All plunge measurements and any surface measurements shown in this document were taken using a ZeGage white light coherence scanning interferometer with a 1024×1024 pixel sensor. Vertical resolution of this instrument is on the scale of single digit nanometers. Horizontal resolution is on the order of one micrometer, but depends on the objective being used for a given measurement. Horizontal resolution is a larger barrier to these measurements because it makes interpolation of the data for fine alignment a requirement. Two objectives were used, depending on the mea-

surement being performed: a 0.40 NA 20x objective with a 420 µm field of view, and a 0.55 NA 50x objective with a 170 µm field of view. Instrument performance is different depending on the objective chosen, higher magnification objectives provide better spatial resolution and higher slope limits but at the expensive of smaller fields of view.

All plunge measurements used to calculate residuals were taken using the 20x objective. Measurements of surface finish or 'detail views' of portions of the plunge were often performed using the 50x objective.

Instrument resolution can be limited by the instrument's detector resolution, or by the optical diffraction limit. The detector resolution δ_{det} is the instrument field of view divided by the number of pixels. Sensor resolution for the two objectives used here is shown below.

$$\delta_{det}^{20x} = \frac{420}{1024} = 0.410 \ \frac{\mu m}{pixel} \qquad \delta_{det}^{50x} = \frac{170}{1024} = 0.166 \ \frac{\mu m}{pixel} \tag{4.1}$$

Any finite-aperture optic experiences diffraction, the effect is essentially a single-slit interference experiment in two dimensions. The diffraction pattern caused by this phenomenon is called an Airy disk, and the diffraction limited performance of an optic is described in terms of this Airy disk. When two Airy disks are sufficiently close, the system is said to be diffraction limited. The minimum distance between disks can be defined using either the Sparrow or Rayleigh criterion. The Rayleigh criterion (δR) states that when the maximum of one PSF meets the first minimum of the second PSF, the system is diffraction limited. The Sparrow criterion (δS) states that when the dip between the two Airy disks can no longer be seen, the system is diffraction limited.

Both are a function of the wavelength of the light passing through the system, and numerical aperture. The respective equations that approximate each are shown below.

$$\delta R = \frac{\lambda}{2 \cdot NA} \qquad \delta S = \frac{\lambda}{NA} \tag{4.2}$$

The Rayleigh criterion is used here simply because it is more conservative.

$$\delta R_{20x} = \frac{549\ nm}{2 \cdot 0.40} = 0.7\ \mu m \qquad \delta R_{50x} = \frac{549\ nm}{2 \cdot 0.55} = 0.5\ \mu m \tag{4.3}$$

The 20x diffraction limit is slightly more limiting than the sensor resolution, while the 50x diffraction limit is three times the detector resolution. However, a 3×3 convolution filter is applied at the hardware level to each pixel, this decreases measurement noise but effectively reduces the spatial resolution of the instrument. This provides a practical minimum horizontal resolution limit of 1.23 µm for the 20x objective, and 0.498 µm for the 50x objective.

4.2 Surface topography repeatability of interferometer

The primary limiting factor for vertical resolution of the interferometer is measurement noise. This is defined as instrument noise, which is the noise inherent in the instrument when operated in an ideal environment, combined with noise contributed by the environment. These external sources can include thermal effects, external vibrations, and air turbulence. One method of characterizing instrument noise is surface topography repeatability (STR). There are several possible definitions of this parameter. The one used here, defined in ISO 25718-604, is the pointwise standard deviation of N measurements. Instead of wrapping a representation of instrument noise into a single number, this allows for the measurement-specific nature of measurement noise to be expressed. The largest factor driving changes in standard deviation at each pixel of a measurement is the local slope of the part being measured. If the local slope is low, small horizontal movements of the stage cause small errors in the reported part

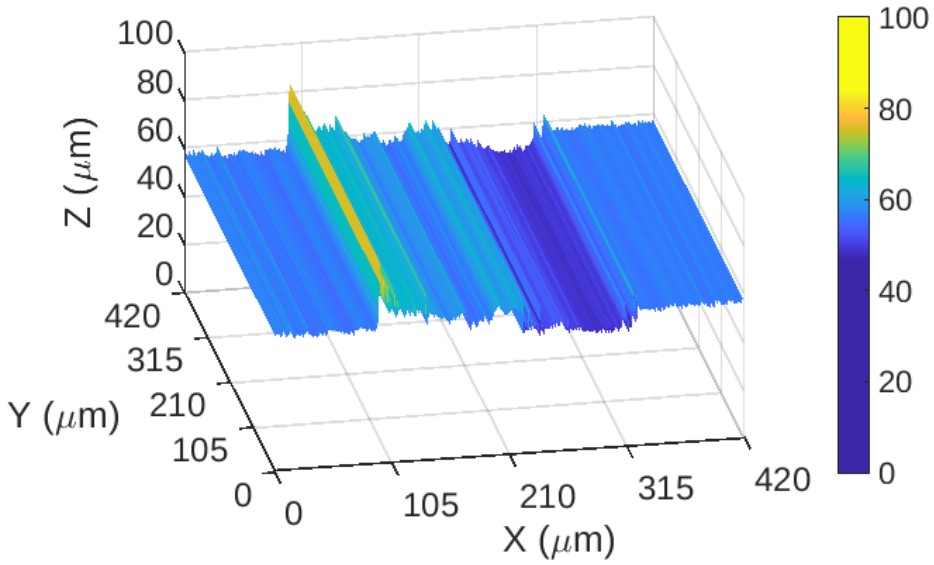

Figure 4.1: Pointwise standard deviation of twenty repeat measurements of one plunge, taken at ten second intervals.

height. When the local slope is large, the same small horizontal movement will cause a larger error in reported part height [59]. There are also spurious abberations proportional to slope [60]. This means that measurement uncertainty along the plunge is expected to be higher than on the flats, and highest at the plunge edge.

A measurement-specific STR measurement, as performed here, quantifies how the instrument and external environment will impact plunge measurements done using the same instrument, in the same environment. The STR measurement shown here was produced using twenty repeated measurements of the initial, unworn plunge of a new tool into copper from a wear experiment.

Since there is very little variation in the pointwise standard deviation along the Y axis, the phasemap is column-averaged to present '1-d' data. This both acts as a smoothing filter and presents a figure which is easier to interpret.

As predicted, the STR peaks is lowest on the flat surfaces to each side of the plunge. It is highest at the plunge edge and becomes lower towards the plunge center. This occurs because the local slope along the plunge edge decreases at x approaches 0.

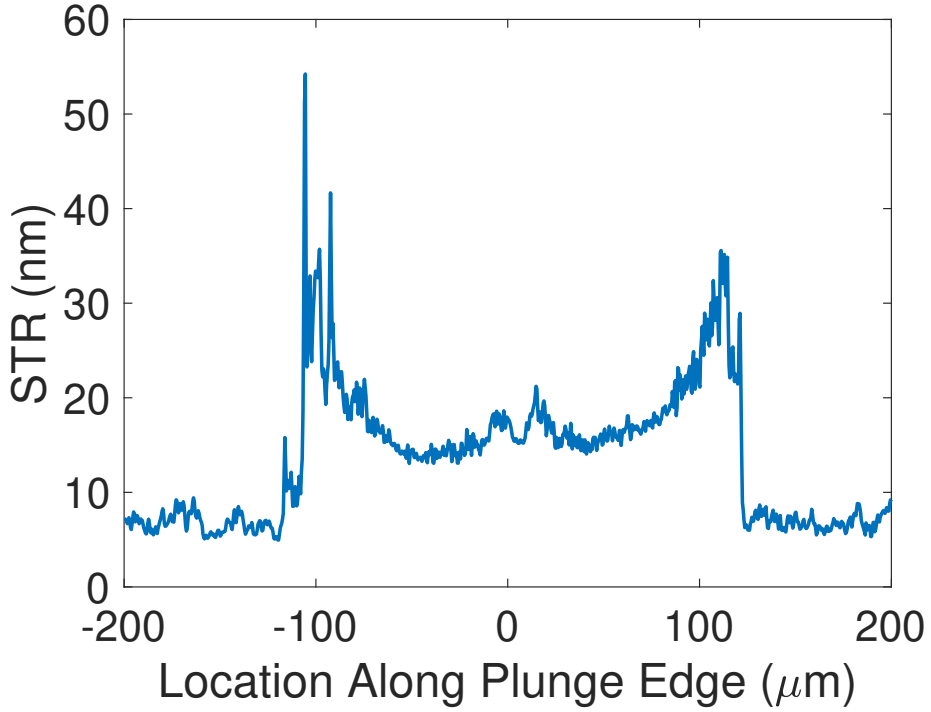

Figure 4.2: Surface topography repeatability of a typical plunge measurement. The spikes around ± 100 µm indicate the plunge edges.

4.3 Monte Carlo uncertainty analysis of plunge cut residual measurements

When it is difficult to combine every uncertainty contribution under a common unit, or there are cross-correlations between contributions that are difficult to account for, Monte Carlo analysis can be used to evaluate measurement uncertainty. This allows an uncertainty estimate to be derived from the functional relationship between input and output distributions by creating a distribution of inputs, running them through a model, and inspecting the distribution of outputs.

This Monte-Carlo analysis is carried out with respect to the measurand: position-dependent edge recession of the unworn diamond cutting tool. All contributions are evaluated as Type B uncertainties. A comprehensive list of classical evaluation for this measurement can be found in Evans [58]. The Monte Carlo approach used here assumes all contributions can be neglected except for noise in the SWLI measurement, pixel resolution, unworn tool quality, and the way these quantities influence errors

introduced by the alignment algorithms. The primary ways in which the alignment algorithms introduce measurement uncertainty are listed below.

1. Noise in the SWLI data acquisition. This is modeled using repeated SWLI measurements of an unworn plunge as a guide.

2. The plunges must be aligned to better than one pixel (440 nm), so the data needs to be interpolated. This makes assumptions about plunge form at higher spatial frequencies.

3. Rotation angle is determined by edge location. Small variations in the edge shape, perhaps caused by noise, influence the calculated angle. CSI noise is highest at the plunge edge due to steeper slopes.

4. The two described sub-pixel alignment algorithms are not perfect, neither align the plunges with 0 nm of lateral error.

5. Edge quality of the unworn tool can have a large influence on final align

The influence of edge quality has a binary nature. If the edge is good enough the uncertainty contribution is negligible, sufficiently poor and the data cannot be processed at all. Some types of defects cause no problems, such as small nicks or chips on the unworn edge, while the alignment process is extremely sensitive to others. The effect described here can be seen in Figures 4.8 and 4.9.

The uncertainty contributions of each final alignment algorithm must be considered separately, but the slope-based algorithm expanded uncertainty was evaluated analytically by Evans to be ± 6 nm at the nose, and ± 14 nm at the plunge edges [58]. This classical analysis serves as a 'sanity check' for the Monte Carlo approaches below. The distribution of height maps is then processed using the algorithms described in Section 3.3. Since each array is identical other than the simulated noise and coordinate transformations applied, perfect alignment should yield a series of reasonably

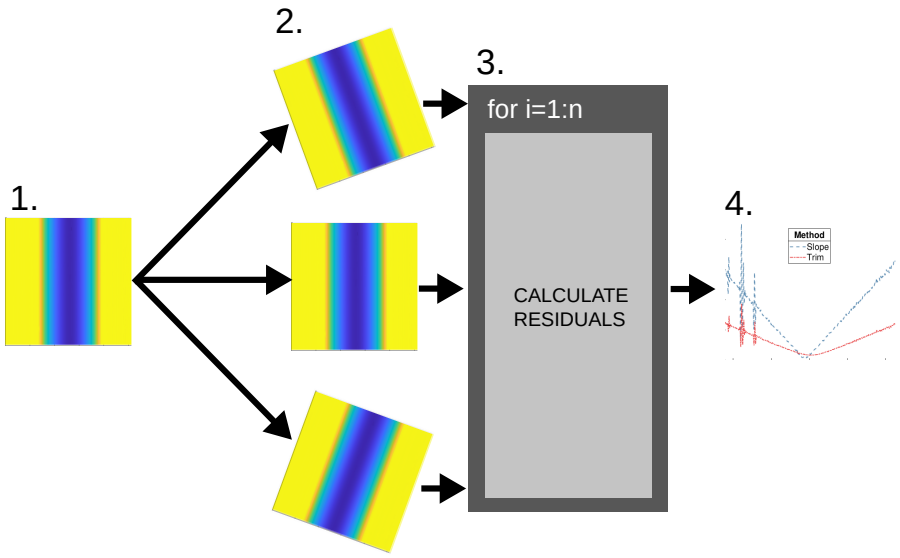

Figure 4.3: 1. Seed measurement used to create distribution of inputs, 2. Add piston, tilt, rotation, and shift, with the amount of each pseudo-randomly drawn from it's respective statistical distribution, take residual of each of these with respect to the seed measurement, 3. Find pointwise standard deviation of all residuals.

straight residuals with magnitude of the same order as the added noise. Since this will never be the case, the standard deviation of all residuals at each x position along the plunge edge is taken and doubled, giving expanded measurement uncertainty (k=2), shown in Figure 4.5.

4.3.1 Input distributions for Monte Carlo uncertaintuy analysis of cutting edge measurement

The Monte Carlo analyses for each alignment method are performed by generating a distribution of input height maps, using a CSI measurement of a reference plunge as the input. A distribution of 1000 height maps is created by adding, in the following order, pseudo-randomly generated lateral shift, piston, tilt, rotation, and measurement noise to the original data. The distributions used for each input and their respective bounds are shown in Table 4.1. The maps are shifted using the MATLAB function `circshift`, tilted by generating a plane from a normal vector where the

Table 4.1: Table of input distributions for Monte Carlo simulation

Type	Distribution	Bounds	Unit
Piston	Uniform	± 1	µm
Tilt	Uniform	± 0.1	deg
Rotation	Uniform	± 5	deg
Meas. noise	Butterfly	± 1[a]	nm
Lateral shift	Uniform	± 4.11	µm

[a] Value from distribution is added to each point on the STR map.

angles associated with each direction cosine are drawn from the distribution, and rotated using the MATLAB function `imrotate`. The inputs for each of these steps are drawn from the associated distribution. The noise distribution is generated by adding small random variations to the surface topography repeatability (STR) measurement of an unworn plunge. The STR used for this purpose is shown above in Figure 4.2.

4.3.2 High frequency surface feature near plunge edge

There is often a high-frequency surface feature found near the plunge edge that interferes with the final alignment process. When using the slope alignment process it creates a bias in the slope measurement, and when using the edge alignment process it makes choosing a width at which to trim the plunges problematic.

This is caused by feeding the tool too slowly during plunge creation, which causes burnishing. This burnishing (or rubbing) effect pushes material outward from the middle of the plunge, until it reaches the point where the plunge and workpiece surface intersect. When the material reaches this point it must change direction to continue moving, this impediment to motion causes it to bunch up. This has two effects: the high frequency content being discussed here, and formation of a burr where the plunge meets the flat surface. The magnitude of this effect could also be related to cutting edge sharpness. At a given infeed rate a duller tool should experience more burnishing, and a sharper tool less.

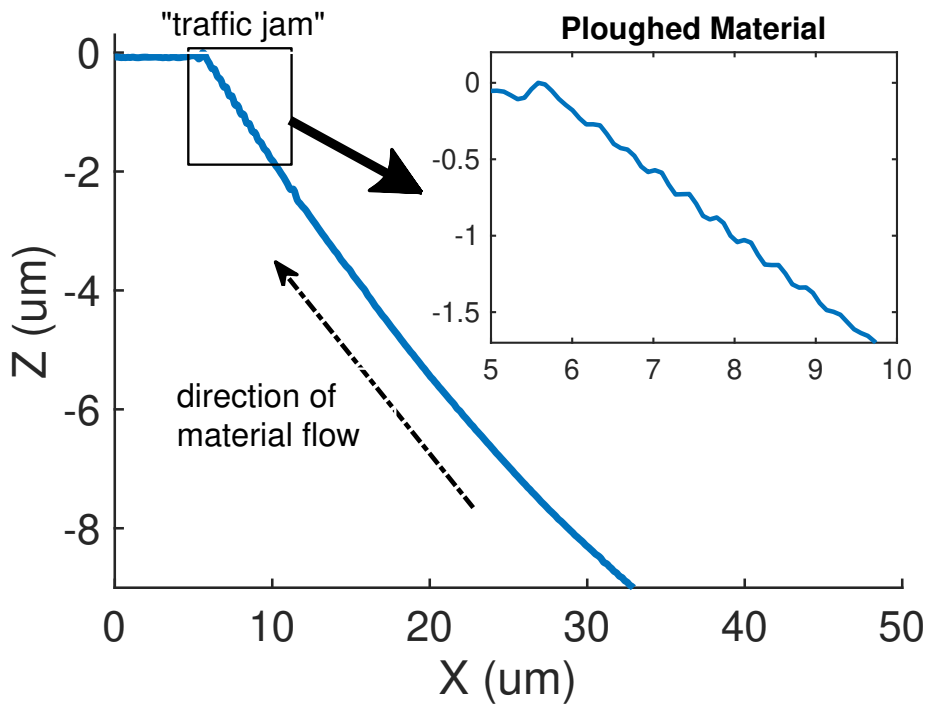

Figure 4.4: Profile from 50x measurement of a plunge where a burr was present on the plunge edge. Both the burr and the material bunching up below can be seen.

4.3.3 Results of Monte Carlo analysis

Expanded uncertainty for the sag method ranges from 3 nm to nearly 30 nm, if the high frequency spikes along the unworn edge are not discounted. These are either the result of a burnishing effect (as discussed above), or artifacts of the relapping process that are generally not present on a new tool. The chosen f value for Equation 3.2 should always be some multiple of the spatial sampling to minimize tilt error. Measurement uncertainty for the slope alignment method ranges from less than 1 nm to over 40 nm. There is also a slight offset from zero because only the unworn plunge edge is used for alignment, introducing asymmetry.

It would be interesting to repeat this process with a profilometer. Data could only be collected for one 'slice' of the plunge, but could be collected at a much higher spatial frequency and all plunges would be on the same reference coordinate system, obviating the need for tilt and rotation registration. These advantages are somewhat

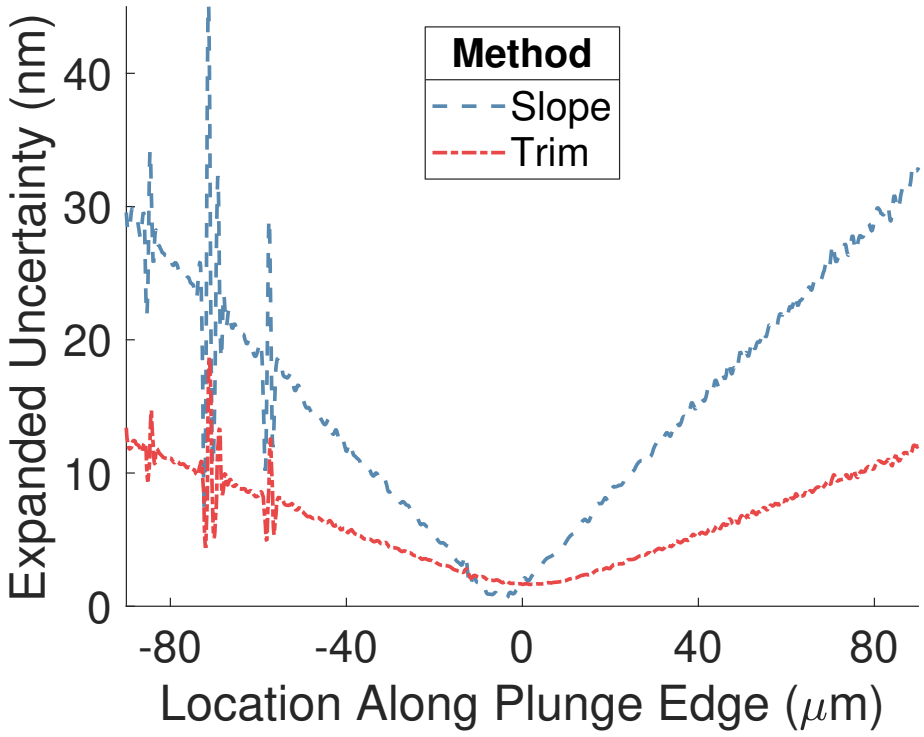

Figure 4.5: Results of Monte Carlo uncertainty evaluation ($k = 2$).

offset by the morphological filter inherent in any profilometer measurement.

4.3.4 Discussion of measurement uncertainty results

Measurement uncertainty is position-dependent, and increases with distance from the nose of the cutting tool. The slope alignment algorithm causes a small lateral shift in the uncertainty distribution, which is interesting but of little practical consequence. The evaluated measurement uncertainty for both methods is reasonable, but the trim method is nearly a factor of three better and should be used for future processing of plunge residuals. The position-dependence implies that when wear rates are low, analysis using nose wear data will yield better results than analysis performed with edge wear data. In general, higher wear rates will provide data that is easier to interpret and analyze. Lower measurement uncertainty allows the investigation of lower rates of wear.

Checking the results of the Monte Carlo evaluation against a real measurement (Fig-

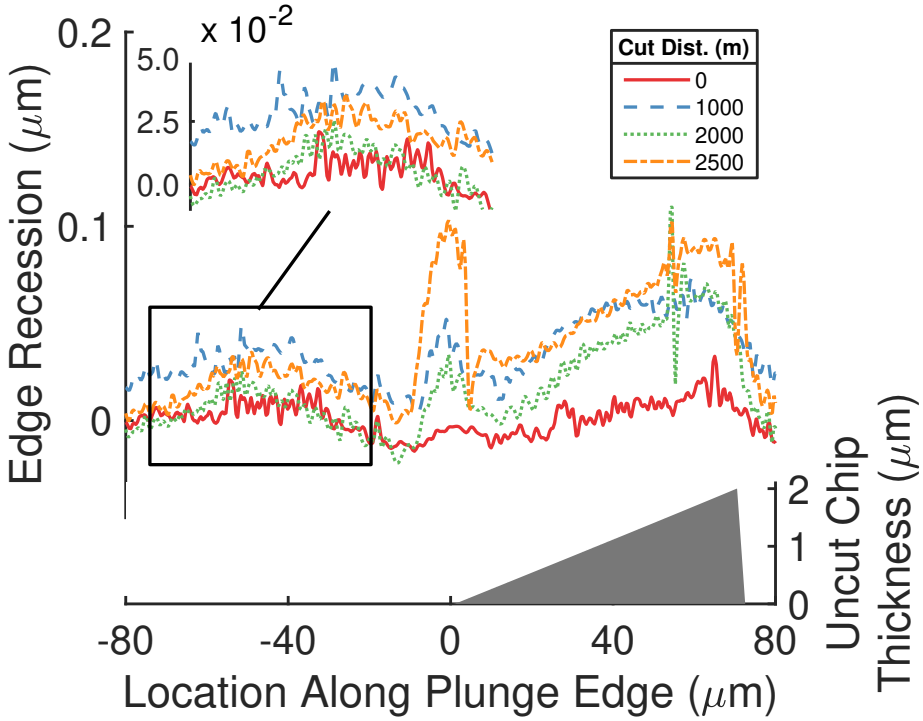

Figure 4.6: Example of alignment quality with real data from an experiment. This tool has a 'rough' edge but aligns to 30 nm or better.

ure 4.6) supports the result shown in Figure 4.5. This is the residual shown in Figure 4.9, with the unworn edge shown in the inset. The residual was prepared using the trim alignment method. This is a good residual to check against because there is high-frequency content in the tool shape that makes good alignment difficult. Superficially, this residual looks poorly aligned, but inspection of the inset shows that misalignment is never greater than about 30 nanometers. This is slightly outside of the three sigma ($k = 3$) interval for the uncertainty evaluation, reinforcing the effect that high-frequency content has on the quality of the measurement.

4.4 Investigation of experimental outliers

There are three possible root causes for the outliers: an insufficiently sharp cutting edge, form, waviness, or roughness error in the tool radius, and dislocations or other structural problems in the diamond lattice. Cutting edge sharpness refers to the actual cutting edge (Figure 4.7), while tool radius refers to the radius of the rake face

(500 µm for these experiments). A dull cutting edge or excessive deviations in the tool radius could both cause wear to occur more rapidly than expected. These two problems would be a product of the manufacturing or resharpening process. When a tool is resharpened it is often only relapped–this is the process of polishing the rake face until the cutting edge appears to be sufficiently sharp. An additional step is to re-cone the clearance face, if a tool has experienced large amounts of wear both processes may be necessary to completely resharpen the tool.

A few simple tests can be used to narrow down the possible causes of a given outlier. First, is there significant form, waviness, or roughness error in the tool radius, especially near a point of abnormally high wear? If yes, does the wear rate decrease after relapping *and* re-coning the tool and repeating the experiment? If the wear rate decreases then the abnormally high wear rate in the first experiment can be attributed to a poorly sharpened tool. If the wear rate remains high compared to other tools, it is likely there is a dislocation in the crystal lattice or other structural problem with the diamond on that particular tool, and it should no longer be used at that angle of rotation.

Figure 4.7: Side view of diamond. Cutting edge sharpness refers to the nanometer-scale radius of the cutting edge emphasized by the black circle.

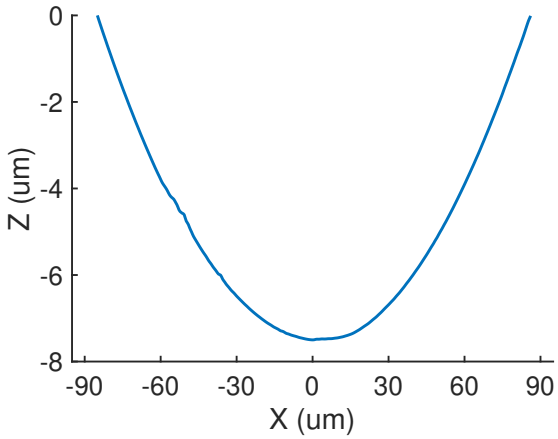

(a) Unworn tool plunge of poorly sharpened tool. This is visible at the nose, and on the trailing edge at x =-60 µm.

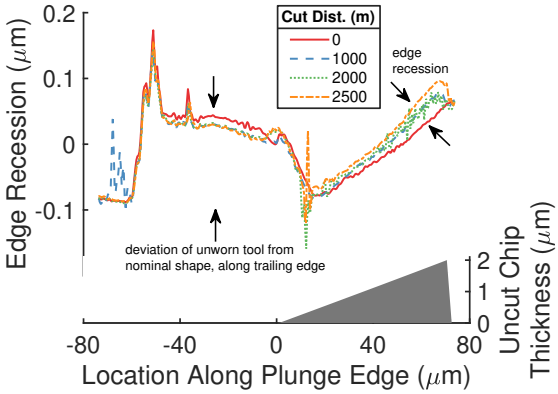

(b) Corresponding residual measurement.

Figure 4.8: The first (unworn) plunge from an experimental data set and the corresponding edge recession measurements. The tool was normal to the workpiece for this experiment. A large piece missing from the trailing edge appears to have not caused excessively high edge recession, but does make decent final alignment impossible.

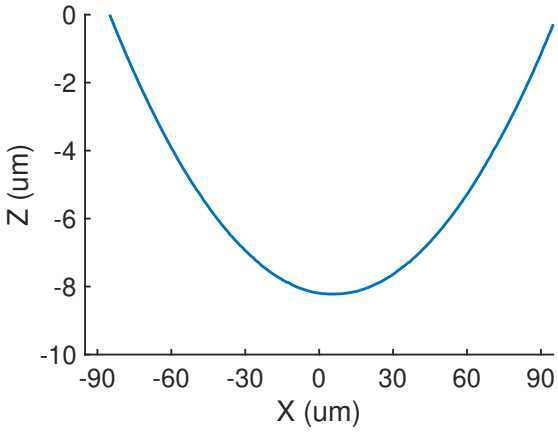

(a) Unworn tool plunge of poorly sharpened tool. This is visible at the nose, and on the trailing edge at x =-60 µm.

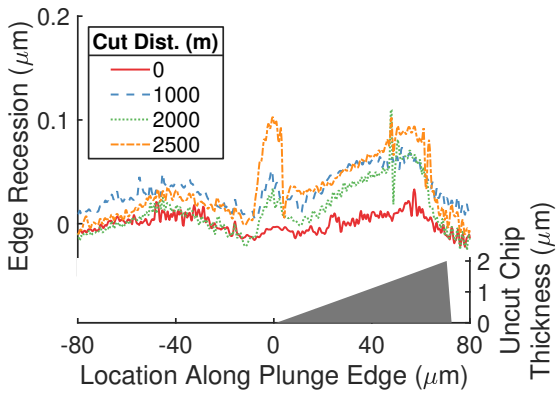

(b) Corresponding residual measurement.

Figure 4.9: The results of repeating the experiment, using the same tool shown in Figure 4.8, after being relapped and reconed. There is still error visible, but it is on the order of 10 nm.

CHAPTER 5: CUTTING FORCES WHEN DIAMOND TURNING CU-NI ALLOYS

This chapter reviews the model of cutting forces in oblique turning and facing with diamond tools, and discusses the cutting forces encountered during plunge cut experiments. In the context of this research, force measurement is useful for understanding the relationship between cutting forces and tool wear in the materials being machined. It is also useful for identifying tools which have worn prematurely, or other anomalies that occur during experiments, (such as unacceptable build up of chips on the rake face) in real time. The models developed here are not new, and are based upon the analyses found in [61] and [62].

5.1 Cutting mechanics and force model for diamond turning metals

When single point diamond turning with a radiused tool a stationary tool is fed into a rotating workpiece. The tool penetrates the workpiece to a certain depth of cut h, and spindle rotation causes the workpiece to move past the tool normal to the rake face with a certain cutting speed v_c. To remove material, the tool then feeds parallel to the workpiece surface at a feedrate f. A schematic of all this, sans the rotating workpiece, is shown in Figure 5.1.

In orthogonal turning the cutting geometry results in a rectangular chip with an area $A_c = f \cdot h$. In round nosed turning, shown here, the chip thickness varies along the cutting edge radius. For small feed rates the thickness as a function of theta is approximated by $t_c(\theta) = f \cdot \sin(\theta)$ (Figure 5.2). The cutting force can still be estimated as proportional to the area of the uncut chip, which is closely approximated by $A_c = f \cdot h$. The thrust force is approximated by estimating the resistance given by

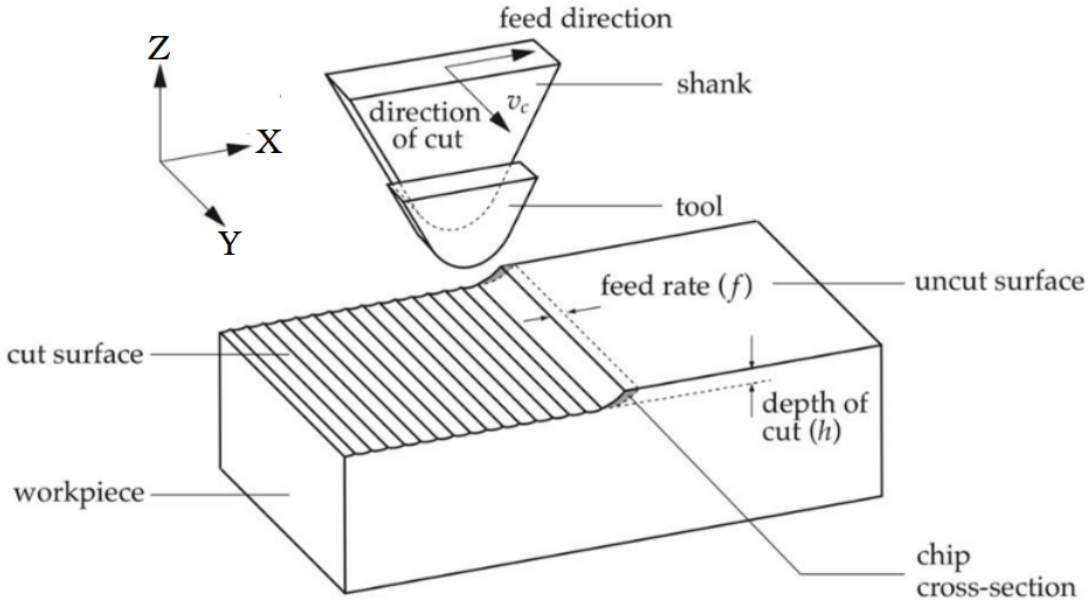

Figure 5.1: Cutting mechanics of single point diamond turning [2] and coordinate system for cutting (F_y), thrust (F_z), and feed (F_x) forces.

the chip sliding along the rake face as μ times the normal force (which is the cutting force).

This yields a basic model of cutting force:

$$F_c = A_c K(t_c) \tag{5.1}$$

$$F_t = \mu A_c K(t_c) \tag{5.2}$$

where A_c is the uncut chip cross-sectional area, μ is the friction coefficient between diamond and the material being machined, and K is a process coefficient which s likely to be a strong function of uncut chip thickness [63]. For metals the process coefficients is strongly correlated with material hardness. This relationship has been shown experimentally by Carroll et. al. [64].

Material hardness can be estimated as three times the yield strength. For Monel,

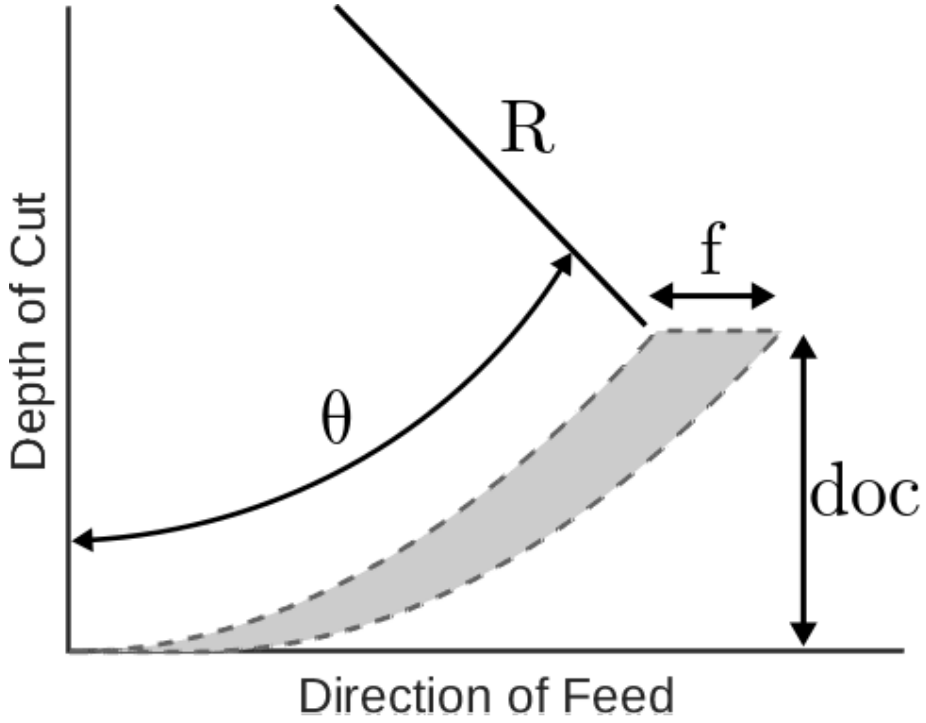

Figure 5.2: Uncut chip thickness increases with θ.

this gives an estimated cutting force for an unworn tool of

$$F_c = 2\ \mu m \cdot 5\ \mu m \cdot (3 \cdot 550\ MPa) = 16.5\ mN \tag{5.3}$$

This estimate does not account for strain hardening of the workpiece from previous machining operations or the cutting edge radius, both of which can have a substantial effect on the force levels the tool experiences. Although μ generally less than one for most material combinations, the chemical affinity between diamond and Cu-Ni alloys may lead to adhesion and correspondingly high values of μ [65].

5.2 Collection of cutting force data

Cutting force was measured using a Kistler MiniDyne dynamomometer attached to the tool post with an adapter plate as shown in Figure 5.3. Force data was recorded continuously during the entire experiment, then chopped for processing as described in the next section.

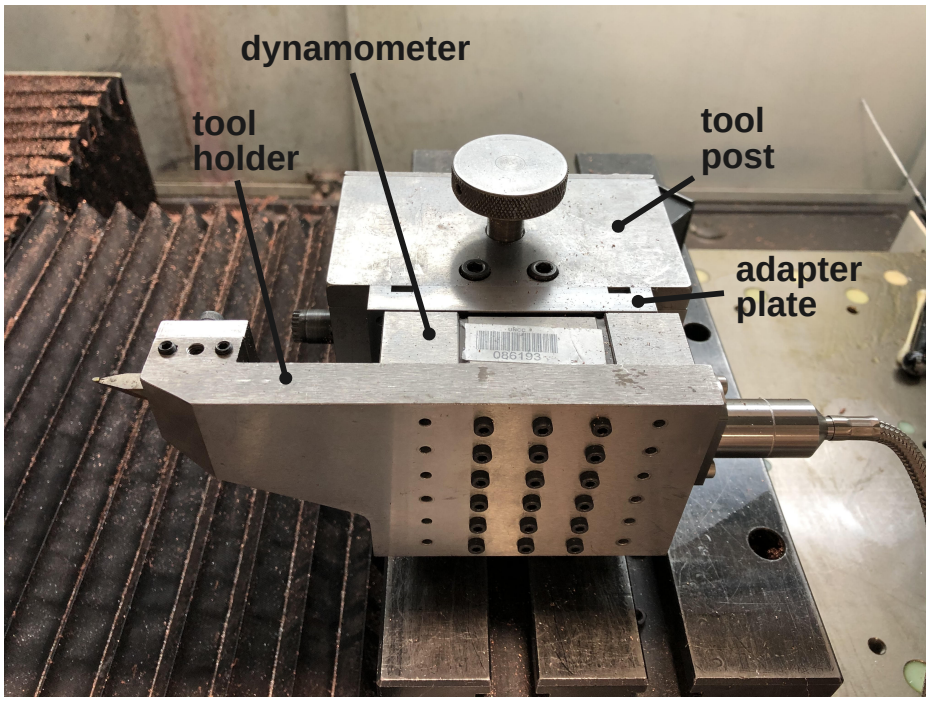

Figure 5.3: Setup for force measurement. The dynamometer is inserted into the tool post structural loop using an adapter plate. The tool is also clamped from the top and side.

Cutting (F_y), thrust (F_z), and feed (F_x) forces are acquired for each plunge into the copper witness sample, and facing pass of the Monel workpiece (Figure 5.1). The force reference frame is fixed at the tool tip. All force data was acquired at 1000 Hz and filtered in real time with a low-pass 50 Hz Butterworth filter. This value was chosen because it filters 60 Hz electrical noise, but is three times greater than the spindle rotation frequency (1000 rpm = 16.67 Hz). This allows the largest noise sources to be filtered while still retaining information about the spindle harmonics.

5.3 Processing of cutting force data

After acquisition two continuous time series, one for thrust force and one for cutting force, are exported MATLAB. Feed force is extremely low and not particularly sensitive to tool wear, so it is discarded for all experiments. These time series are then chopped into $N-1$ sets of facing pass data, and N sets of plunge data. The value of N is six for most experiments. Each of these time series is then processed

by: correcting for piezo drift, aligning with respect to time, and filtering using a rectangular moving average filter with a width of 0.2 seconds. This final step is only performed to make the figures shown here easier to inspect.

Piezoelectric force sensors work by producing an electric charge proportional to the stress induced in the piezoelectric crystal. This will also be proportional to the input force, and can produce precise force measurements down to the milli-newton scale. Accuracy of force measurements is driven by three factors: calibration, signal drift due to charge leakage, and measurement noise. The dynamometer used in these experiments includes a NIST-traceable calibration certificate. However, piezoelectric dynamometers are only capable of measuring dynamic or quasi-static forces. No matter how well electrically insulated the system is, charge will leak through the path of least resistance. For a static force measurement this charge leakage will eventually result in a measurement of zero newtons, when the dynamometer is still under load. The rate of this drift is defined by a time constant, the value of which is driven by the capacitance and resistance in the cable connecting the dynanometer to the signal conditioner, and the capacitance and resistance of the signal conditioner itself.

Drift is measured by taking a least squares linear fit of the first five seconds of data before the tool is in contact with the workpiece, then subtracting this fit from the entire data set. The drift is not guaranteed to be constant, but for cutting forces the measured drift from 0-5 seconds (shown in Figure 5.4) is -1.22 mN/sec, and measured drift over the final five seconds is -1.26 mN/sec. The variation in drift between the beginning and end of this measurement is 0.04 mN/sec. It should be noted that the drift rate differs subtantially for each axes of the dynamometer, and that cutting and thrust axes drift rates were calculated separately. Typical measurement noise, after real-time filtering but before the moving average filter was applied in post-processing, was estimated by taking the drift-corrected standard deviation of the first two seconds of data for several force measurements. This value was on the order of 2 mN for all

measurements. Recording data over long time periods and errors in correcting drift data can both compound this. On a time scale of fifteen seconds or less, the variation in drift from start to finish of the measurement is far smaller than the measurement noise. On this time scale the primary limit on measurement accuracy is noise in the signal.

5.4 Measurement of thrust and cutting force with tool normal to workpiece

Measured cutting forces, and the associated residual measurement, are presented here for a tool oriented normal to the workpiece. These results are typical of experiments where edge recession is not excessive. It should be noted that the edge radius measurements given here contain significant measurement error.

5.5 Investigation of the relationship between wear rates, cutting force, and edge sharpness

Both the predicted cutting force and rate of edge recession are expected to correlate with cutting edge sharpness. A theoretical maximum sharpness of single-digit nanometers (or better) is possible [66][67], but unlikely. The sharpening process, operator skill, and process variations all impact the final cutting edge sharpness. Published edge radii measurements for unworn tools performed using EBID or AFM measurements range from 23 nm [42] to over 200 nm [43]. Edge radii on the order of half a micrometer may not be uncommon in everyday use (personal communication Dave Keller).

To investigate the relationship between edge recession rates, plunge and cutting forces, and sharpness of the tool's cutting edge, a wear experiment was performed using a newly relapped and reconed tool. The standard experiment parameters described in Chapter 3 were used. Atomic force microscope measurements of the tool's cutting edge were taken before and after the experiment. Force data was recorded and processed as described above.

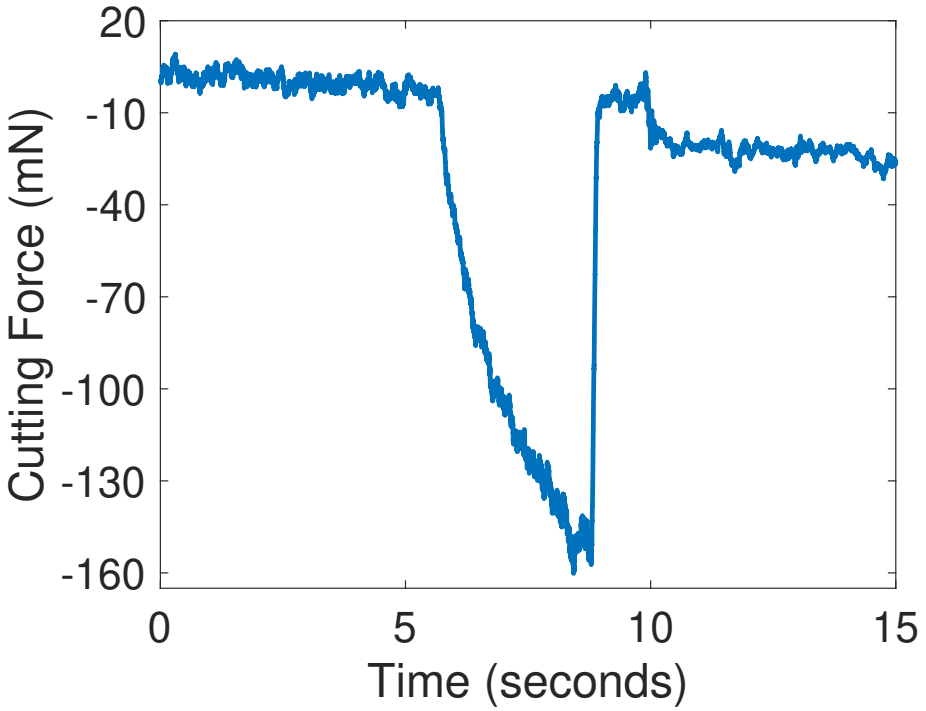

(a) Uncorrected plunge cutting force measurement. Drift is corrected by subtracting a linear fit to the first four seconds of data from the entire data set.

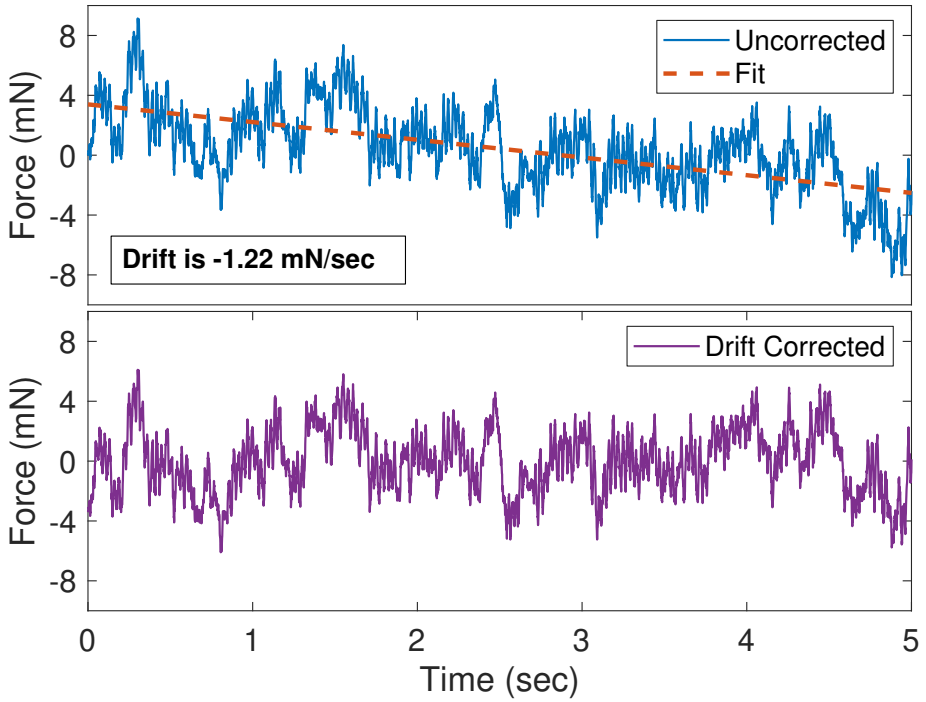

(b) Using the first five seconds of data to measure and correct drift.

Figure 5.4: Typical plunge cut force measurement before drift correction and the associated drift correction process. The drift is *not* linear over long δt. Each plunge only lasts for three seconds so the problem is minimal, but must be considered.

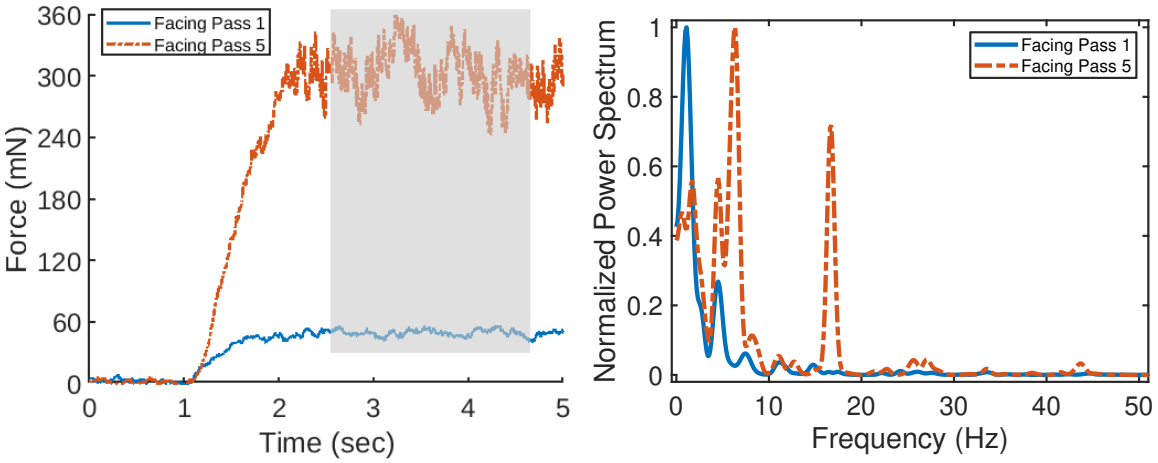

(a) Cutting forces for pass one and pass five from Figure 5.6a, before filtering. The gray box represents the two-second window used for power spectrum calculation.

(b) Power spectrum corresponding to the two windowed segments. Note the spike at 16 Hz on pass five, when the wear rate is higher.

Figure 5.5: The first and final facing passes from Figure 5.6a, before filtering, and the power spectrum associated with each. The low-frequency peaks may be associated with noise in the spindle drive current.

The proposed hypotheses are that:

1. there is a relationship between initial cutting edge radius and edge recession rates, and

2. there is a relationship between cutting edge radius and measured plunge and thrust forces.

Cutting edge radius was measured by taking a trace of the cutting edge from an AFM measurement, then fitting a circle to the section of the trace which represents the cutting edge. Measurement uncertainty is not evaluated in detail here, but the primary contributors are AFM scanner error, thermal drift, electronic noise, and the AFM tip radius.

Fitting a circle to the unworn cutting edge gives a cutting edge radius of 422 nm. This is too large to be reasonable. Measured cutting and thrust forces when plunging into the UBAC witness sample are presented below. The relationship between measured force and edge recession is also shown.

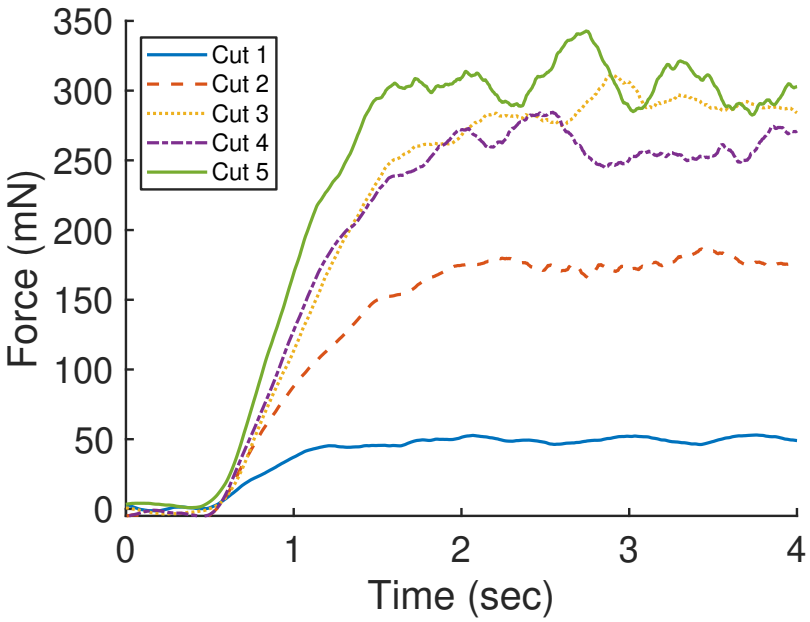

(a) Thrust force vs. time when facing Monel with the cutting tool oriented normal to the workpiece.

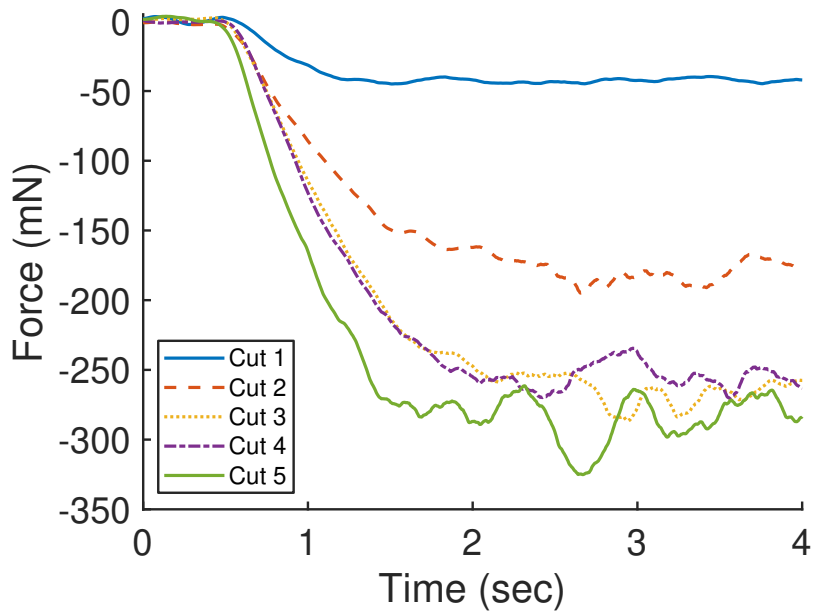

(b) Cutting force vs. time when facing Monel with the cutting tool oriented normal to the workpiece.

Figure 5.6: Typical thrust and cutting forces when facing Monel at 5 µm depth of cut and a feed rate of 2 µm/rev.

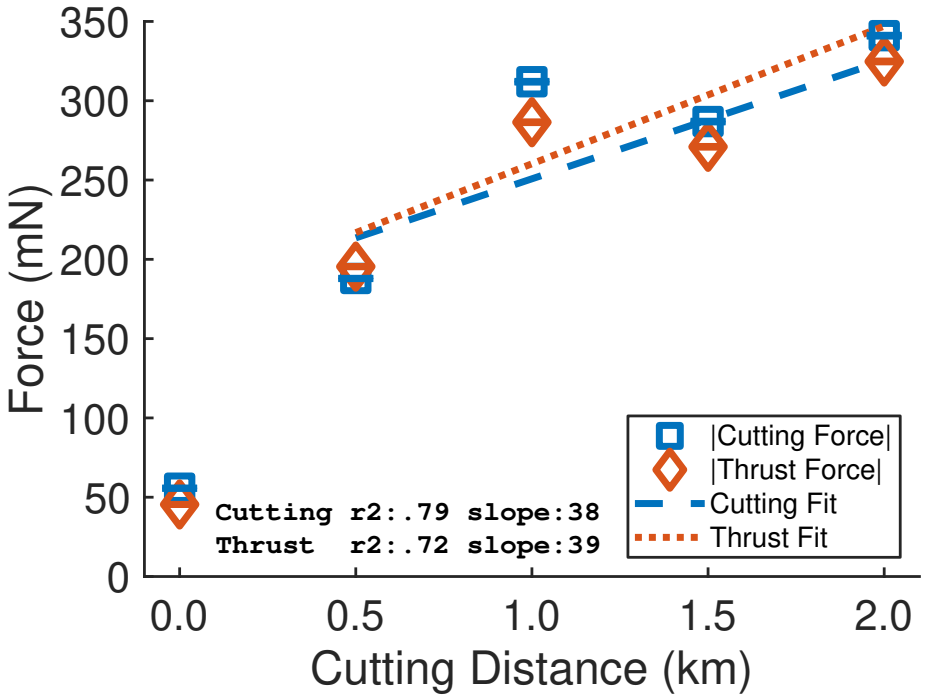

Figure 5.7: Absolute value of average cutting and average thrust force for each facing pass from Figure 5.6. Absolute value is used so that the rate trends can be compared on the same plot. Each data point represents the average from two to four seconds.

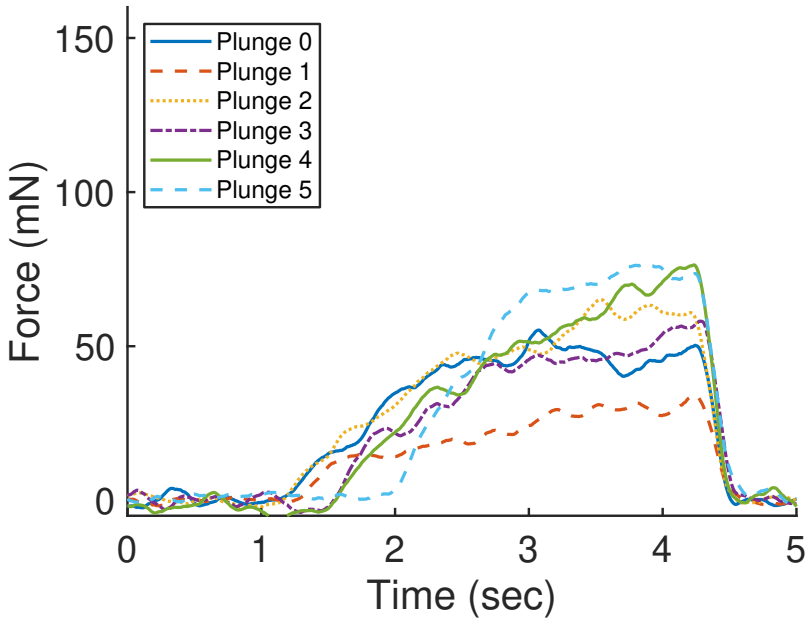

(a) Thrust force vs. time when plunging into UBAC copper with the cutting tool oriented normal to the workpiece.

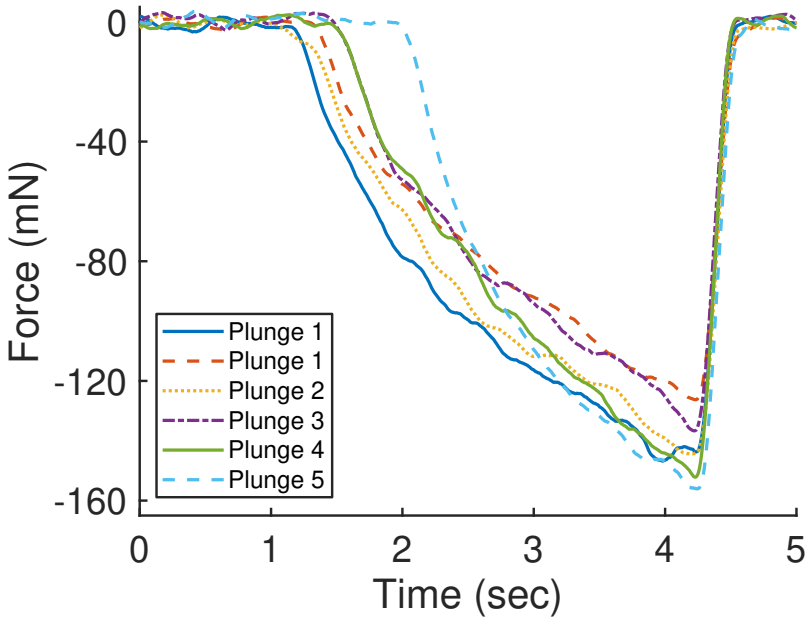

(b) Cutting force vs. time when plunging into UBAC copper with the cutting tool oriented normal to the workpiece.

Figure 5.8: Typical thrust and cutting forces when plunging into UBAC copper at 50 nm/rev.

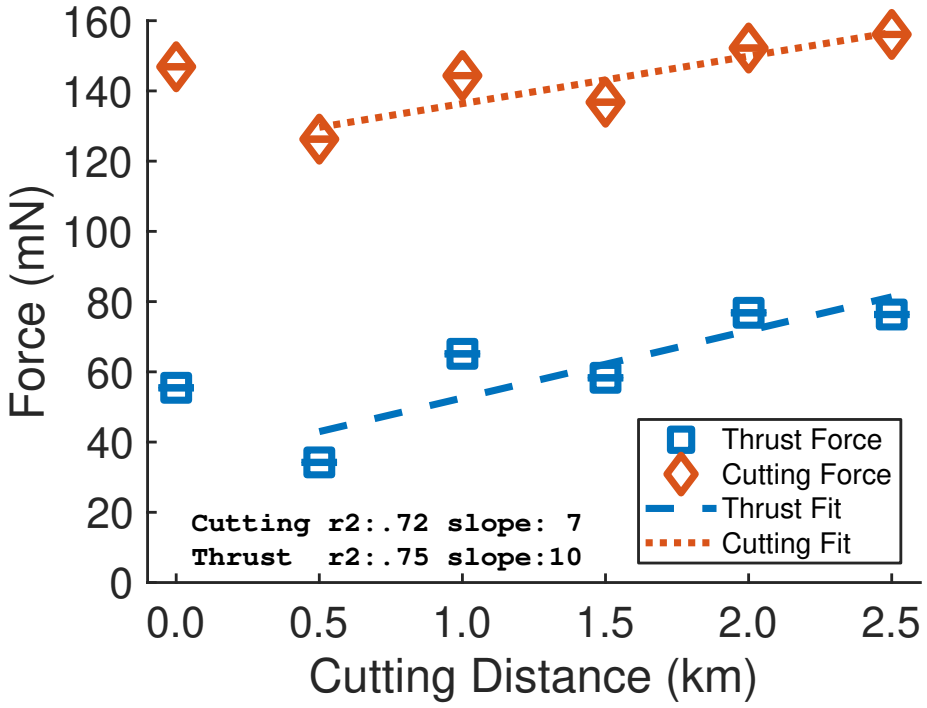

Figure 5.9: Absolute value of peak cutting and peak thrust force for each plunge from Figure 5.8. Absolute value is used so that the rate trends can be compared on the same plot. Each data point represents largest force value recorded during each plunge.

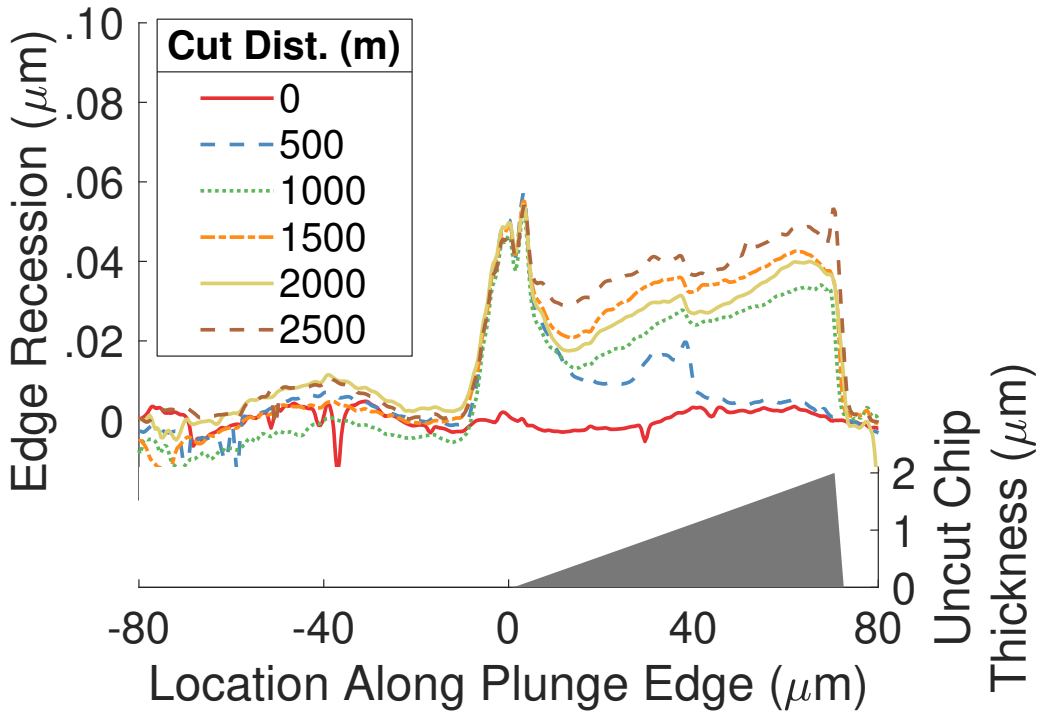

Figure 5.10: Tool wear residual from the experiment where the force data in Figures 5.6 through 5.9 was recorded.

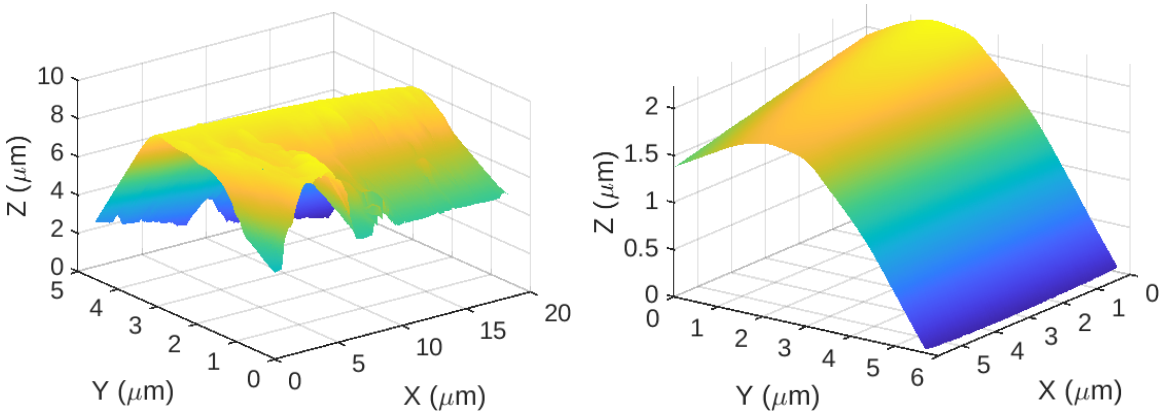

(a) Full scan of a section of the cutting edge.

(b) Zoomed in on a clean subsection of the edge to obtain a trace. The trace is 'sliced' along the Y axis.

Figure 5.11: AFM measurement used to measure cutting edge radius.

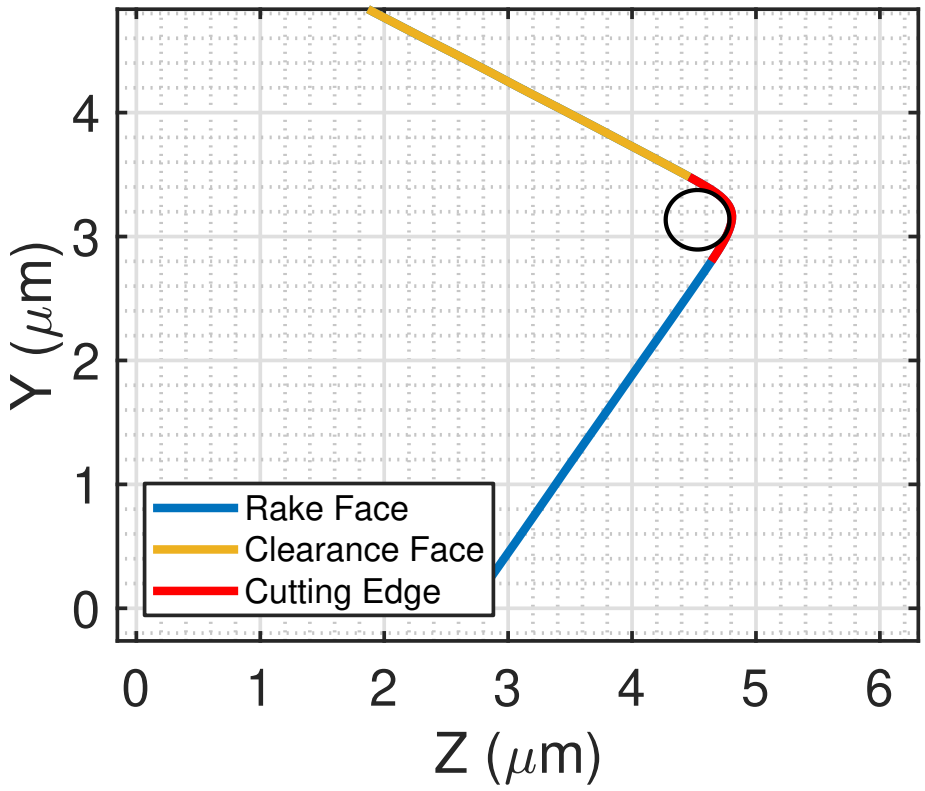

Figure 5.12: Profile of cutting edge from previous figure.

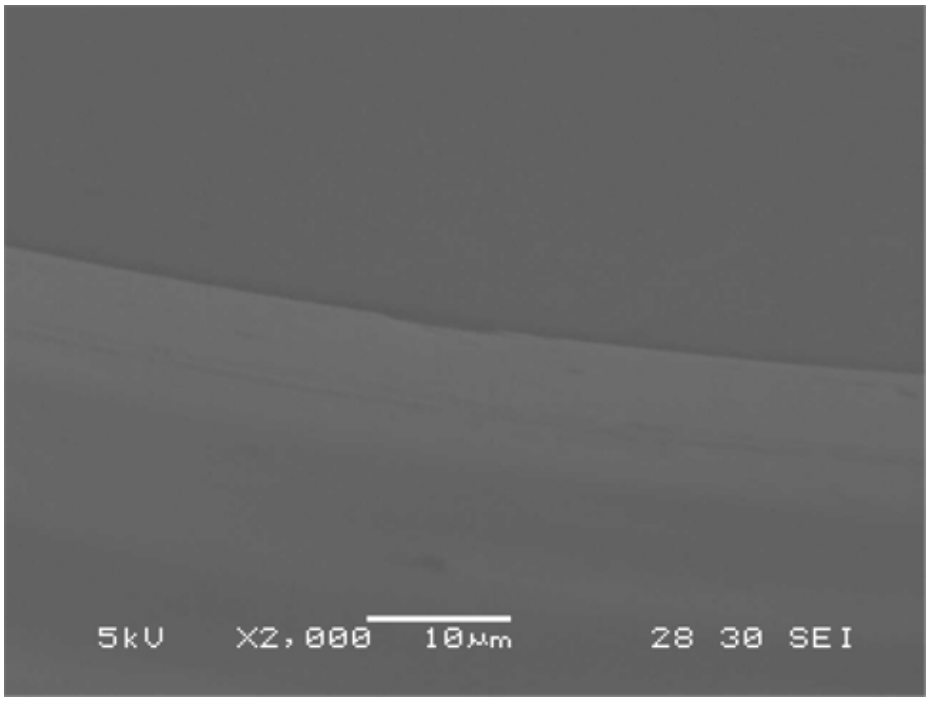

Figure 5.13: SEM measurement of the unworn cutting edge. There is a defect in the middle of the field of view.

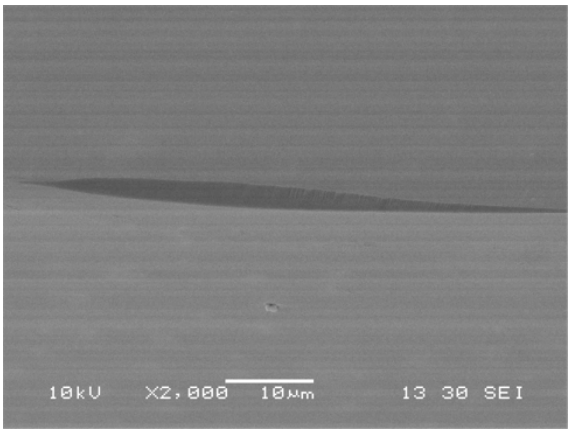

(a) Wear land at 2000x.

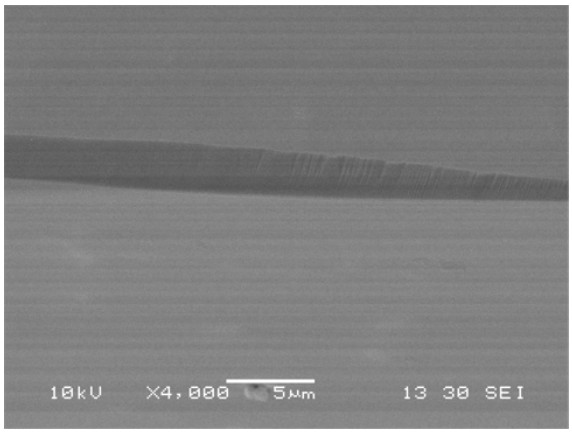

(b) Portion of wear land at 4000x. Periodic structure can be seen near the nose.

Figure 5.14: SEM measurements of the worn cutting edge. Leading edge wear is to the left, and nose wear is to the right.

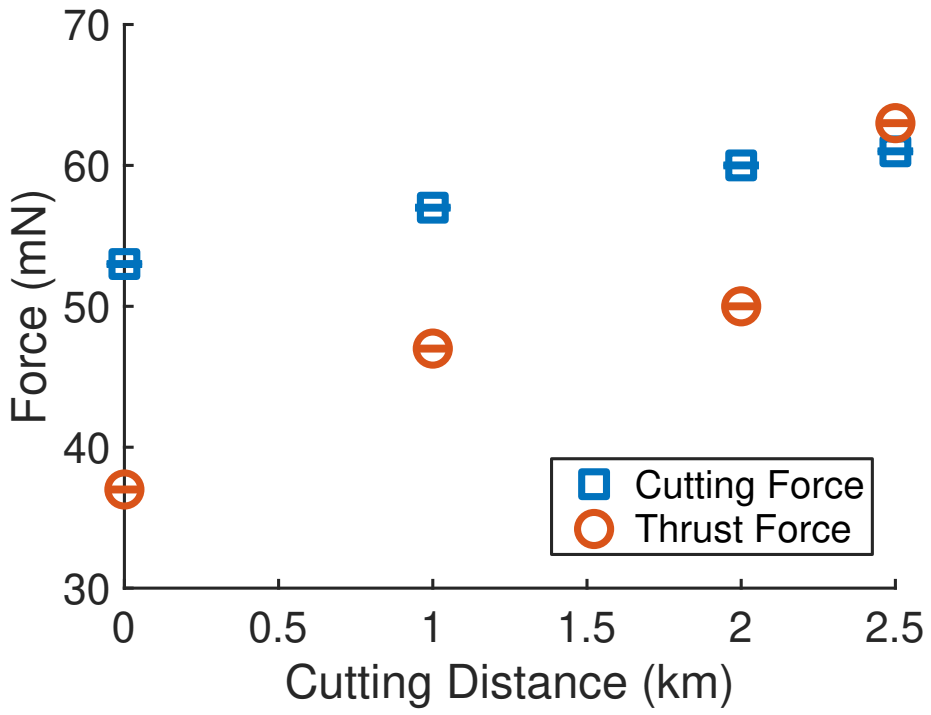

Figure 5.15: Peak cutting and thrust forces when plunging into copper as a function of cutting distance, from Figure 5.10.

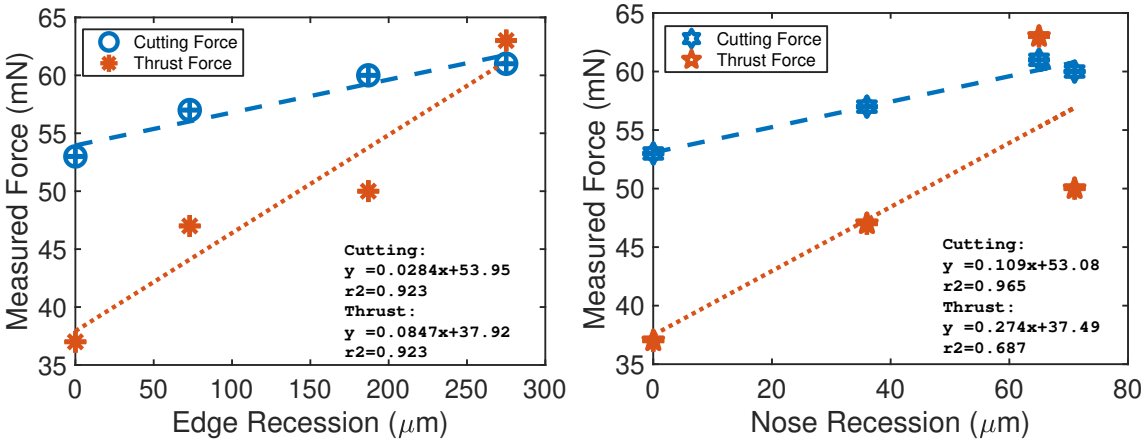

(a) Cutting and thrust force plotted against leading edge recession at $x = 63$ µm

(b) Cutting and thrust force plotted against nose recession at $x = 0$ µm

Figure 5.16: Plots of the relationship between cutting edge recession and measured forces.

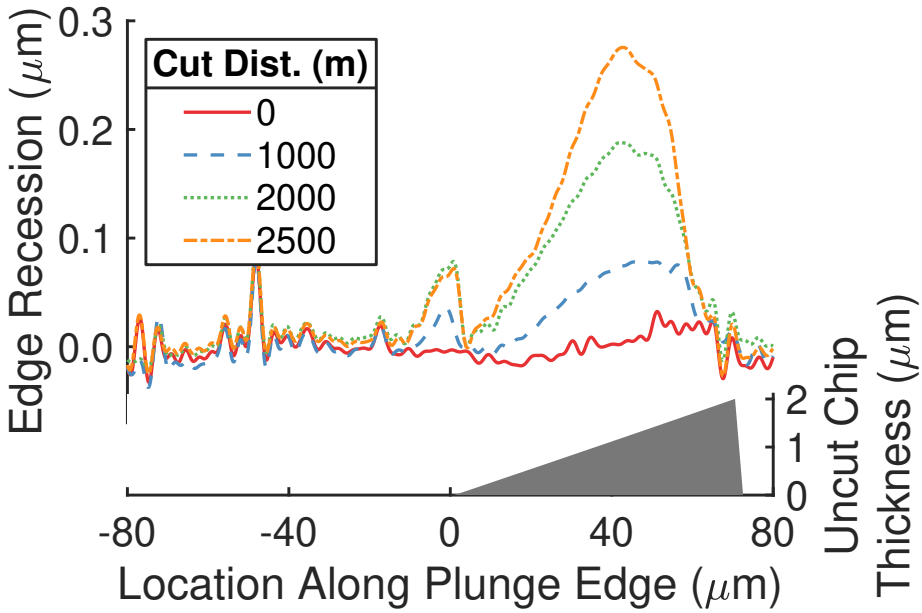

Figure 5.17: Residual for experiment described in this section.

5.6 Discussion of cutting force data

Measured cutting forces on the diamond when facing Monel ranged from 50 mN for the unworn tool to over 300 mN during the final cutting pass. This is higher than predicted by the theoretical model presented, but that model does not account for the effects of strain hardening. The thrust and cutting force values were very similar, implying a coefficient of friction between diamond and Monel of approximately $\mu = 1$. After an initial wearing-in period the force increased in a linear fashion between facing passes, although chatter increased with greater edge recession. Investigation of this wearing-in period is a good candidate for future work.

Measured cutting forces on the diamond when plunging into UBAC copper ranged from 120 mN to 150 mN. Thrust forces were substantially lower, implying a much lower coefficient of friction. Surprisingly, the lowest forces were not on the first plunge. This behavior remains unexplained. The measured forces were overall lower for UBAC, and also increased more slowly as a function of cutting distance.

There appears to be a strong, linear correlation between edge recession and measured forces when plunging into UBAC copper. The correlation is more consistent for edge recession than for nose recession, but the magnitude of edge recession for this particular experiment was much greater. This may simply be a signal/noise ratio problem, compounded by the measurement uncertainty limitations of the plunge cut residual measurement. This thought is reinforced by inspecting Figures5.17 and 5.16b and noting that for the last pass, edge recession appears to decrease (which does not make physical sense). The SEM images show no evidence of built up edge. This correlation is interesting and deserves further investigation.

CHAPTER 6: DIAMOND EDGE RECESSION AS A FUNCTION OF CUTTING DISTANCE

The purpose of this chapter is to investigate the questions: what is the relationship between nose recession and cutting distance, and what is the relationship between edge recession and and cutting distance with respect to uncut chip thickness?

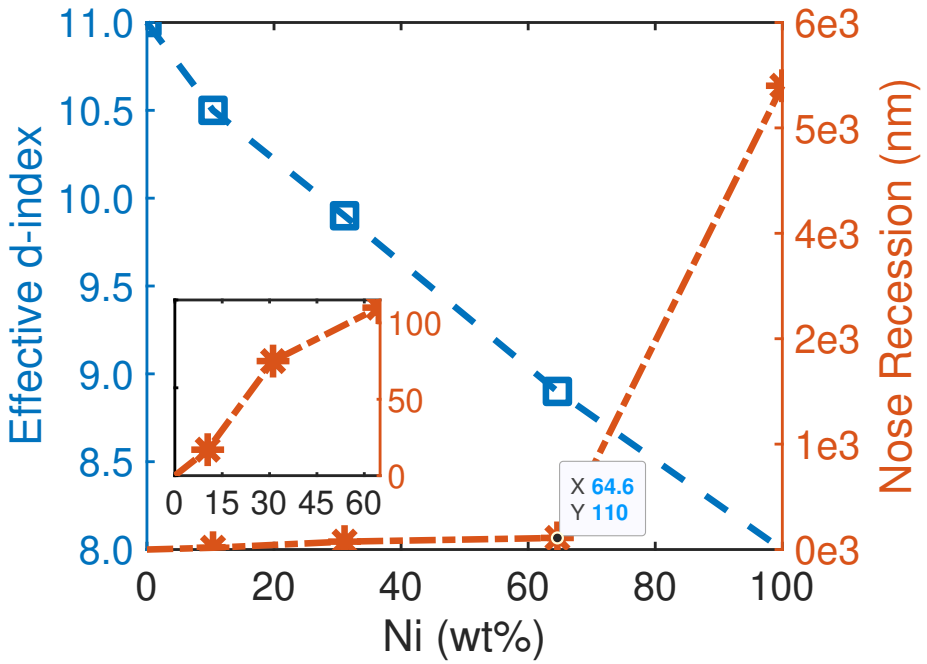

Figure 6.1: Nose recession on the final cutting pass for various Cu-Ni alloys, adapted from Browy [3]. For Cu-Ni alloys, the relationship between recession and d-index is extremely nonlinear. The inset shows the relationship between nose recession and nickel content below 64.6% Ni.

6.1 Expected relationship between wear and cutting distance

Broadly speaking, pure copper may be diamond turned with the expectation of nearly nonexistent tool wear, and pure nickel can be expected to very rapidly induce wear that deserves to be described as catastrophic. In both cases the wear is primarily

chemical in nature. Paul showed that this is due to the number of unpaired d-shell electrons available in each element, respectively. Copper has no unpaired d-shell electronsk and nickel has two.

For predicting the diamond-turnability of Cu-Ni alloys, Browy proposed a d-index model based on the idea that d-shell electrons in the nickel will combine with p-shell electrons in the copper, presenting no apparent vacancies to catalyze carbon bond breakage in the diamond lattice. Figure 6.1, adapted from Browy, compares the relationship between nickel content and effective d-index to the relationship between nickel content and nose recession for the final cutting pass [3]. Effective d-index is reasonably linear with nickel content. Nose recession is also fairly linear with nickel content for values below 64.6 %, but increases by several orders of magnitude for pure nickel.

Since the experimental parameters used in these experiments were chosen to match those used in Browy, the expected maximum nose and edge recession should be similar to what was found in that work. For Monel, this implies maximum nose recession values around 100 nm, and maximum leading edge recession values around 80 nm.

6.2 Analysis of nose and leading edge wear as a function of cutting distance

All of the analysis conducted below is performed using the data shown in Figure 3.9.

There are two hypothesis investigated here. The first is that there is a linear relationship between uncut chip thickness and the magnitude of edge recession at any point along the tool's leading edge. As uncut chip thickness increases more work must be done to cut the material, raising the local temperature of the cutting tool. Since chemical wear rates are directly related to temperature, it is expected that leading edge recession will increase with uncut chip thickness.

The second is that cutting conditions change signficantly as uncut chip thickness approaches zero, resulting in markedly different wear rates at the nose of the tool. Since the cutting edge is not perfectly sharp, once the chip is sufficiently thin the

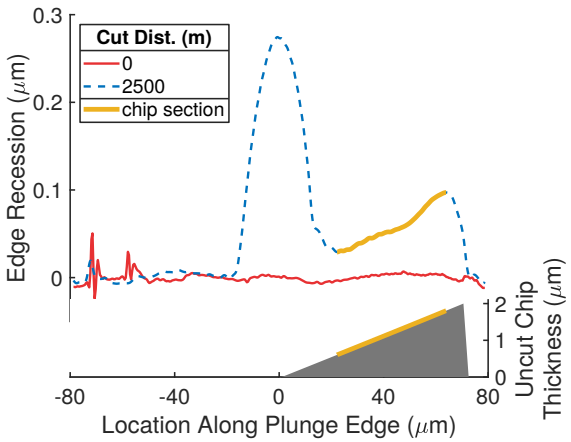

(a) The the yellow line highlights the uncut chip and leading edge sections from the final plunge plunge which are plotted against each other in the next Figure.

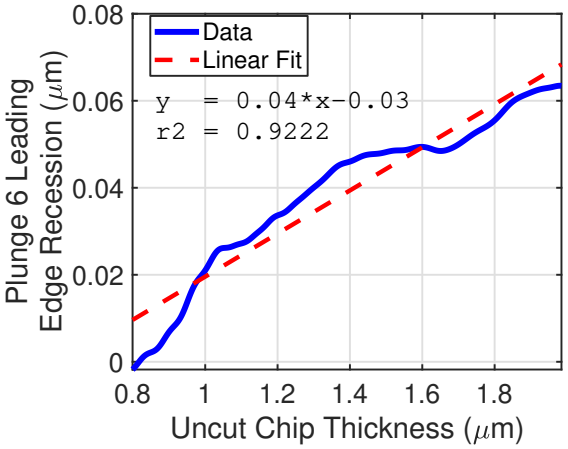

(b) Relationship between uncut chip thickness and leading edge recession.

Figure 6.2: As the uncut chip thickness increases, higher cutting forces lead to more work performed and higher local temperatures. This causes higher local wear rates as the chip thickness increases.

tool will be burnishing rather than cutting. At this point two things happen – this rubbing causes a temperature spike, and oxygen has a difficult time reaching the tool-workpiece interface.

Both of these hypotheses are only evaluated at the feed per rev and depth of cut these experiments were performed at. At higher feed rates and greater depths of cuts leading edge wear overwhelms the nose wear, and they cannot be analyzed as separate phenomena.

The relationship between leading edge wear and uncut chip thickness is analyzed by plotting uncut chip thickness against edge recession after 2500 m of cutting and taking a least-squares fit (Figure 6.2). The comparison is made from $x = 18$ to $x = 64$ µm. The local minima between nose and leading edge wear was used to choose the lower x boundary. The local maxima of the leading edge was used to choose the upper x boundary.

Nose and leading edge recession as a function of cutting distance, as well as nose

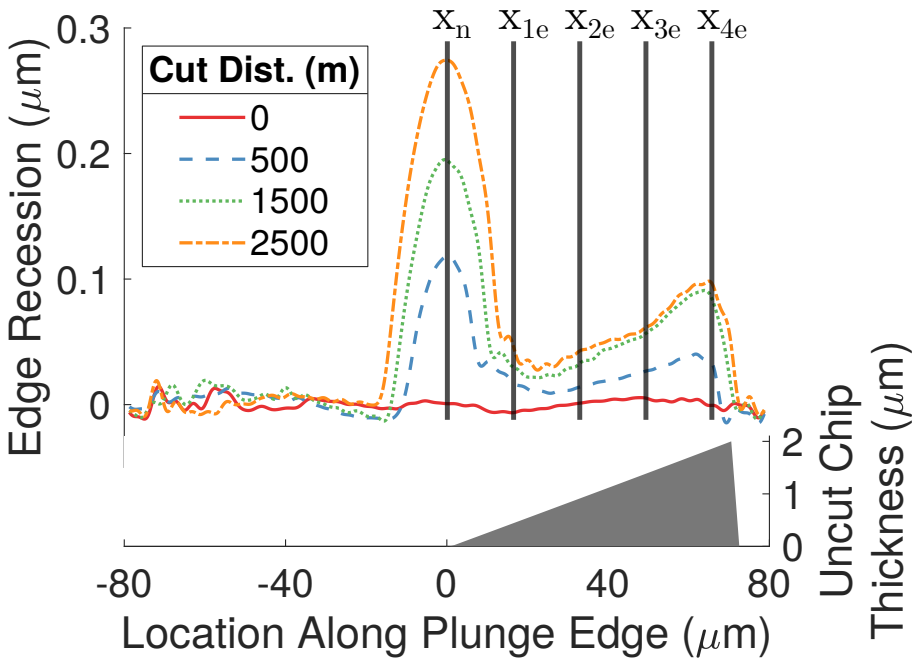

Figure 6.3: Residual from Figure 3.9, after filtering, with locations along the cutting edge where wear rates will be calculated marked.

and leading edge recession rates, were also analyzed. Nose wear was analyzed at $x = 0$ µm, leading edge wear was analyzed at equally spaced points between $x = 21$ and $x = 63$ µm (Figure 6.3). Recession rates at each x location are calculated as the using backward finite difference:

$$\delta r = \frac{r_{k-1} - r_k}{d} \tag{6.1}$$

where r_k is the recession as a function of cutting distance at a given x location, and d is the cutting distance between measurements. The recession and recession rate for leading edge wear are shown in Figure 6.4, the same is given for nose wear in Figure 6.5).

6.3 Discussion of edge recession analysis

Leading edge recession and uncut chip thickness appear to be highly correlated. The least-squares fit of the data shown in Figure 6.2 has a coefficient of determination

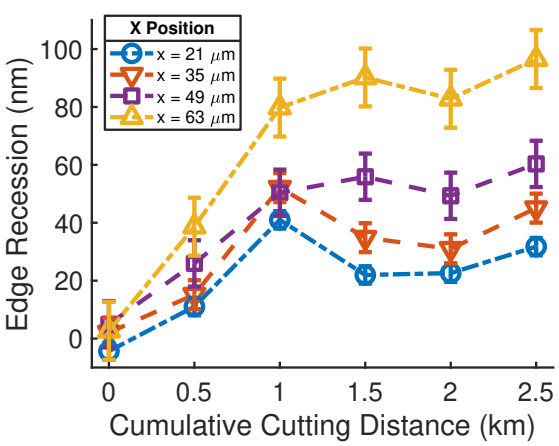

(a) Progression of edge recession along the leading edge at the marked locations. This rises rapidly for the first two facing passes, then subsequently does not change much.

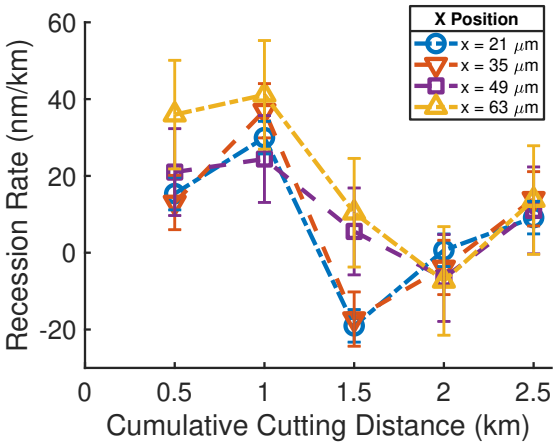

(b) Progression of edge recession rate along the leading edge at the marked locations. Wear rates are initially rapid, then decrease. Negative wear rates indicate measurement error, as they cannot represent reality.

Figure 6.4: Edge recession and edge recession rates at x_{1e} through x_{4e}.

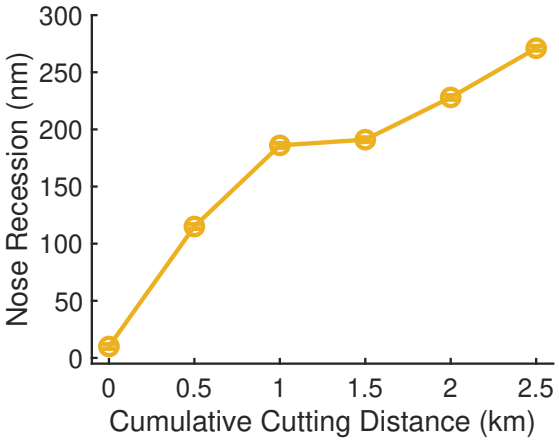

(a) Recession of cutting edge at $x = 0$ µm.

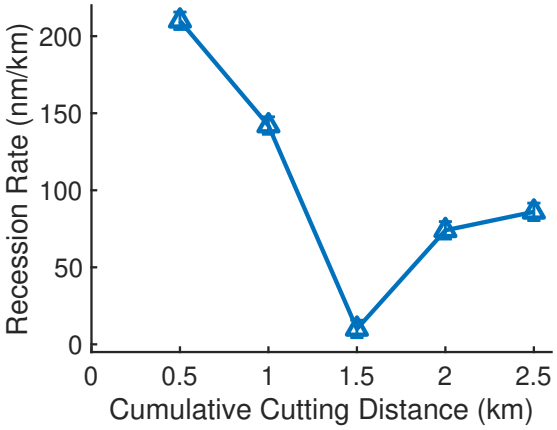

(b) Recession rate of cutting edge at $x = 0$

Figure 6.5: Nose recession and nose recession rates at x_n.

of 0.922 (or a correlation coefficient of $(0.922)^{\frac{1}{2}} = 0.96$). This implies a strong relationship between chip thickness, local cutting forces, local cutting temperatures, and ultimately, their effect on local wear rates along the leading edge of the cutting tool. This behavior can also be seen in Figure 6.4b – edge recession generally increases with uncut chip thickness.

The data in Figures 6.4 and 6.5 must be interpreted cautiously. For instance, inspecting Figure 6.4a, the unworn tool appears to have leading edge recession varying over ± 5. This is either variation in the tool shape along the leading edge, or measurement error. Additionally, for many data points the difference between $x = 21$ and $x = 35$ µm recession is 10 nm or smaller, this is smaller than the measurement uncertainty calculated in Chapter 4. Finally, for every location along the leading edge where data was collected there is a point where recession appears to *decrease* as cutting distance increases, which is not physically possible and must be measurement error. Despite this, clear trends are visible and the results represent physically plausible results. At each point along the leading edge the recession rises sharply, levels off, then begins to rise again.

Figure 6.4b suffers from all of the same problems, with the addition of noise from taking the derivative. The final problem discussed above shows up as a negative wear rate – material appears to be added to the tool. Despite this, the sharp rise, small drop, and small rise stand out even more clearly.

CHAPTER 7: DIAMOND TOOL WEAR AS A FUNCTION OF CRYSTALLOGRAPHIC ORIENTATION

7.1 Literature review for anisotropy of diamond tool wear

Two hypothesis were tested here. The first is that since the number of dangling bonds on the rake surface does not change as the tool rotates, crater wear is not related to orientation of the diamond tool. The second is that edge recession is related to crystallographic orientation by the model described in Section 2.3. If the $< 100 >$ direction in Figure 7.1 is normal the workpiece, wear will be minimized. As the angle between $< 100 >$ and the normal vector increases, chemical wear will increase, with a maximum at 55 degrees, then decrease slightly.

7.2 Crater wear and crystal orientation

The crater wear hypothesis was tested by performing a series of experiments as described in Chapter 3, but with the additional step of taking interferograms of the tool's rake face using a 50x objective after the tool has been used for an experiment. This was done at tool rotations of 0, 4, 7.5, 15, and 22.5 degrees. As discussed in Section 4.1 the effective resolution is no greater than 0.498 µm. This is adequate for the purposes of this experiment.

The interferograms were loaded into MATLAB and a best fit plane was subtracted to remove any tilt and DC offset from the measurement. The measurement is then cropped to the size of the crater. A typical measurement result, before and after cropping, is shown in Figure 7.3. All NaN values are then replaced with zeroes and the surface is filtered with a Gaussian filter using a cutoff frequency of 4 µm. The results of this process for all six measurements are shown in Figure 7.4. It is

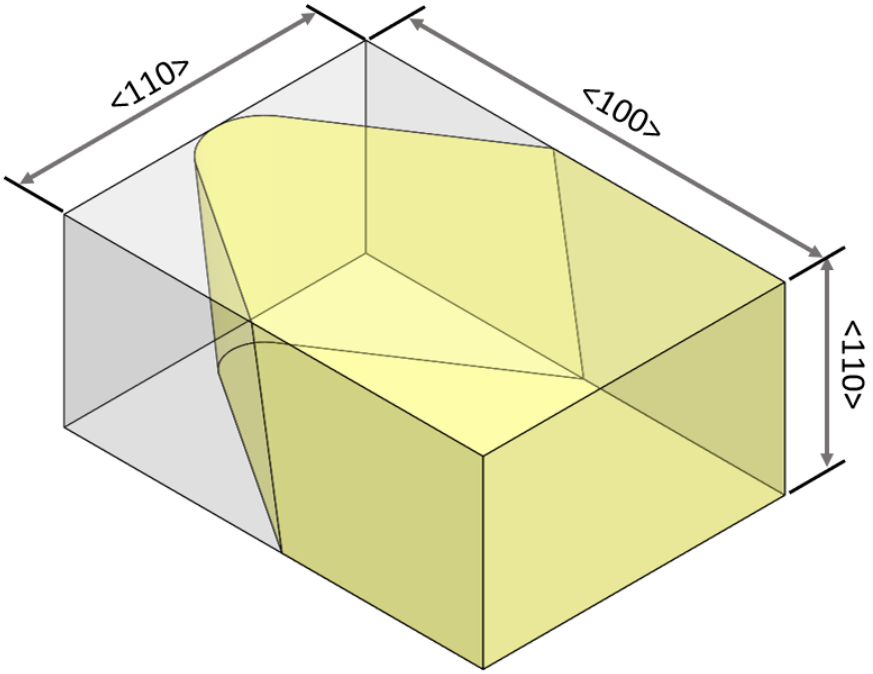

Figure 7.1: Crystal lattice geometry for the diamond tools used in these experiments.

Figure 7.2: Custom tools with the diamond blank brazes on at an angle.

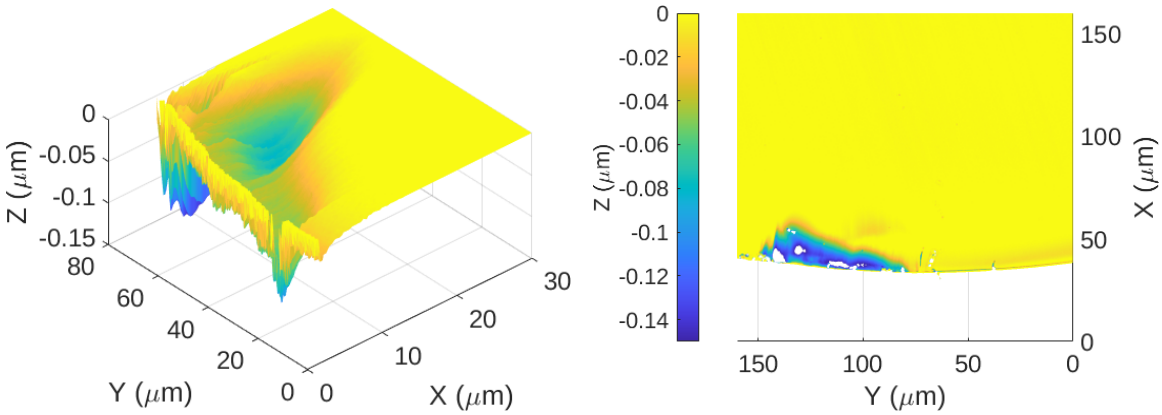

(a) Interferogram of crater on rake face, after cropping.

(b) Interferogram of crater wear on rake face, before cropping.

Figure 7.3: Typical measurement of the rake face. This measurement is of a tool rotated to 15 degrees.

noteworthy that the crater never extends along the x axis more than 35 µm from the tool edge, and is generally the length of the uncut chip along the y axis.

All six craters have similar roughly similar length and width dimensions, but the 0 degree and one of the 15 degree measurements both feature substantially deeper craters then the other measurements. It is likely this is due to chips not being effectively cleared by the coolant during the machining operation.

The crater volume for each measurement is determined by numerically integrating over the cropped phasemap using the MATLAB `cumtrapz` function, the results are presented in Figure 7.5. As expected, there appears to be no relationship between tool rotation and the degree of crater wear. When the cutting interface is kept clear of chips, the crater size is consistent to single-digit nanometers.

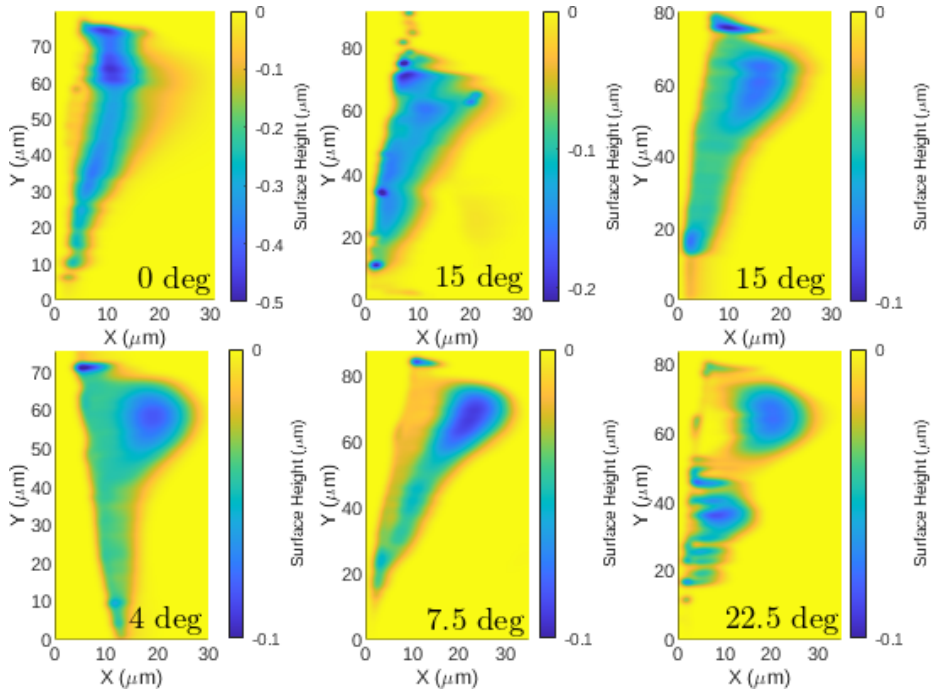

Figure 7.4: Cropped and filtered interferograms of the rake face crater after six experiments at a variety of angles. Crater depth for the first two measurements is significantly greater than for the final four, so the first two are presented on their own z scales. All others are on a matching z scale.

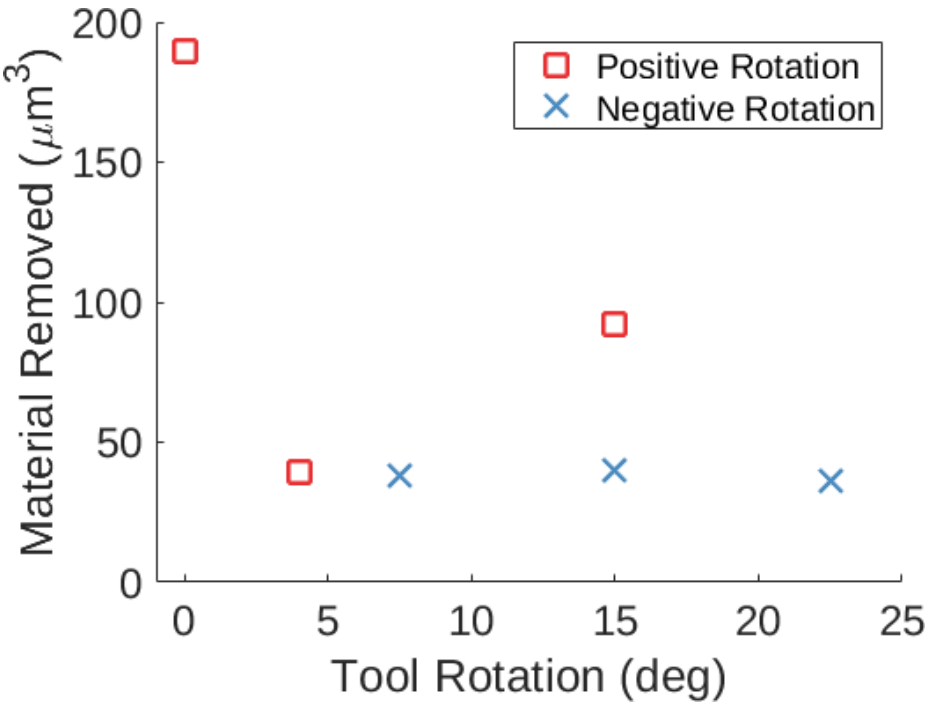

Figure 7.5: Volume of material removed from the rake face over the course of one experiment, as a function of angle.

7.3 Edge recession and crystal orientation

The hypothesis relating wear, crystallographic orientation, and the volumetric distance between atoms in the diamond lattice at a given orientation was tested using two methods. The first method was to simply rotate the tool to some angle theta with respect to the workpiece (Figure 3.1),. The second method was to have custom tools manufactured with the diamond mounted at an angle (Figure 7.2), so that the tool shank could still be normal to the workpiece. For both methods the experiments were conducted as described in Section 3.

The magnitude of wear with the custom tools was substantially larger than is typical with standard tools, making direct inter-comparison of results between the two experiments impossible. They are analyzed separately here.

The hypothesis predicts wear will increase quadratically as the tool is rotated away from normal to the workpiece, up to 55 degrees, then wear will decrease upon additional rotation.

Standard tools can only be rotated approximately 22 degrees from normal in the experimental setup, at higher angles chatter causes rapid wear of the tool. A total of 33 experiments were conducted over the course of three years using standard tools at a variety of angles. A selection of results at 0, 4, 15, and 22.5 degrees are shown in Figure 7.6, showing a clear increase in maximum nose and leading edge recession as the tool is rotated. The increase from 0 deg to -22.5 deg is so large that the latter needs to be presented on a different ordinate scale. The 'bump' near the edge of the -22.5 measurement should also be noted–this is typical of experiments where the tool was only relapped, and not reconed, between experiments, and seems to be related to unworn edge quality. After generating these data sets the maximum nose and maximum leading edge recession are found for all experiments using the final edge recession profile. For the standard tools, maximum recession nose and leading edge recession, respectively, are defined as:

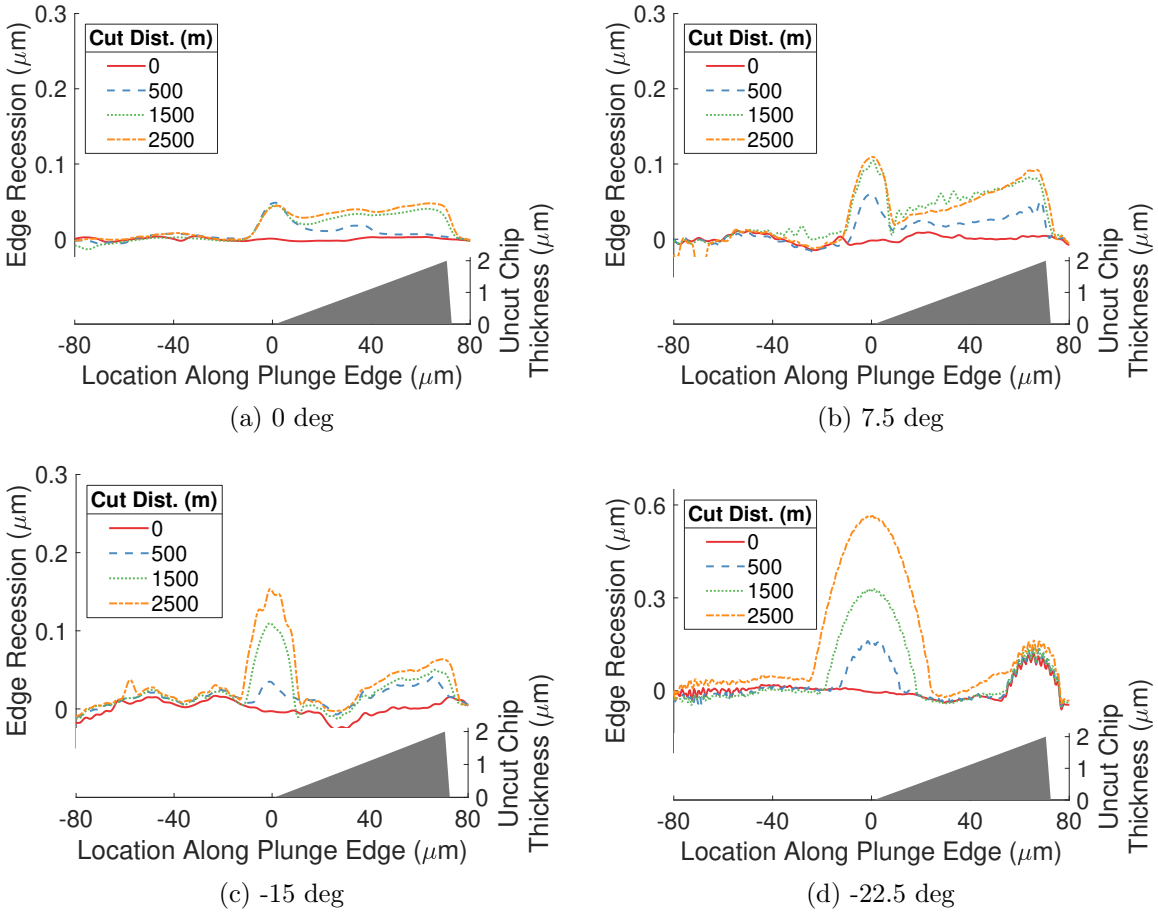

(a) 0 deg

(b) 7.5 deg

(c) -15 deg

(d) -22.5 deg

Figure 7.6: Selected recession plots at 0, 7.5, -15, and -22.5 degrees. The nose recession increases in a gradual manner, then jumps at 22.5 degrees - the y axis must be changed to accomodate the higher recession.

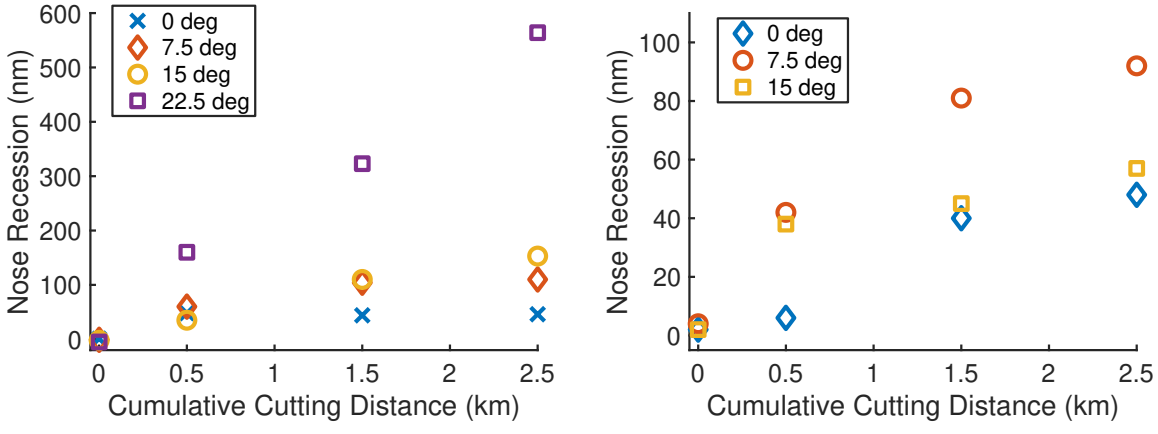

(a) Nose recession at $x = 0$ µm

(b) Leading edge recession at $x = 63$ µm

Figure 7.7: Nose and leading edge recession for the residuals in Figure 7.6.

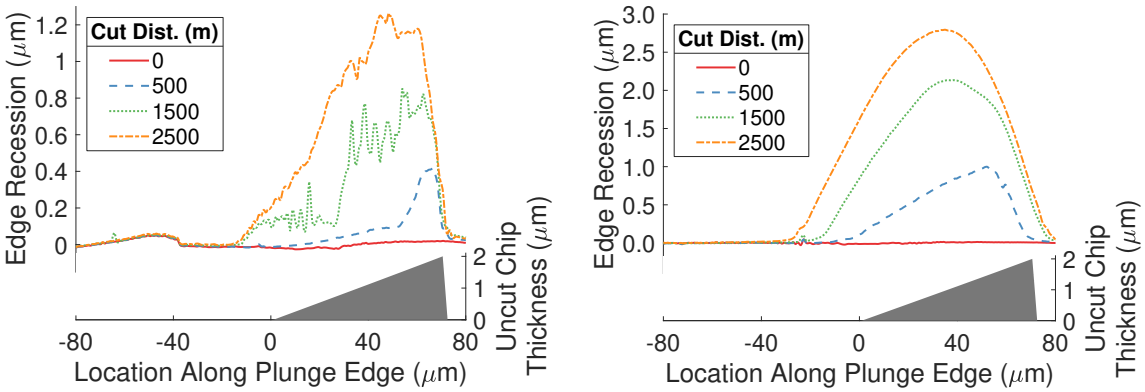

(a) Outlier at +15 degree rotation.

(b) Outlier at +22.5 degree rotation.

Figure 7.8: Outliers at higher angles of rotation. Both have edge recession to such a large degree that nose wear cannot be differentiated from leading edge wear.

```
1  max_nose = z(x == 0);
2  max_edge = z(x == 63);
```

These are the same parameters used in the preceding section. Both methods were tested–the difference between these two approaches is negligible. When this process has been performed on all of the available data, the result is three arrays: one of maximum edge recessions, one of maximum nose recessions, and one for the corresponding rotations. Between three and seven experiments were performed at each angle. Figure 7.9a shows the results of this process. There are notable outliers present, specifically at 15 degrees and 22.5 degrees. The residual plots for these outliers are shown in Figure 7.8.

After outliers have been identified and, if possible, discarded, the remaining data at each angle is averaged and presented in Figure 7.10.

This plot can be compared to the theory presented in Figure 2.2 by first inverting the theoretical plot so that bond magnitude increases with the inverse of bond density (which is bond distance), and then normalizing both plots so that they are unitless and can be inter-compared. The model is shown before and after normalization in

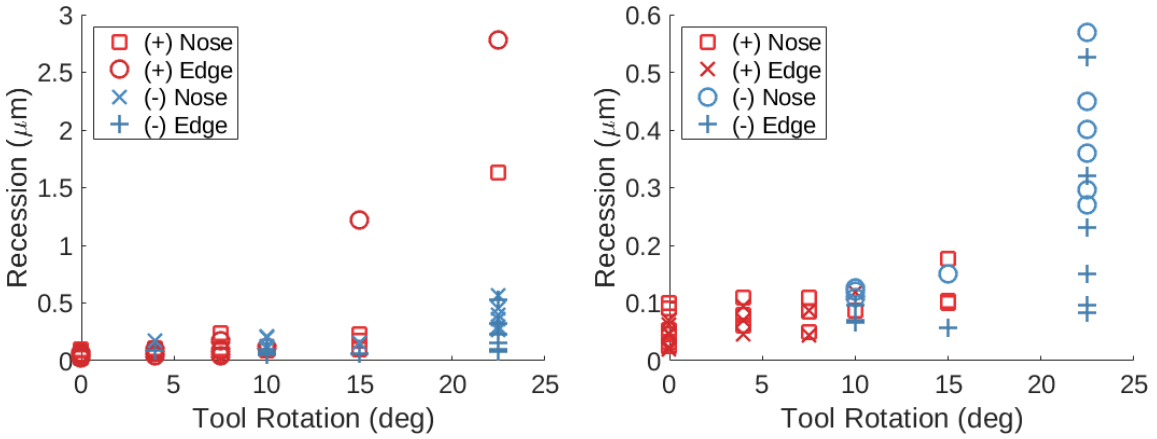

(a) All recession vs angle data, including the outliers discussed above.

(b) Recession vs angle data after outlier removal.

Figure 7.9: Angle data from all experiments, before and after outliers have been identified and removed from the data set.

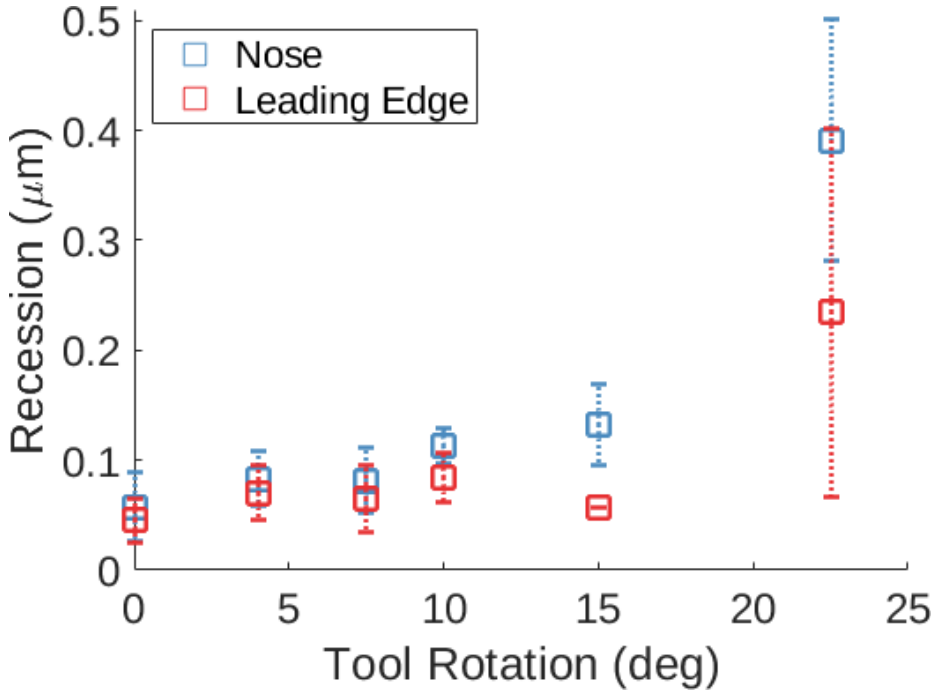

Figure 7.10: Maximum nose and leading edge recession, averaged at each angle of rotation.

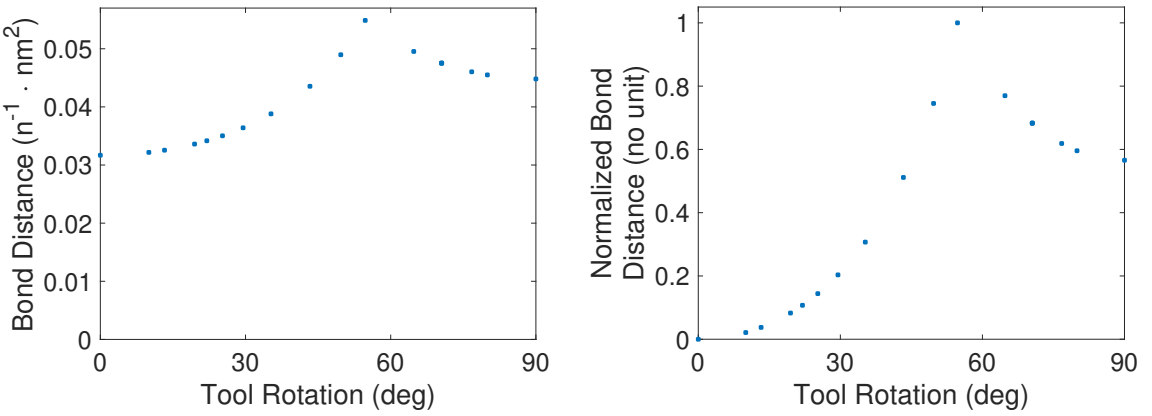

(a) Volumetric distance between carbon atoms as a function of crystal orientation.

(b) Volumetric distance normalized onto a scale from zero to one.

Figure 7.11: Bond distance as a function of crystallographic orientation before and after normalization.

Figure 7.11. The model is a discrete set of points because it is developed from a set of Miller indices. Both normalizations are done using the equation

$$y = \frac{(x - min(x)) * (b - a)}{max(x) - min(x)} + a \tag{7.1}$$

where b is the maximum scaled value, and a is the minimum scaled value. Bond distance is minmax normalized onto a scale from $a = 0$ to $b = 1$. The average nose and average edge recession are both minmax normalized onto a scale from $a = 0$ to the value of the theoretical model at 22.5 degrees ($b = 0.38$ for nose wear, and $b = 0.23$ for leading edge wear, from Figure 7.10).

These results show good agreement between theory and measurements, but only up to 22.5 degrees. The custom tools manufactured for these experiments have diamonds rotated to 10, 25, -25, 55, and 90 degrees. It is expected that wear will increase up to 55 degrees, be symmetrical across 25 degrees, and decrease at 90 degrees. These experiments were performed twice for a total of ten data sets at each angle. The general hypothesis is supported by the results: wear increased rapidly from 10 degrees to 55 degrees. However, wear at 90 degrees is also very rapid, and wear rates across

positive and negative 25 degrees are not symmetric.

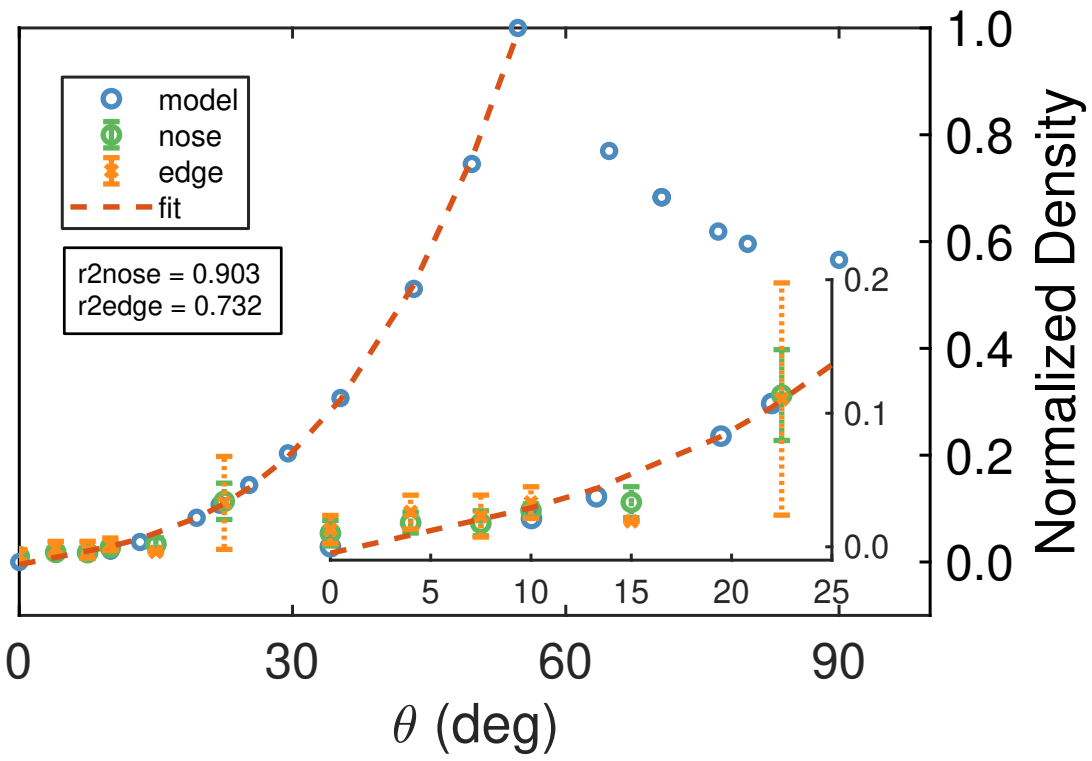

Figure 7.12: Comparison of maximum edge recession to the predictive theory for angles of tool rotation between 0 and 25 degrees. The model is Equation 2.3, the dashed line is a cubic fit to that model from 0 to 55 degrees.

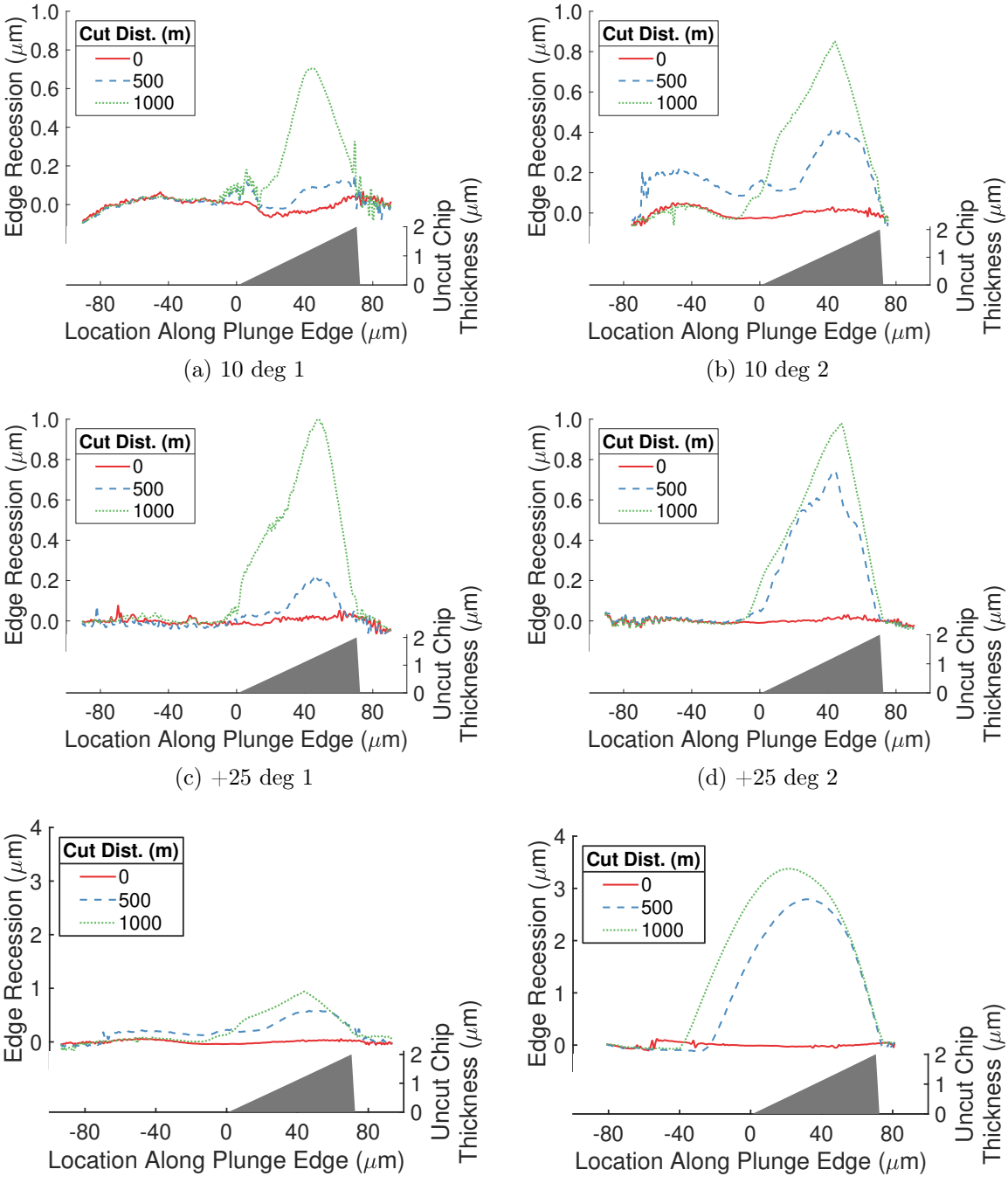

(a) 10 deg 1

(b) 10 deg 2

(c) +25 deg 1

(d) +25 deg 2

(e) -25 deg 1

(f) -25 deg 2

Figure 7.13: Edge recession residual plots from experiments conducted using custom tools at 10 degrees and +/- 25 degrees. The final two plots are on a larger vertical scale.

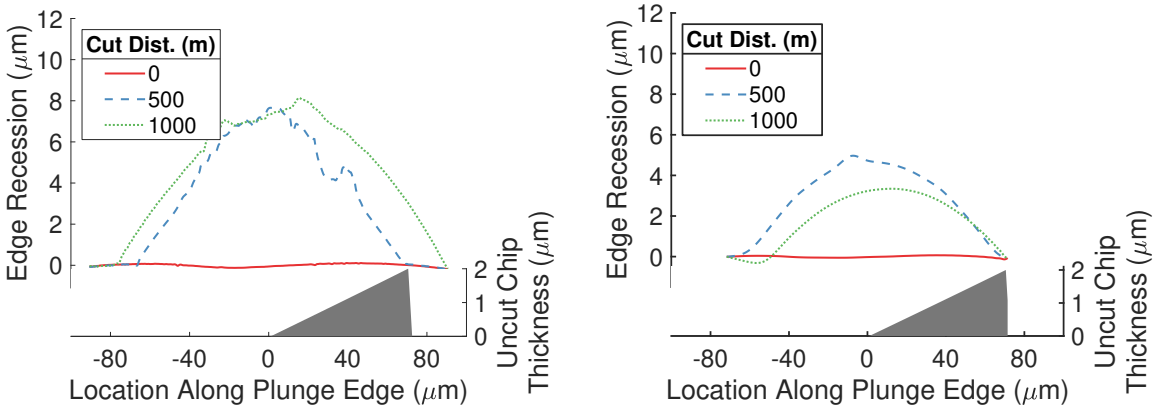

(a) 55 deg 1

(b) 55 deg 2

(c) 90 deg 1

(d) 90 deg 2

Figure 7.14: Edge recession residual plots from experiments conducted using custom tools at 55 degrees and 90 degrees.

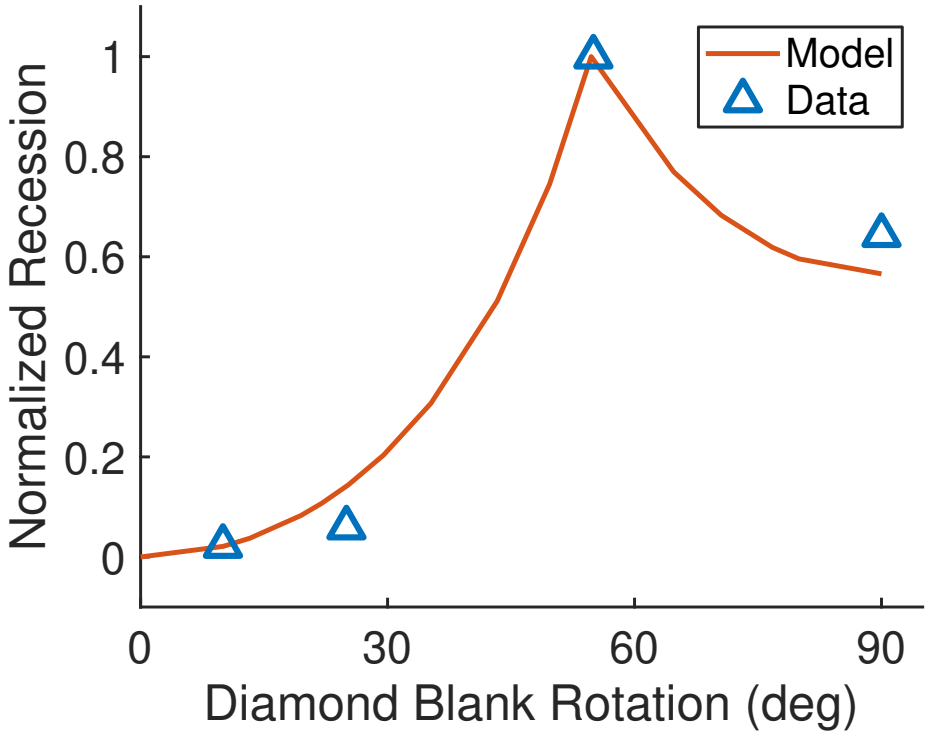

Figure 7.15: The analysis developed for standard tools (shown in Figure 7.12), applied to the custom tools shown above. Negative angles of rotation are omitted.

7.4 Discussion of angular orientation experiment results

Two hypothesis were tested in this chapter. The first is that crater wear, defined as the volumetric size of the crater, will not vary as the tool is rotated. The experimental data collected supports this hypothesis. Further work using lithographically applied thermocouples to relate these craters to temperature distributions would be interesting.

The second is that edge recession will vary with tool rotation, with maximum recession rising as bond density decreases. This hypothesis is also supported by both the model and experimental results. Experiments using standard tools match the model out to 22 degrees, but further rotation of the tools turns the tool shank into a tuning fork, causing chatter and high wear rates. Rotation of standard tools to higher angles while still keeping the structural loop sufficiently stiff could probably be done on a machine with a b-axis.

Custom tools were manufactured to test the bond density hypothesis at higher angles of rotation. Two sets of experiments were performed with these tools. The results were consistent between experiments, and they support the hypothesis. Peak recession increased up to 55 degrees, then decreased at 90 degrees, as predicted. However, these experiments also raised additional questions. These tools experienced substantially higher wear rates than standard tools manufactured by the same vendor, regardless of the angle of rotation. There could be multiple causes for this. The most likely is that creating a cutting edge even slightly off the [100] plane is difficult. This is supported by the large deviations in the unworn plunge that can be seen in all of the custom tool residuals. At 90 degrees of rotation the edge is being created at the intersection of two [111] planes. This is the softest, least resistant edge with respect to mechanical abrasion on the entire diamond log.

The custom tool experiment could be repeated, using an indium block mounted to a dynamometer to record the cutting tool edge sharpness after each pass. This would

allow relationships between edge sharpness and rotation of the diamond blank to be explored. Understanding the cause of the higher wear in the custom tool experiments would allow stronger conclusions to be drawn.

CHAPTER 8: DIAMOND TOOL WEAR AS A FUNCTION OF OXYGEN PARTIAL PRESSURE

This chapter reviews the model of chemical tool wear in the context of oxygen partial pressure, describes an experiment to investigate that relationship, and discusses the results of that experiment. A model based on Langmuir surface occupancy is proposed to explain the experimental results.

8.1 Historical research on wear and gaseous environment

Investigation of the relationship between the atmospheric environment and tool wear has historically provided results that are either difficult to interpret, or directly in conflict.

In 1979 Thornton and Wilks discovered that machining mild steel with a diamond tool in weak vacuum (100 mTorr) reduced wear by fifty percent–but only at low cutting speeds [38]. This work was not performed on an ultraprecision lathe, and the cross feed and depth of cut were high for diamond turning work. They expanded this work in 1980, including cutting in an inert gas (argon) atmosphere. The results of this follow-up work showed considerable variance, possibly from variation in composition between diamond tools used in the experiments [37]. In 1984 Hitchiner and Wilks followed up on these experiments, repeating the vacuum experiments and also testing the effect of both methane and hydrogen atmospheres on wear [68].

Taken as a whole, these experiments provide results that show that the rate of tool wear may depend on the gaseous environment. Turning in vacuum may decrease wear rates, and the the replacement of typical atmosphere with methane or hydrogen drastically increases wear. The former is evidence for the influence of oxygen on wear.

The specific question this work attempts to answer is: does varying oxygen partial pressure vary the wear rate? The previously mentioned work implies an effect; removing atmsophere (and oxygen) from the environment lowers wear rates. This hypothesis is supported by Shimada's finding that reducing oxygen partial pressure causes crater wear to decrease when diamond-turning OFHC copper [29]. When performing similar experiments on steel, Brinksmeier found no change in wear rates [34]. What is understood about the chemical nature of diamond tool wear implies that varying of oxygen partial pressure should change the rate of wear.

There are two primary pathways for chemical wear– an oxygen-dependent (aerobic) pathway and an oxygen-independent (anaerobic) pathway (Equation 2.2). Turning in an environment with reduced oxygen partial-pressure should allow the relative importance of each pathway to be investigated. If the aerobic reaction pathway is important wear should decrease substantially as the oxygen partial pressure is reduced. If it is not, then wear rates should only change a small amount, or remain the same.

8.2 Experimental setup, data collection and processing

This hypothesis was tested by turning in an enclosure designed to control the oxygen partial pressure by pumping helium into the chamber to purge the environment (Figures 8.2, 8.3). The gas is injected into the system through a collar around the spindle, a diffuser in the aluminum plate mounted to the spindle, and the coolant supply. The oxygen partial pressure is controlled by manually adjusting the flow rate of helium at the spindle collar, diffuser, and coolant nozzle.

The enclosure is consists of an aluminum spindle plate and base plate, aluminum tubing used to frame the enclosure, and four lexan plates. The base plate is lightweighted to minimize stress on the moving stage. The interface between the three vertical Lexan sheets and the frame is sealed with epoxy. The top Lexan sheet is removable to allow access to the workspace and is sealed with rubber weather stripping. A sliding seal

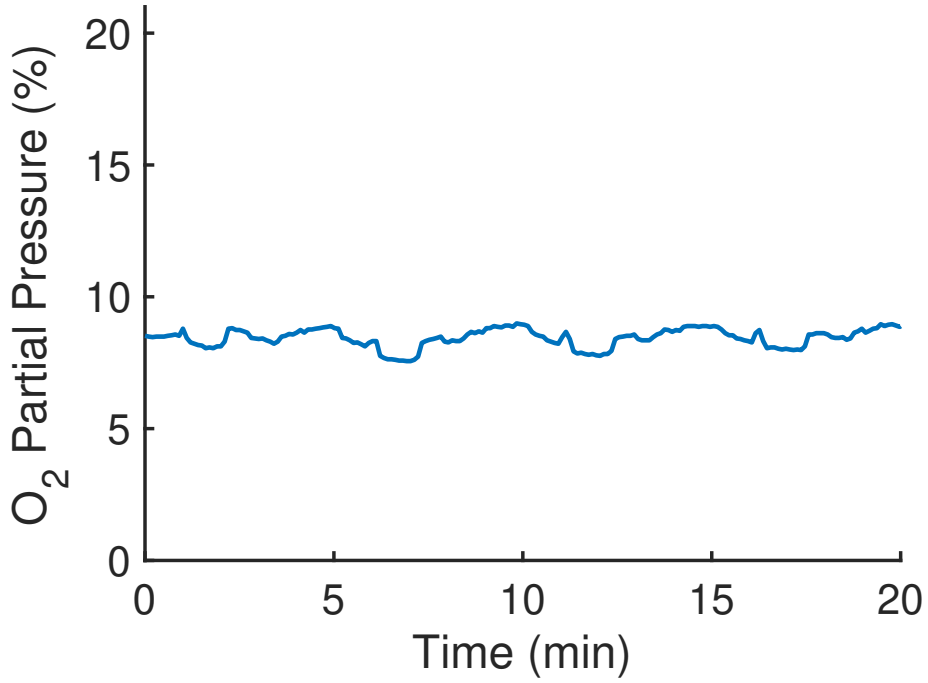

Figure 8.1: Varation of oxygen partial pressure with time when controlling over the course of an experiment.

is created between the frame and base plate using weather stripping.

The spindle collar is designed with a 100 µm gap and internal geometry which preferentially forces helium into the enclosure, forming an air gasket (Figure 8.4). Partial pressure is controlled by manually controlling the helium flow rate. This approach allows partial pressure to be controlled with a 0.2% range during an experiment(Figure 8.1). The results of seven experiments at a variety of partial pressures are presented here. Temperature in the enclosure is monitored at two locations, near the cutting interface and far from the cutting interface. Oxygen partial pressure is recorded using a PulseOx PRO OX-100B.

8.3 Collection and analysis of data

Data was collected by performing the same experiment described in Section X, but using the enclosure to modify the oxygen partial pressure during each experiment. All of the data displayed below was collected with the tool rotates to negative ten

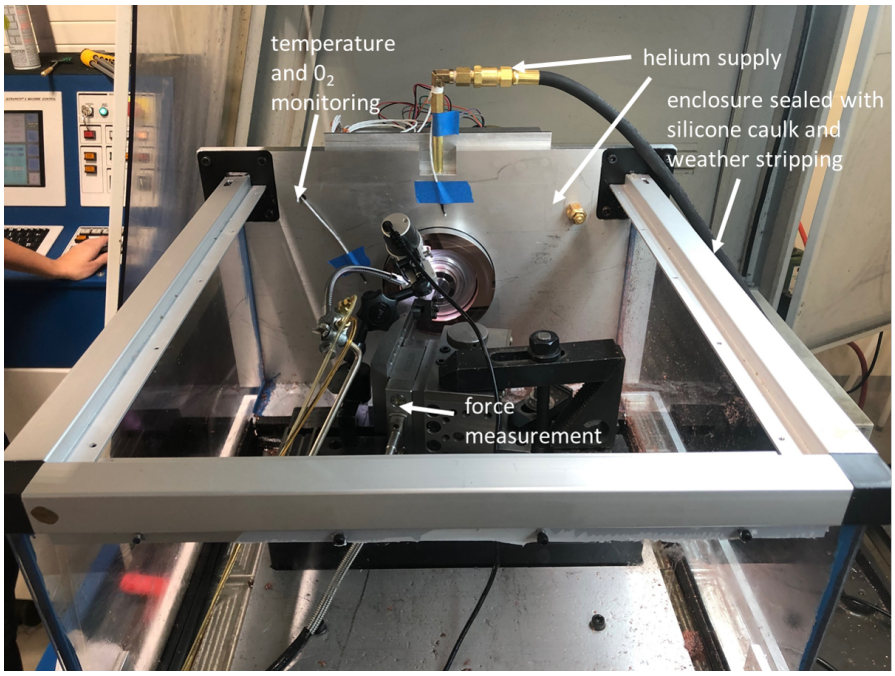

Figure 8.2: Enclosure used to control oxygen partial pressure while conducting wear experiments. A Lexan lid with rubber gaskets sits on top the aluminum rails during the experiment.

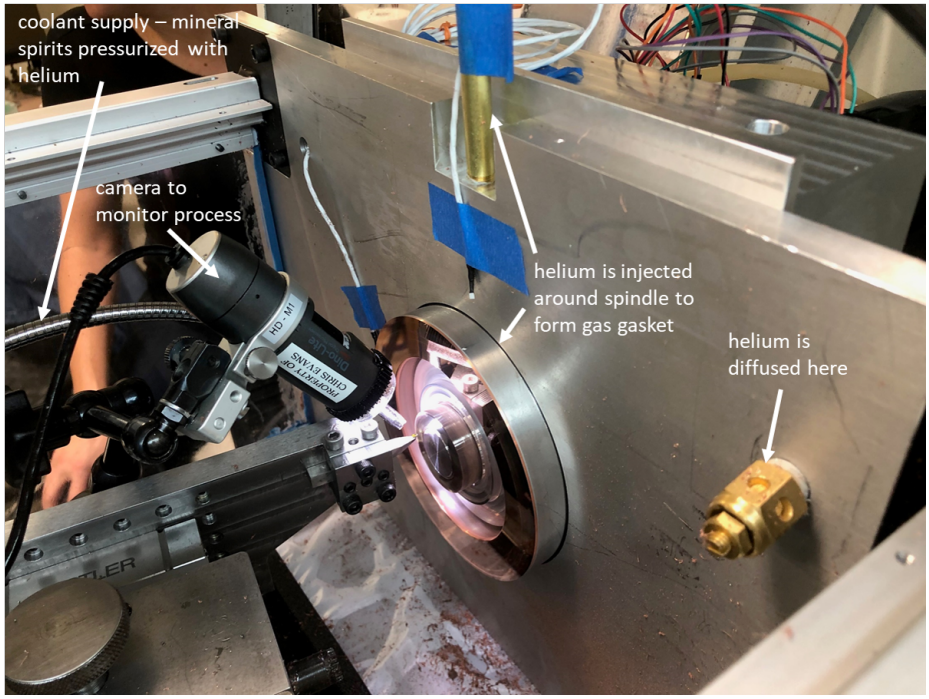

Figure 8.3: Detail view of the enclosure, showing the cutting setup and helium injection locations.

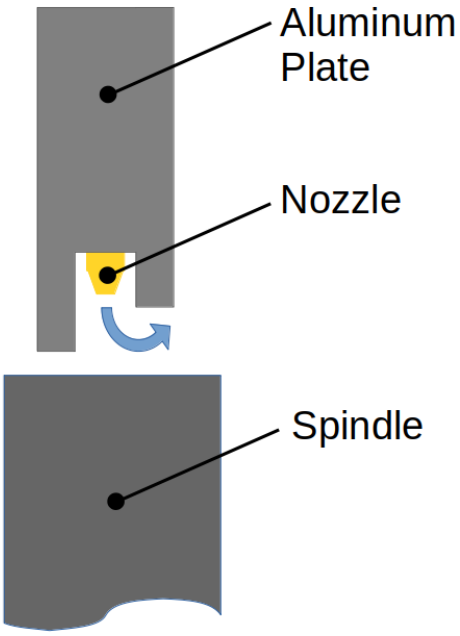

Figure 8.4: Section view of gap between spindle and aluminum plate. Pressurizes gas flows preferentially towards the enclosure interior and forms a gasket.

degrees. This experiment was performed over twelve times, but only eight experiments produced results without excessive wear rates. This is most likely caused by the weight of the enclosure causing problems with the machine controller. If repeating the experiment, it would make sense to lightweight the spindle plate and use smaller, lighter aluminum framing. Friction from the sliding interface at the enclosure base could have also contributed to this problem.

The residuals from these experiments are presented in their entirety to inspect for trends. The figures are grouped by oxygen content, Figure 8.5 presents residuals from low-oxygen (relatively anaerobic) experiments, and Figure 8.6 shows residuals from higher oxygen content experiments. The magnitude of recession at both the nose and along the leading edge appears to not change, regardless of the atmosperic oxygen content. The morphology also does not change–for instance, there are no examples where leading edge wear begins to dominate, or pekelharing grooves increase in magnitude. For these seven experiments, maximum nose and maximum leading

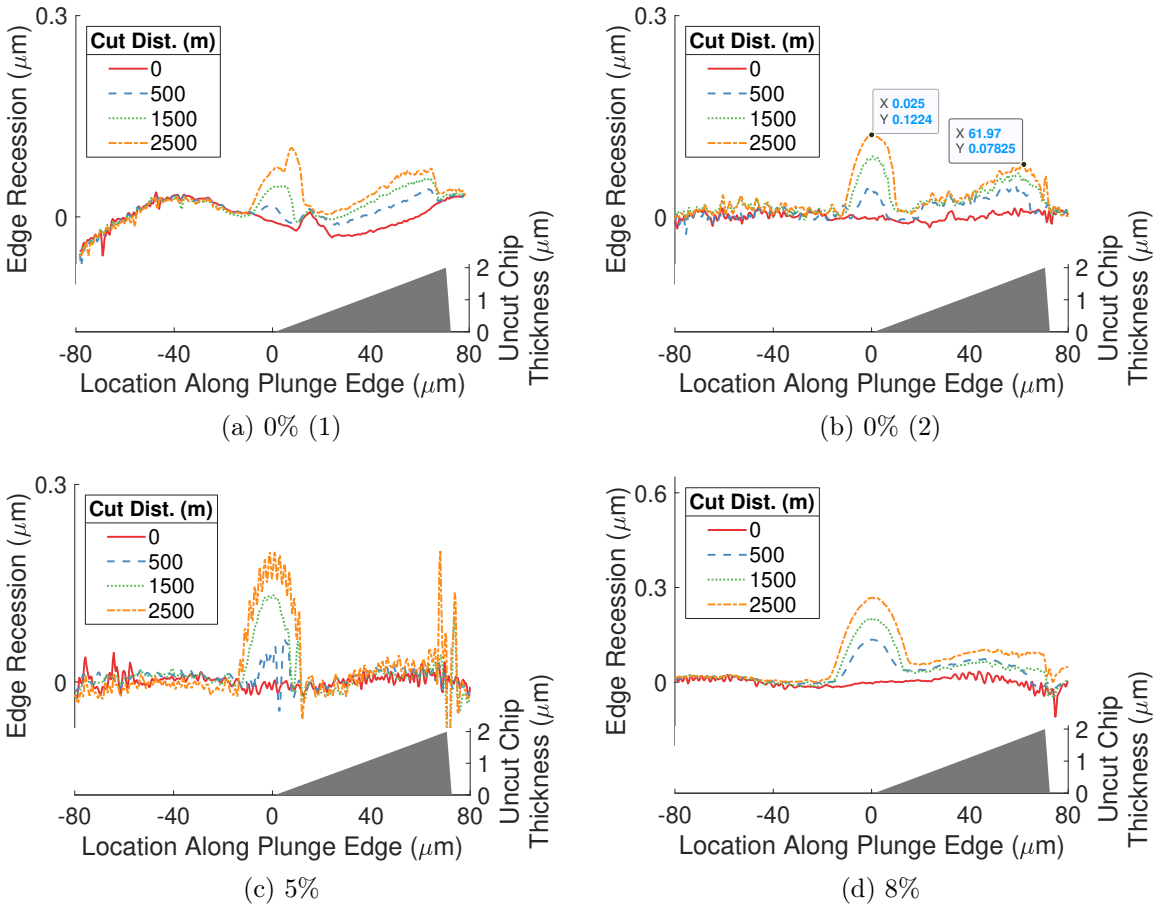

(a) 0% (1)

(b) 0% (2)

(c) 5%

(d) 8%

Figure 8.5: Residuals at lower levels of oxygen partial pressure.

edge wear were plotted against oxygen partial pressure (Figure 8.7).

8.4 Discussion of wear rates and oxygen partial pressure

No effect on wear rate was observed when varying the oxygen partial pressure. This is unintuitive. Below is a discussion of possible factors influencing the result of the experiment. One variable is cleanliness of the tool surface. It is possible that an extremely thin layer of contaminant could provide enough oxygen to the surface to influence the experiment. Another is humidity of the local atmosphere. No sensor was used to record humidity, so atmospheric vapor levels during the experiments are not known. However, water molecules are relatively heavy and difficult to crack. The final consideration is temperature changes due to the Joule-Thomson effect. Helium

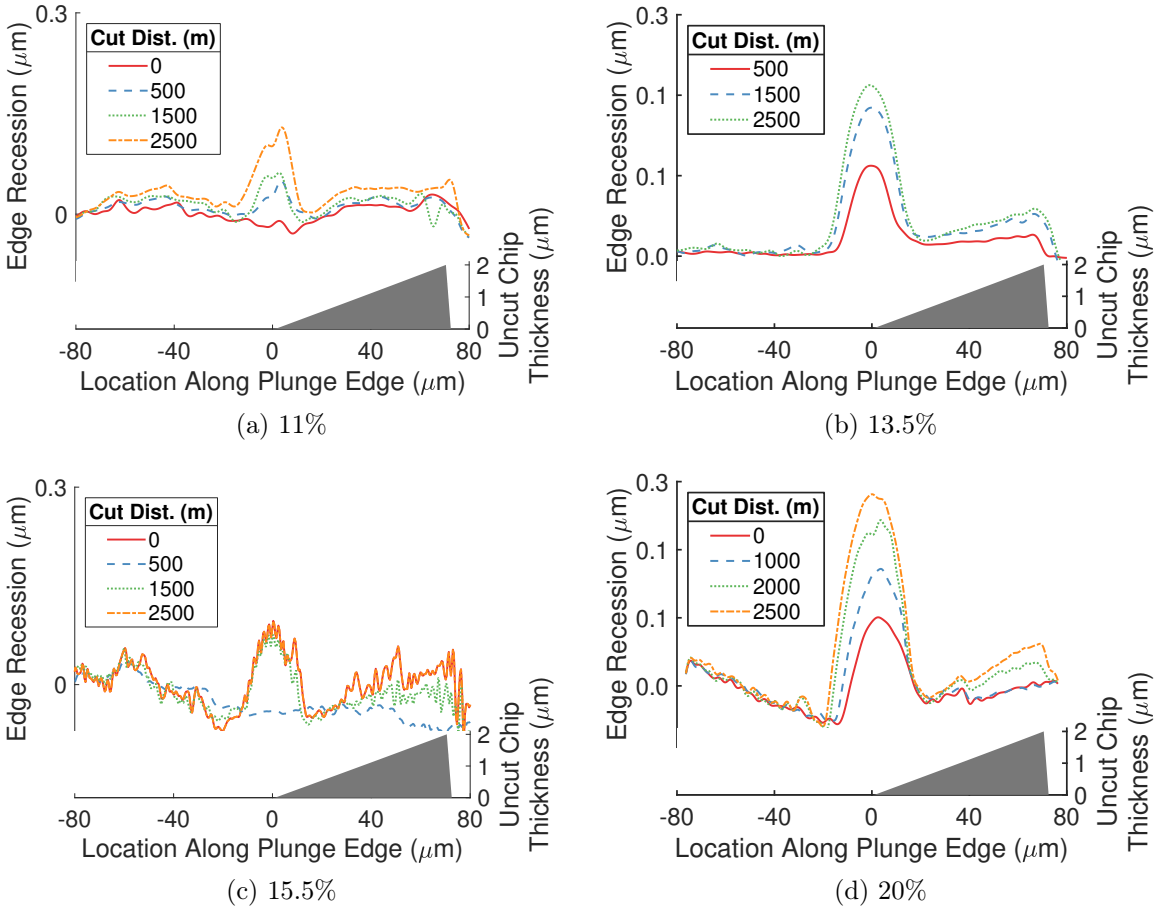

Figure 8.6: Residuals at higher levels of oxygen partial pressure.

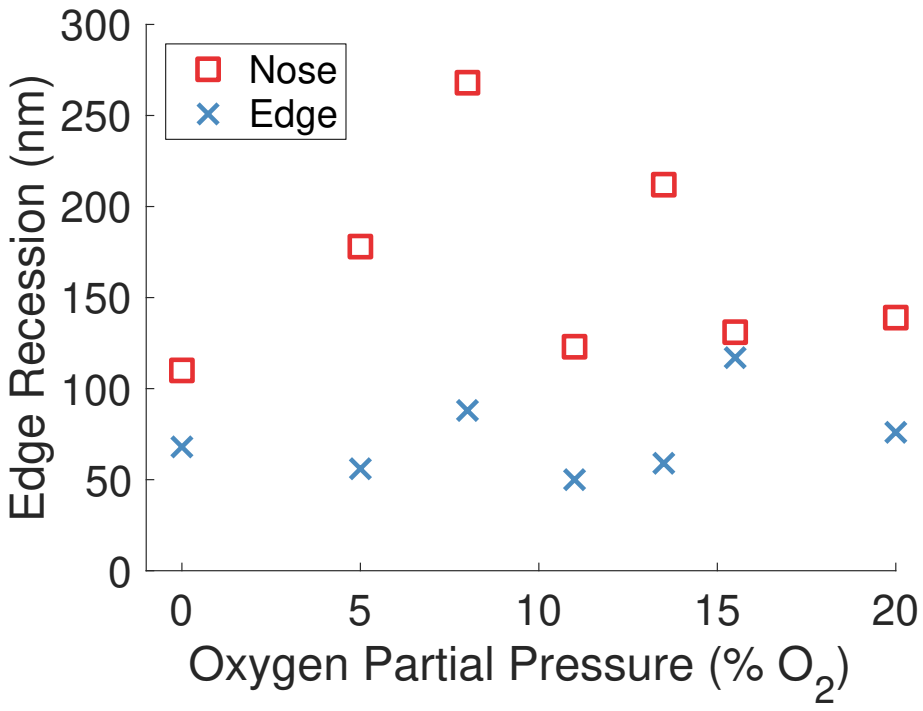

Figure 8.7: Wear rate with changing oxygen partial pressure.

has a negative Joule-Thomson coefficient, meaning that the enclosure temperature will rise as helium expands through the nozzles. It is possible that elevated environmental temperatures could lead to higher temperatures at the cutting interface, and subsequently to higher wear rates.

In addition to all of this, a model of the surface chemistry is needed to correctly model the role of oxygen in the chemical reaction occuring between the tool and workpiece. The Langmuir surface model is used as the foundation for a new model.

8.4.1 Elevated enclosure temperatures and Joule-Thomson cooling

Figure 8.8 shows temperatures near the cutting interface for a subset of the experiments discussed here (data from all experiments was not available). There is an obvious trend–the experiment performed at lower oxygen partial pressures was at a substantially lower temperature. The opposite should be happening, since increased helium flow should result in warming of the enclosure.

This disparity is likely due to temperature fluctuations in the room itself. Figure 8.9

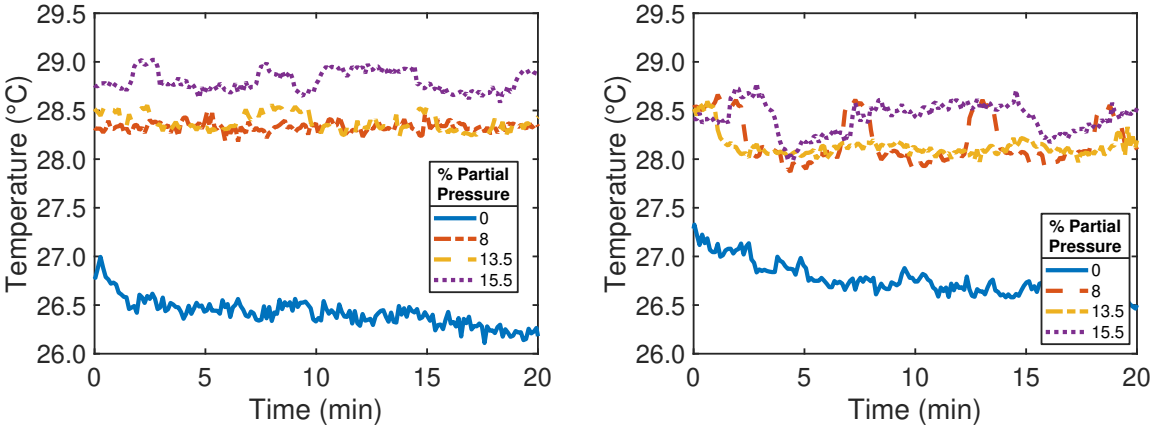

(a) Temperature near cutting interface.

(b) Temperature away from cutting interface.

Figure 8.8: Temperature close to and away from the tool tip for four experiments.

shows the typical range of temperatures in the room where the diamond turning machine used for these experiments is located. The temperature over long timescales varies by 1.5 degrees in a sawtooth pattern. The difference in measured experimental similar. If one set of experiments was carried out near a high room temperature, and another near a low room temperature, this could account for the difference.

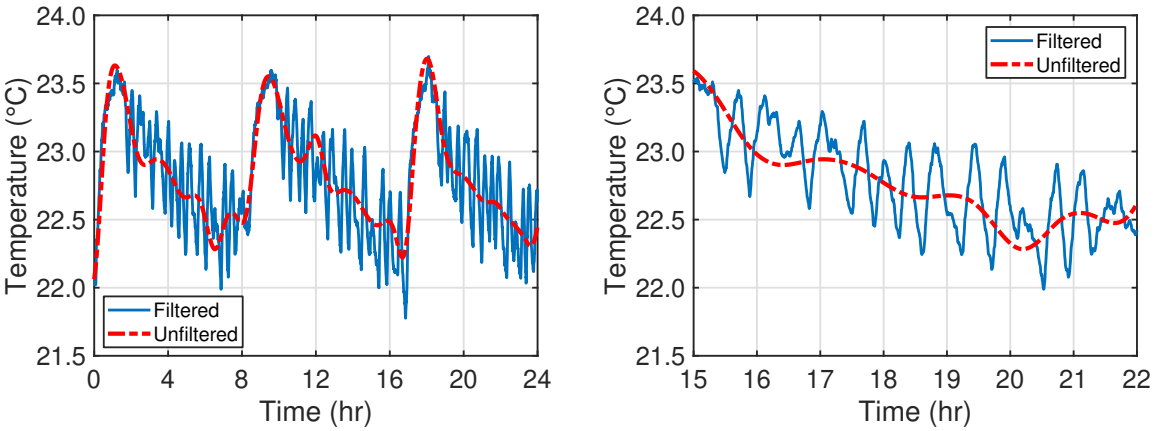

(a) Room temperature measured over a twenty four hour period.

(b) Room temperature of one cycle.

Figure 8.9: Temperature in the room where the diamond turning machine is located, over one twenty four hour period. The temperature varies cyclically by 1.5 degrees on a seven hour cycle. The right-hand plot shows a shorter period. A thirty-minute cycle over a half degree range is seen.

8.4.2 Langmuir surfaces and wear rates

Irving Langmuir founded the study of surface chemistry through the introduction of a simple model. The model describes surfaces as consisting of sites that are either empty, or occupied by a reactant. Furthermore, the chemical reaction rate is proportional to the number of occupied sites.

This model, developed below, makes the following assumptions.

1. The surface is a perfectly flat plane.
2. Each site can hold only one molecule.
3. The gas adsorbs cannot move between sites after adsorption.
4. Each site on the surface is energetically equivalent.
5. There are no interactions between adsorbed molecules at adjacent sites.

If n is the total number of available surface locations and X is the fraction which are occupied, then the total number of occupied sites is $n \cdot X$ and the total number of unoccupied sites is $n \cdot (1-X)$. If the system is in equilibrium then the forward reaction and backward reaction rates are equal. The forward rate of reactant sticking to the surface, r_f, is proportional to the number of unoccupied sites and to the concentration of reactant in the gas interacting with the surface, $[O_2]$. The backward rate, r_b, is proportional to the number of occupied sites.

$$r_f = k_f \cdot n \cdot (1 - X)[O_2] \qquad r_b = k_b \cdot n \cdot X \tag{8.1}$$

The variables k_f and k_b are the forward and backward proportionality constants. The ratio $K = \frac{k_b}{k_f}$ represents the relative on/off rate and has units of concentration. At equilibrium the forward and backward reaction rates are equal: $k_f \cdot n \cdot (1 - X)[O_2] = k_b \cdot n \cdot X$.

Solving this equation for X and plugging in K gives the equation:

$$X = \frac{[O_2]}{K + [O_2]} \tag{8.2}$$

The fraction of sites occupied X is a function of the oxygen concentration $[O_2]$ and the on/off rate K. When K and $[O_2]$ are equal $X = \frac{1}{2}$.

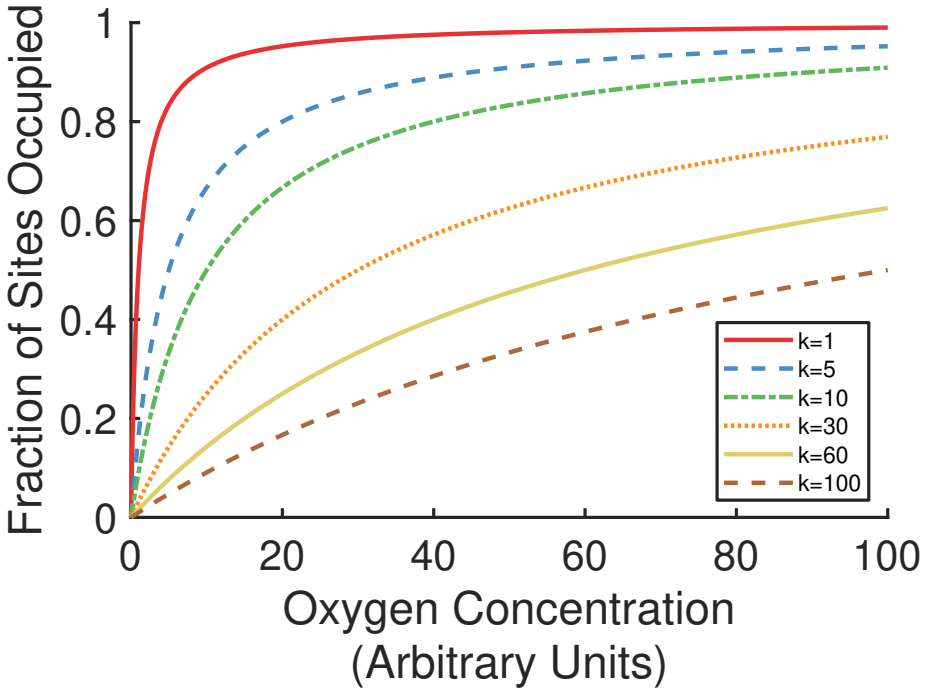

Figure 8.10: Langmuir curves for selected values of k

It is possible that the rake face Langmuir surface has a very small K value, such that the surface is effectively always full. This would make it difficult to rigorously exclude oxygen from the experiment and would explain the stability of wear rates as the oxygen concentration changes, even at very low partial pressures. Even a few parts per million of oxygen in the enclosure could cause the surface to stay filled if K is sufficiently small.

CHAPTER 9: CONCLUSIONS

This dissertation uses tool wear residual measurements as a tool to evaluate: wear of diamond when cutting Cu-Ni alloys as a function of cutting distance, cutting forces and tool wear when machining Cu-Ni alloys, and the relationship between wear rates and oxygen partial pressure. A detailed evaluation of measurement uncertainty for tool wear residual measurements is also performed.

The plunge cut residual measurement methods described here have position-dependent uncertanties ranging from 2 nm to 30 nm. Plastic flow of the UBAC witness sample can cause high-frequency surface structures to present in the residual measurement, and poorly sharpened tools can cause outliers which have low measurement uncertainty, but are not useful experimental results. A large amount of experiments were conducted to allow statistical methods to be used to reject these outliers in many cases. The experimental method and corresponding uncertainty evaluation described here provide a robust method for measuring edge recession of cutting tools as a function of position along the cutting edge. While the results acheived here are sufficient, modulating the feedrate to reduce plastic flow from burnishing, conducting the experiments in an environment with better temperature control, and more complete characterization of tools before and after each experiment could improve the quality of the measurements.

Experimental outliers were not an uncommon occurence. These outliers could be due to imhomogeneity of the diamond lattice, incomplete sharpening of the cutting edge, excessive roughness or waviness of the rake face radius, environmental temperature variations, or error motions of the diamond turning machine. The root cause of some outliers was identified, but most were rejected via statistical methods. For

a group of experiments with identical parameters, any single experiment more than three standard deviations from the mean of that group was rejected.

While this dissertation applies the method to single crystal diamond tools, it could just as easily be applied to polycrystalline tools. Future work could include an evaluation of residual measurement uncertainty using iterative close point (ICP) or other modern, robust registration algorithms to align the plunges.

Cutting and thrust forces on the cutting tool are under 500 mN when facing Monel, even after the tool becomes worn. There is a linear relationship between force and cutting distance when facing Monel, excluding a 'run-in' period occuring during the first facing pass. This step increase in force implies that multiple wear mechanisms are at work during the first facing pass, when the tool is still extremely sharp. The small cutting edge radius of a newly sharpened tool is vulnerable to mechanical damage. It is likely that the newly sharpened edge is mechanically abraded until a cutting radius is reached that allows chemical processes to dominate future wear. It is possible that very little cutting distance is required for this to happen. Future work could explore this idea two ways. One would be to perform experiments were only one facing pass is performed, then inspect the tool for signs of mechanical wear in an SEM. The other would be to perform experiments were six (or more) facing passes are with 50 m of cutting distance per pass (instead of the current 500 m), giving a small delta between plunges. If the same effect is observed this supports the idea that it occurs very quickly and is difficult to avoid.

A similar effect was observed when plunging into UBAC, but forces dropped after the first plunge instead of rising. The most likely cause is an errant chip pressing on the tool during the first plunge.

Edge recession of diamond tools as a function of cutting distance was found to match previous work by Browy in terms of magnitude. In addition, differing morphology and rate of wear along the nose and leading edge were investigated. Nose wear

can be seen as a separate 'bump' at the tool nose, while leading edge wear increases with uncut chip thickness. Nose wear is expected to be dominated by burnishing, while leading edge wear is driven by higher temperatures as uncut chip thickness increases. As the uncut chip thickness increases more work must be done by the tool (at each $d\theta$ along the leading edge), increasing the local temperature. The 'running-in' effect is observed along the leading edge, but for the residual analyzed in Chapter 6 nose wear increases linearly. This makes sense when the 'running-in' mechanics described above are applied. When the uncut chip becomes sufficiently thin the tool is now rubbing against the workpiece instead of cutting.

Leading edge wear and uncut chip thickness were found to have a strong correlation. This further supports the hypothesis that higher local temperatures result in higher local wear rates.

Hypothesis proposing a model for changes in crystal wear as the crystal lattice is rotated was developed and tested. This model proposed that crater wear on the rake face will not vary with tool orientation, and that edge recession will vary with orientation of the tool. Both of these hypotheses were supported by the experiments performed. However, there is an unexplained increase in the rate of wear when using the custom tools.

Diamond tool wear does not appear to vary as a function of oxygen partial pressure. This result is superficially counterintuitive, but can be explained by a Langmuir film surface model. Accounting for surface films on the diamond, humidity, temperature, and any instability in the DTM due to the dynamics of the large mass hanging on the spindle should be a part of any future work.

CHAPTER 10: FUTURE WORK: PROPOSED TOOL WEAR CHARACTERIZATION EXPERIMENTS

10.1 Measurement of activation energy

Chemical wear of diamond tools can be described using Equation 2.1. This model describes the wear rate in terms of an activation energy E_a. Direct measurement of this number would allow for validation and refinement of existing models. Values for this activation energy depend on the thermal conductivity of the diamond and the particular alloy being machined. Childs et. al. estimated values ranging from 15–60 kJ/mole when milling Monel 400 with a polycrystalline diamond (PCD) tool [4]. Lane et. al. used a combination of wear measurements and finite-element temperature modeling to create a similar thermo-chemical model for SCD turning of low carbon steel [69].

If the system temperature is actively controlled and the resulting change in wear rates is recorded, a more complete measurement of E_a can be performed. This experiment can be carried out using the system shown in Figure 10.1. Current is provided to the heating element through the slip ring, which also can provide measurements of the workpiece temperature from embedded temperature sensors. A similar heating element could be used to bring the tool to the same temperature as the workpiece. Doing this with thermally 'pin' the cutting interface between the two higher-temperature systems, forcing the cutting interface to the higher baseline temperature. Kinematic couplings allow different alloys to be tested with minimal effort, at the cost of lower stiffness. Similar fixturing, using dowel pins instead of kineamtic joints, would be provide a less flexible but easier to manufacture and assemble setup. This fixture also allows experiments to be performed at a constant surface speed.

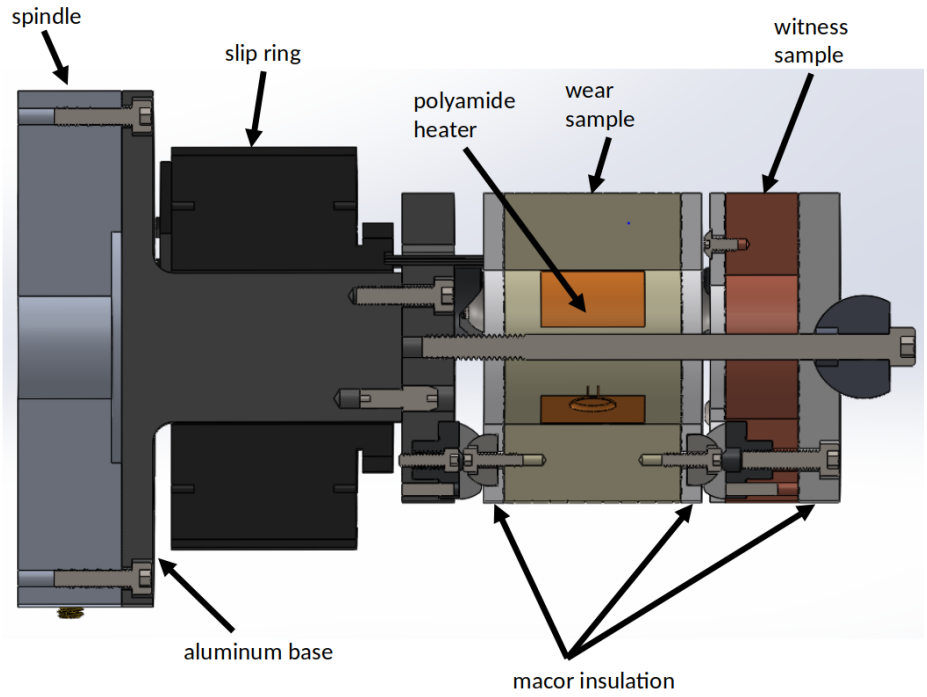

Figure 10.1: Setup for conducting wear rate experiments while controlling the workpiece temperature.

10.2 Measurement of temperatures at the cutting interface

Direct measurement of temperatures at the cutting interface would also allow for direct validation of Arrhenius models. Measurements of diamond tool temperature when cutting have been performed by mounting an RTD to the rake face [45], and by manufacturing tools with thermocouples embedded in the diamond [2]. Both of these methods provide valuable data, but the measurements are made relatively far from the cutting edge. Because diamond has such high thermal conductivity, temperature measurements as as close to the cutting edge as possible are needed to evaluate the accuracy of a model with confidence.

Two approaches to acheiving this goal are presented here. Deposition of thermocouples directly onto the rake face, and measurement of temperatures by applying a thin layer of gold or nickel to the side of a thin chisel tool and measuring the temprature of the metallic film. Deposition of nickel onto diamond has been performed

successfully, but integration of a complete thermocouple has proved challenging.

Measurement via thermal camera bypasses this particular problem, but presents its own drawbacks. Alignment of the tool, workpiece, and optical system would be challenging. The measurement is also indirect; the film temperature is being measured and used to infer the diamond temperature.

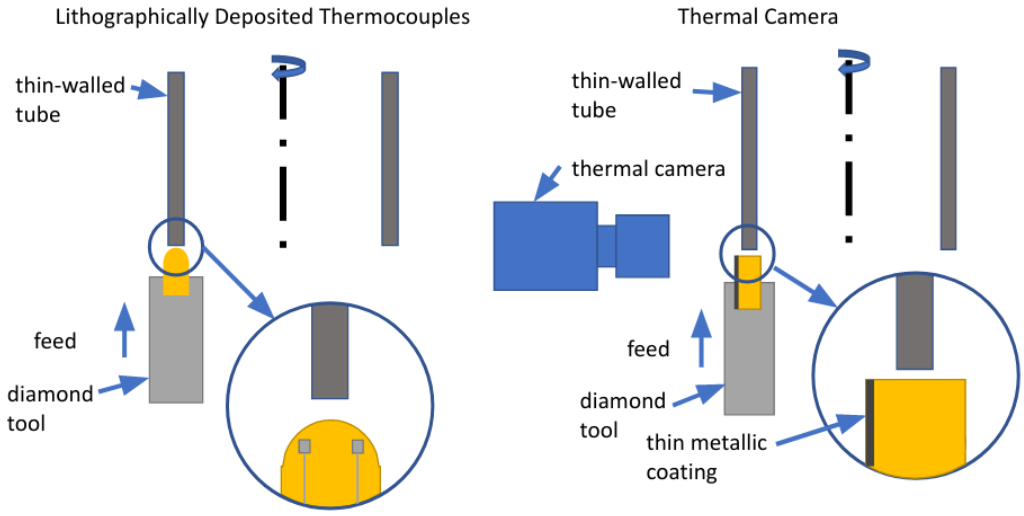

Figure 10.2: Two possible methods of measuring temperature at the cutting interface. The thermocouples allow essentially infinite lateral resolution by plunging repeatedly, moving the tool laterally each time.

10.3 Improved characterization of edge recession

Combining any number of the techniques listed in Table 1.1 with the witness sample method developed in this document would provide a more complete picture of how tool wear evolves as cutting distance increases. One particular combination of measurements is proposed below (Figure 10.3).

The same experiment described in Chapter 3 is performed, with the addition of a dynamometer-mounted indium plate fixed to the machine frame. Before each cutting pass the tool creates an indentation in the plate and a plunge in the witness sample. The indentations provide a three-dimensional representation of the cutting edge that can be measured directly, or by replication. If precise measurements of cutting edge

radius are desired AFM measurements of the replicated edge are probably the best approach. Direct measurement by SEM would provide high-resolution measurements of V_b, allowing better characterizaiton of the effect of burnishing. These SEM measurements could be combined with EBID to provide intermittent measurements of cutting edge radius along the cutting edge.

The data from this experiment would allow correlations between cutting edge sharpness, edge recession, cutting distance, and cutting forces to be explored.

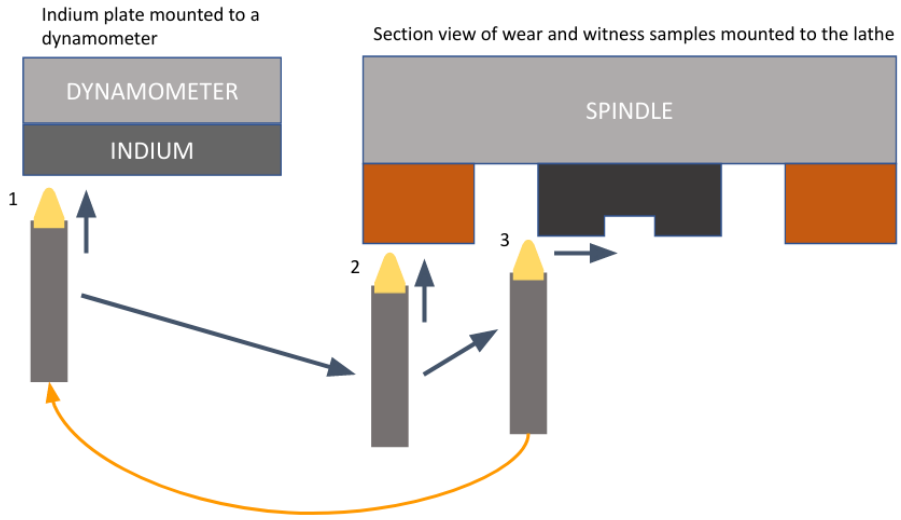

Figure 10.3: Experiment designed to measure V_b, cutting edge sharpness, and edge recession as a function of cutting distance.

REFERENCES

[1] E. Paul, C. J. Evans, A. Mangamelli, M. L. McGlauflin, and R. S. Polvani, "Chemical aspects of tool wear in single point diamond turning," *Precision Engineering*, vol. 18, no. 1, pp. 4–19, 1996.

[2] G. Gubbels, *Diamond turning of glassy polymers*. PhD thesis, Eindhoven Technical University, 2006.

[3] E. C. Browy, "The evaluation of chemical wear on single crystal diamond tools while diamond turning a binary cu-no alloy system," Master's thesis, The University of North Carolina at Charlotte.

[4] T. Childs, C. Tyler, C. J. Evans, T. L. Schmitz, E. Paul, and E. C. Browy, "Estimation of cutting conditions in precision micromachining of CuNi alloys of varying composition," *Procedia CIRP*, vol. 14, pp. 383–388, 2014.

[5] T. Childs, C. J. Evans, E. C. Browy, J. R. Troutman, and E. Paul, "Tool temperatures and wear in micro-machining Cu-Ni alloys with diamond tools: Models, simulations and experiments," *Procedia CIRP*, vol. 31, pp. 270–275, 2015.

[6] M. A. Davies, C. J. Evans, R. R. Vohra, B. C. Bergner, and S. R. Patterson, "Application of precision diamond machining to the manufacture of microphotonics components," *Lithographic and Micromachining Techniques for Optical Component Fabrication II*, vol. 5183, p. 94, 2003.

[7] R. L. Rhorer and C. J. Evans, "Fabrication of optics by diamond turning," *Handbook of Optics*, pp. 41.1–41.13, 1995.

[8] M. Liu, J. A. Shultz, J. D. Owen, M. A. Davies, and T. J. Suleski, "Moth's eye: anti-reflection gratings on germanium freeform surfaces," *Current Developments in Lens Design and Optical Engineering XV*, vol. 9192, p. 91920L, 2014.

[9] E. Brinksmeier, R. Gläbe, and L. Schönemann, "Review on diamond-machining processes for the generation of functional surface structures," *CIRP Journal of Manufacturing Science and Technology*, vol. 5, no. 1, pp. 1–7, 2012.

[10] M. Beier, S. Scheiding, A. Gebhardt, R. Loose, S. Risse, R. Eberhardt, and A. Tünnermann, "Fabrication of high precision metallic freeform mirrors with magnetorheological finishing (MRF)," *Optifab 2013*, vol. 8884, no. 0, p. 88840S, 2013.

[11] N. W. Horvath and M. A. Davies, "Concurrent engineering of a next-generation freeform telescope: mechanical design and manufacture," *Proceedings of SPIE*, vol. 109989, p. 35, 2019.

[12] D. Gurganus, S. Novak, A. Symmons, and M. Davies, "Process evaluation and optimization for freeform precision glass molding," *Proceedings of SPIE*, vol. 1148710, p. 31, 2020.

[13] D. Gurganus, J. D. Owen, M. A. Davies, B. S. Dutterer, S. Novak, and A. Symmons, "Precision glass molding of freeform optics," *SPIE Optical Manufacturing and Testing XII*, vol. 10742, p. 28, 2018.

[14] G. Liu, J.-H. Staasmeyer, O. Dambon, and T. Grunwald, "Scalability of the precision glass molding process for an efficient optics production," *SPIE Optical Manufacturing and Testing XII*, vol. 10742, p. 17, 2018.

[15] J. Reimers, A. Bauer, K. P. Thompson, and J. P. Rolland, "Freeform spectrometer enabling increased compactness," *Light: Science & Applications*, vol. 6, no. 7, pp. e17026–e17026, 2017.

[16] C. J. Evans, *Precision Engineering:An Evolutionary View*. Cranfield Press, 1989.

[17] J. M. Casstevens and C. E. Daugherty, "Diamond Turning Optical Surfaces On Electroless Nickel," *Proc. of SPIE: Precision Machining of Optics*, vol. 0159, pp. 109–113, 1978.

[18] J. S. Taylor, C. K. Syn, T. T. Saito, and R. R. Donaldson, "Surface finish measurements of diamond-turned electroless-nickel-plated mirrors," *Optical Engineering*, vol. 25, no. 9, pp. 1013–1020, 1986.

[19] J. W. Dini, R. R. Donaldson, and C. K. Syn, "Diamond tool wear of electrodeposited nickel-phosphorus alloy," *SUR/FIN '90: 77th American Electroplaters and Surface Finishers Society*, 1990.

[20] E. Brinksmeier and R. Gläbe, "Advances in precision machining of steel," *CIRP Annals - Manufacturing Technology*, vol. 50, no. 1, pp. 385–388, 2001.

[21] R. Bohr, "Diamond machining of steel molds for optical components," *Advanced Optical Technologies*, vol. 5, no. 4, pp. 289–291, 2016.

[22] D. Ravindra, S. K. Kode, C. Stroshine, D. Morrison, and M. Mitchell, "Micro-laser assisted machining: the future of manufacturing silicon optics," *Proceedings of SPIE*, vol. 10448, 2017.

[23] H. Shahinian, D. Zaytsev, J. Navare, Y. Su, D. Kang, and D. Ravindra, "Micro laser assisted machining (µ-lam) of precision optics," in *Optical Design and Fabrication 2019 (Freeform, OFT)*, p. OT1A.5, Optical Society of America, 2019.

[24] D. Kang, J. Navare, Y. Su, D. Zaytsev, D. Ravindra, and H. Shahinian, "Observations on ductile laser assisted diamond turning of tungsten carbide," in *Optical Design and Fabrication 2019 (Freeform, OFT)*, p. JT5A.11, Optical Society of America, 2019.

[25] C. Bodlapati, *Diamond turning of plastic optics*. PhD thesis, North Carolina State University, 2019.

[26] C. Bodlapati, K. Garrard, T. A. Dow, and A. Wong, "Surface finish and diamond tool wear when machining PMMA and PC optics," *Proceedings of SPIE*, vol. 10742, p. 14, 2018.

[27] T. Moriwaki and E. Shamoto, "Ultra-precision diamond turning of stainless steel by applying ultrasonic vibration," *Journal of the Japan Society for Precision Engineering*, vol. 40, no. 1, p. 559, 1991.

[28] Y. Zhang, Z. Zhou, J. Wang, and X. Li, "Diamond tool wear in precision turning of titanium alloy," *Materials and Manufacturing Processes*, vol. 28, no. 10, pp. 1061–1064, 2013.

[29] S. Shimada, T. Inamura, M. Higuchi, H. Tanaka, and N. Ikawa, "Suppression of tool wear in diamond turning of copper under reduced oxygen atmosphere," in *Annals of the ClRP*, vol. 49, pp. 21–24, 2000.

[30] C. J. Evans and J. B. Bryan, "Cryogenic diamond turning of stainless steel," *CIRP Annals - Manufacturing Technology*, vol. 40, no. 1, pp. 571–575, 1991.

[31] M. Weck and J. Luderich, "Influence of thermal expansion of the cutting tool on the workpiece accuracy during diamond turning," *SPIE*, vol. 1266, pp. 216–225, 1990.

[32] R. Malz, E. Brinksmeier, W. Preuss, J. Kohlscheen, H. R. Stock, and P. Mayr, "Investigation of the diamond machinability of newly developed hard coatings," *Precision Engineering*, vol. 24, no. 2, pp. 146–152, 2000.

[33] J. Kohlscheen, H. R. Stock, and P. Mayr, "Substoichiometric titanium nitride coatings as machinable surfaces in ultraprecision cutting," *Surface and Coatings Technology*, vol. 120-121, pp. 740–745, 1999.

[34] E. Brinksmeier, R. Gläbe, and J. Osmer, "Ultra-precision diamond cutting of steel molds," *CIRP Annals - Manufacturing Technology*, vol. 55, no. 1, pp. 551–554, 2006.

[35] R. Berman, ed., *Physical Properties of Diamond*. Oxford University Press, 1st ed., 1965.

[36] J. Field, ed., *Properties of Diamond*. London: Academic Press Inc., 1979.

[37] A. G. Thornton and J. Wilks, "The wear of diamond tools turning mild steel," *Wear*, vol. 65, no. 1, pp. 67–74, 1980.

[38] A. G. Thornton and J. Wilks, "Tool wear and solid state reactions during machining," *Wear*, vol. 53, no. 1, pp. 165–187, 1979.

[39] J. Wilks, "Performance of diamonds as cutting tools for precision machining," *Precision Engineering*, vol. 2, no. 2, pp. 57–72, 1980.

[40] F. Z. Fang and V. C. Venkatesh, "Diamond cutting of silicon with nanometric finish," *CIRP Annals - Manufacturing Technology*, vol. 47, no. 1, pp. 45–49, 1998.

[41] F. Z. Fang, H. Wu, W. Zhou, and X. T. Hu, "A study on mechanism of nano-cutting single crystal silicon," *Journal of Materials Processing Technology*, vol. 184, no. 1-3, pp. 407–410, 2007.

[42] M. Shi, B. M. Lane, C. B. Mooney, T. A. Dow, and R. O. Scattergood, "Diamond tool wear measurement by electron-beam-induced deposition," *Precision Engineering*, vol. 34, no. 4, pp. 718–721, 2010.

[43] W. Gao, T. Motoki, and S. Kiyono, "Nanometer edge profile measurement of diamond cutting tools by atomic force microscope with optical alignment sensor," *Precision Engineering*, vol. 30, no. 4, pp. 396–405, 2006.

[44] D. L. Decker, H. H. Hurt, J. H. Dancy, and C. W. Fountain, "Preselection of diamond single-point tools," *Production Aspects of Single Point Machined Optics*, vol. 0508, no. December 1984, p. 132, 1984.

[45] B. Suit, *Analysis of Accelerated Tool Wear and Built Up Edge When Diamond Turning Ferrous Materials*. PhD thesis, North Carolina State University, 2016.

[46] D. Mullner, "Verifying Nd-Tool quality using plunge cuts and micro-interferometer," in *SPIE*, vol. 0645, p. 20, 1986.

[47] Kevin Kendall, "Adhesion: Molecules and Mechanics," *Science*, vol. 263, no. 5154, pp. 1720–1725, 1994.

[48] W. J. Zong, Z. Q. Li, T. Sun, D. Li, and K. Cheng, "Analysis for the wear resistance anisotropy of diamond cutting tools in theory and experiment," *Journal of Materials Processing Technology*, vol. 210, no. 6-7, pp. 858–867, 2010.

[49] S. J. Zhang, S. To, and G. Q. Zhang, "Diamond tool wear in ultra-precision machining," *International Journal of Advanced Manufacturing Technology*, vol. 88, no. 1-4, pp. 613–641, 2017.

[50] C. V. Raman and S. Ramaseshan, "The crystal forms of diamond and their significance," *Proceedings of the Indian Academy of Sciences*, 1946.

[51] S. Ramaseshan, "A theory of the crystal forms of diamond," *Proceedings of the Indian Academy of Sciences*, pp. 122–129, 1946.

[52] J. F. Verrill, "Use of the Talystep in Investigating Diffraction Grating Groove Profiles," *Journal of Physics E: Scientific Instruments*, vol. 6, no. 12, pp. 1199–1201, 1973.

[53] J. F. Verrill, "A study of blazed diffraction grating groove profiles using an improved talystep stylus," *Optica Acta*, vol. 23, no. 6, pp. 425–432, 1976.

[54] C. J. Wong, "Fracture and wear of diamond cutting tools," *American Society of Mechanical Engineers (Paper)*, vol. 103, no. 81, 1981.

[55] R. E. Glardon and I. Finnie, "Some observations on the wear of single point diamond tools used for machining glass," *Journal of Material Science*, vol. 16, pp. 1776–1784, 1981.

[56] C. K. Syn, J. S. Taylor, and R. R. Donaldson, "Diamond tool wear vs cutting distance on electroless nickel mirrors.," in *SPIE Vol. 676 Ultraprecision Machining and Fabrication of Optics*, 1986.

[57] H. H. Hurt and G. A. Showman, "Wear Test Of A Preselected Diamond Tool," *Ultraprecision Machining and Automated Fabrication of Optics*, vol. 0676, no. February 1987, p. 116, 1987.

[58] C. J. Evans, E. C. Browy, T. Childs, and E. Paul, "Interferometric measurements of single crystal diamond tool wear," *CIRP Annals - Manufacturing Technology*, vol. 64, no. 1, pp. 125–128, 2015.

[59] K. Venditti, "Design for metrology of freeform optics," Master's thesis, University of North Carolina at Charlotte, 2020.

[60] C. Hovis, "Optical metrology of freeform optics utilizing interferometric stitching," Master's thesis, University of North Carolina at Charlotte, 2019.

[61] J. R. Troutman, *Cutting mechanics and manufacture of optics for imaging applications*. PhD thesis, The University of North Carolina at Charlotte, 2016.

[62] J. D. Drescher and T. A. Dow, "Tool force model development for diamond turning," *Precision Engineering*, vol. 12, no. 1, pp. 29–35, 1990.

[63] J. D. Owen, M. A. Davies, D. Schmidt, and E. H. Urruti, "On the ultra-precision diamond machining of chalcogenide glass," *CIRP Annals - Manufacturing Technology*, vol. 64, no. 1, pp. 113–116, 2015.

[64] J. T. Carroll III, T. A. Dow, and J. S. Strenkowski, "Tool Force Measurement And Prediction In Diamond Turning," *Ultraprecision Machining and Automated Fabrication of Optics*, vol. 0676, p. 104, 1987.

[65] F. Bowden and D. Tabor, "Deformation, friction and wear of diamond," in *Physical Properties of Diamond* (R. Berman, ed.), pp. 184–219, Oxford: Clarendon Press, 1965.

[66] N. Ikawa and S. Shimada, "Cutting tool for ultraprecision machining," in *Proceedings of 3rd International Conference on Production Engineering*, (Kyoto), 1977.

[67] M. Burnham, "The mechanics of micromachining," *SPIE, Advances in Precision Machining of Optics*, vol. 93, 1976.

[68] M. P. Hitchiner and J. Wilks, "Factors affecting chemical wear during machining," *Wear*, vol. 93, no. 1, pp. 63–80, 1984.

[69] B. M. Lane, T. A. Dow, and R. O. Scattergood, "Thermo-chemical wear model and worn tool shapes for single-crystal diamond tools cutting steel," *Wear*, vol. 300, no. 1-2, pp. 216–224, 2013.

APPENDIX A: MATLAB CODE

A.1 Script for plunge processing

```
zScaleFactor = 10^6;
processedData = PlungeProcessing(output(1:6));
processedData.ResidCalcType = 'subtractFit';
processedData.UserSelect = 0;
processedData.TrimH = 9.25;
processedData.TrimZo = -.6;

%% main program
%% prepare data for final alignment
% change z scale from meters to um
for ii = 1:processedData.Nplunges
    processedData.MapData(ii).PhaseMap = processedData.MapData(ii).PhaseMap*zScaleFactor;
    processedData.MapData(ii).Zscale   = 'um';
end

processedData.CheckMapOrientation();
processedData.RemovePlane();
processedData.RotateMaps();
processedData.GetAvgSlices();

% add most current property data to the plunge traces
for ii = 1:processedData.Nplunges
    processedData.TraceData(ii).dx = processedData.MapData(ii).dx;
    processedData.TraceData(ii).Xscale = processedData.MapData(ii).Xscale;
    processedData.TraceData(ii).Zscale = processedData.MapData(ii).Zscale;
end

processedData.InterpTraces();
processedData.PlotSlices();   % see if column average went well

processedData.AlignPlungesTrim();
% processedData.AlignPlungesSlope();

processedData.PlotSlices();   % see if alignment went well
processedData.FitFirstPlunge(0);

% add most current property data to the plunge residuals
for ii = 1:processedData.Nplunges
    processedData.ResidualData(ii).dx = processedData.TraceData(ii).dx;
    processedData.ResidualData(ii).Xscale = processedData.TraceData(ii).Xscale;
    processedData.ResidualData(ii).Zscale = processedData.TraceData(ii).Zscale;
end

processedData.CalcResiduals();
processedData.PlotResiduals();
```

A.2 Script for Monte Carlo analysis

```
N = 100;
k = 2; % expanded uncertainty

% monte carlo options
addShift    = 1;
addRotation = 1;
addPlane    = 1;
addNoise    = 1;
useRealData = 1;
% updateScale = 1;

removeRotation = 1;
removePlane    = 1;
% data processing options

% options are 'subtractFit' and 'subtractPlungeZero'
residCalcMethod = 'subtractPlungeZero';
% options are 'trim' and 'slope'
alignMethod     = 'trim'; % other option is 'slope'
%% create the fake data object
if useRealData
    load('realPlungeMapInput2.mat');
end
for ii = 1:N
    fakeData(ii) = FakeData(); %#ok<*SAGROW>

    fakeData(ii).RotationRange = [-.2, .2];
    fakeData(ii).NormalVecRange = [-.1, .1];
    fakeData(ii).ShiftRange = [-10, 10];
    fakeData(ii).PlaneOffsetRange = [-1, 1];
    fakeData(ii).MeasNoiseRange = .005;

    %% operations on plunge trace
    % create a plunge trace
    if useRealData
        fakeData(ii).CreatePhaseMap(realData); %#ok<UNRCH>
        fakeData(ii).Name = 'Real Data';
        fakeData(ii).PhaseMap = fakeData(ii).PhaseMap'.*10^6;
    else
        fakeData(ii).CreatePlungeTrace();
        fakeData(ii).CreatePhaseMap();
        fakeData(ii).Name = 'Fake Data';
    end
    %% operations on phasemap
    if addShift
        fakeData(ii).AddShift(); %#ok<UNRCH>
    end
    if addRotation
        fakeData(ii).AddRotation(); %#ok<UNRCH>
    end
    if addPlane
        fakeData(ii).AddPlane(); %#ok<UNRCH>
    end
    if addNoise
        fakeData(ii).AddNoise(); %#ok<UNRCH>
    end
end

%% create plunge processing object
processedData = PlungeProcessing(fakeData);
processedData.ResidCalcType = residCalcMethod;
processedData.UserSelect    =  0    ;
processedData.TrimH         =  9    ;
processedData.TrimZo        = -1    ;
processedData.dzTrim        =  0.001;
processedData.UnwornSection = [100; 180];

%% process fake data

processedData.CheckMapOrientation();

processedData.InterpMaps()

if removePlane
    processedData.RemovePlane(); %#ok<UNRCH>
end
if removeRotation
    processedData.RotateMaps(); %#ok<UNRCH>
end

processedData.GetAvgSlices();

for ii = 1:processedData.Nplunges
    processedData.TraceData(ii).dx = processedData.MapData(ii).dx;
    processedData.TraceData(ii).Xscale = processedData.MapData(ii).Xscale;
    processedData.TraceData(ii).Zscale = processedData.MapData(ii).Zscale;
end

processedData.PlotSlices();   % see if column average went well
```

```
91  
    switch alignMethod
        case 'trim'
93          processedData.AlignPlungesTrim();
        case 'slope'
95          processedData.GetThetaShift();
            processedData.AlignPlungesSlope();
97  end

99  for ii = 1:N
        minLength = min(processedData.TrimmedPlungeLengths);
101     processedData.TraceData(ii).Trace = processedData.TraceData(ii).Trace(1:minLength);
    end
103 
    processedData.FitFirstPlunge(0);
105 
    % add most current property data to the plunge residuals
107 for ii = 1:processedData.Nplunges
        processedData.ResidualData(ii).dx = processedData.MapData(ii).dx;
109     processedData.ResidualData(ii).Xscale = processedData.MapData(ii).Xscale;
        processedData.ResidualData(ii).Zscale = processedData.MapData(ii).Zscale;
111 end

113 processedData.CalcResiduals();

115 %% create uncertainty calc objects
    % create avg of residuals object
117 meanResid = SurfAnalysis();
    meanResid.Xscale = 'um';
119 meanResid.Zscale = 'nm';
    meanResid.dx = processedData.dxInterp;
121 meanResid.Name = 'Average of N Residuals';

123 % create std dev of residuals object
    stdResid = SurfAnalysis();
125 stdResid.Xscale = 'um';
    stdResid.Zscale = 'nm';
127 stdResid.dx = processedData.dxInterp;
    stdResid.Name = 'Std Dev of N Residuals';
129 
    %% calculate uncertainty
131 % outer loop moves along x axis
    % inner loop moves from plunge to plunge
133 for jj = 1:length(processedData.ResidualData(2).X)
        for ii = 2:processedData.Nplunges
135         % store value of each residual at x(jj)
            z(ii) = processedData.ResidualData(ii).Trace(jj);
137     end
        meanResid.Trace(jj) = mean(z).*10^3;
139     stdResid.Trace(jj)  = std(z).*10^3;
    end
141 
    processedData.PlotResiduals();
143 
    figure
145 meanResid.Plot();
    hold on
147 stdResid.Trace = stdResid.Trace*k;
    stdResid.Plot();
149 
    legend('mean', 'std');
151 figure
    stdResid.Plot();
```

A.3 Class for surface data type and manipulation methods

```
classdef SurfAnalysis < handle
properties
    Zscale {mustBeMember(Zscale,{'m','cm','mm', 'um', 'nm'})} = 'm'
    Xscale {mustBeMember(Xscale,{'m','cm','mm', 'um', 'nm'})} = 'm'
    dx
%         FilteredState
    Trace    double
    PhaseMap double
    Name     char
end
properties (Dependent)
    X     double
    XY    cell
    Nrows double
    Ncols double
end

methods
    function surfObj = SurfAnalysis(surfaceData, dx, Zscale, Xscale)
        % Construct an instance of this class
        if nargin == 4
            if (size(surfaceData, 1) == 1) || (size(surfaceData, 2) == 1)
                surfObj.Trace = surfaceData;
            else
                surfObj.PhaseMap = surfaceData;
            end
            surfObj.dx = dx;
            surfObj.Zscale = Zscale;
            surfObj.Xscale = Xscale;
        end
    end

    function Plot(surfObj)
        if ~isempty(surfObj.PhaseMap)
            XY = surfObj.XY; %#ok<*PROP>
            [XX,YY] = meshgrid(XY{1}, XY{2});
            surf(XX, YY, surfObj.PhaseMap,'LineStyle','none');
            view(0,90)
            axis([0, XY{1}(end), 0, XY{2}(end)]);
            ylabel(['Y (', surfObj.Xscale, ')']);
            xlabel(['X (', surfObj.Xscale, ')']);
            c = colorbar;
            c.Label.String = ['Z (', surfObj.Zscale, ')'];
            c.Label.FontSize = 12;
        elseif ~isempty(surfObj.Trace)
            XX = surfObj.X;
            plot(XX, surfObj.Trace);
            ylabel(['Z (', surfObj.Zscale, ')']);
            xlabel(['X (', surfObj.Xscale, ')']);
        end
    end

    function avgSlice = GetAvgSlice(surfObj, dim)
    assert(~isempty(surfObj.PhaseMap),...
           'There is no PhaseMap in the object!');
    if dim == "row"
        avgSlice = nanmean(surfObj.PhaseMap, 1);
    elseif dim == "col"
        avgSlice = nanmean(surfObj.PhaseMap, 2);
    end
    end

    function mapSlice = GetSlice(surfObj, ind, dim)
        mustBeNonempty(surfObj.PhaseMap);
        assert(isa(surfObj,'SurfAnalysis'),...
           'GetSlice Error:  Input obj is of class %s, not a SurfAnalysis object.',...
            class(surfObj));
        if dim == "row"
            mapSlice = surfObj.PhaseMap(ind, :);
        elseif dim == "col"
            mapSlice = surfObj.PhaseMap(:, ind);
        end
    end

    function surfObj = RotateSurf(surfObj, rotAngle)
        surfObj.PhaseMap = imrotate(surfObj.PhaseMap, rotAngle, 'bilinear', 'crop');
    end

    function InterpMap(surfObj, dxNew)
        mustBeNonempty(surfObj.PhaseMap);
        N = size(surfObj.PhaseMap, 1);
        xx = linspace(0, N*surfObj.dx, N);
        [XX, ~] = meshgrid(xx, xx);
        Ninterp = floor(xx(end)/dxNew);
        xQ = linspace(0, Ninterp*dxNew, Ninterp);
        Xq = meshgrid(xQ, xQ);
        surfObj.PhaseMap = interp2(XX, XX', surfObj.PhaseMap, Xq, Xq', 'bilinear');
        surfObj.dx = dxNew;
    end % InterpMap
```

```
90
        function InterpTrace(surfObj, dxNew)
92          mustBeNonempty(surfObj.Trace);
            N = length(surfObj.Trace);
94          xx = linspace(0, N*surfObj.dx, N);
            Ninterp = floor(xx(end)/dxNew);
96          xQ = linspace(0, Ninterp*dxNew, Ninterp);
            surfObj.Trace = interp1(xx, surfObj.Trace, xQ, 'linear');
98          surfObj.dx = dxNew;
        end % InterpTrace
100
        function fitPlane = FitPlane(surfObj)
102         % replace surfObj.PhaseMap with Z
            [x, y] = meshgrid(1:1:size(surfObj.PhaseMap, 2),...
104                           1:1:size(surfObj.PhaseMap, 1));
            XX = x(~isnan(surfObj.PhaseMap));
106         YY = y(~isnan(surfObj.PhaseMap));
            ZZ = surfObj.PhaseMap(~isnan(surfObj.PhaseMap));
108         A = [ones(size(XX)) XX YY]\ZZ; % model
            fitPlane = ones(size(surfObj.PhaseMap)).*A(1) + x.*A(2) + y.*A(3);
110     end

112     function Offset(obj, offsetVal)
            obj.Trace = obj.Trace + offsetVal;
114     end
    %% getter functions
116     function Nrows = get.Nrows(surfObj)
            Nrows = size(surfObj.PhaseMap, 1);
118     end

120     function Ncols = get.Ncols(surfObj)
            Ncols = size(surfObj.PhaseMap, 2);
122     end

124     function X = get.X(surfObj)
            mustBeNonempty(surfObj.Trace);
126         X = linspace(0, length(surfObj.Trace)*surfObj.dx, length(surfObj.Trace))';
        end
128
        function XY = get.XY(surfObj)
130         mustBeNonempty(surfObj.PhaseMap);
            XY{1} = linspace(0, size(surfObj.PhaseMap, 1)*surfObj.dx, size(surfObj.PhaseMap, 1))';
132         XY{2} = linspace(0, size(surfObj.PhaseMap, 2)*surfObj.dx, size(surfObj.PhaseMap, 2))';
        end
134 end
    end
```

A.4 Class for Monte Carlo methods

```
classdef FakeData < SurfAnalysis
    properties
        RotationRange(1,2) double
        NormalVecRange(1,2) double
        ShiftRange(1,2) double
        PlaneOffsetRange(2,1) double
        MeasNoiseRange(1,1) double
        CuspWidth double
    end
    properties(Constant)
        FeedRate double = 2; % um/rev
        PlungeDepth double = 10; % um
        SpindleSpeed double = 1000; % rpm
    end

    methods
        function obj = FakeData()
            dx = PlungeProcessing.FOV/PlungeProcessing.Pixels;
            obj = obj@SurfAnalysis([], dx, 'um', 'um');
        end % constructor

        function set.CuspWidth(obj, val)
            obj.CuspWidth = val;
        end

        % methods for Traces
        function CreatePlungeTrace(obj)
            % anonymous function for circle formula
            % k = y offset |  h = x offset
            y = @(r, x, h, k) -sqrt(r.^2 - (x - h).^2) + k;
            xLim = PlungeProcessing.FOV/2;
            x = linspace(-xLim, xLim, PlungeProcessing.Pixels);
            hCirc = 0; % circle has no shift in the x direction
            kCirc = PlungeProcessing.R; % shift the circle center up to y = tool radius
            zTrace = real(y(PlungeProcessing.R, x, hCirc, kCirc));
            % create flat spots on either side of plunge
            % this step also sets the DOC
            zTrace( zTrace >= (obj.PlungeDepth) ) = obj.PlungeDepth;
            % adjust y offset so that flats are at 0
            zTrace = zTrace - obj.PlungeDepth;
            obj.Trace = zTrace;
        end

        function CreatePhaseMap(obj, realPlunge)
            mustBeNonempty(obj)
            if nargin == 1
                obj.PhaseMap = repmat(obj.Trace, PlungeProcessing.Pixels, 1)';
            else
                obj.PhaseMap = realPlunge.PhaseMap;
            end
        end

        function AddShift(obj)
            mustBeNonempty(obj.PhaseMap);
            Nshift = round(boundedUniformDistr(obj.ShiftRange, 1));
            obj.PhaseMap = circshift(obj.PhaseMap, [Nshift, 1]);
        end

        function PlotTraces(obj)
            figure;
            hold on;
            for ii = 1:length(obj)
                plot(obj(ii).Trace);
            end
        end

        % methods for PhaseMaps
        function AddNoise(obj)
            mustBeNonempty(obj.PhaseMap);
            load('ET2020785quickAstr', 'strMap');
            noiseMap = nan(strMap.Ncols, strMap.Nrows);
            c = 0; % distribution center
            strTrace = strMap.GetAvgSlice('row');
            for ii = 1:strMap.Ncols
                a = -abs(strTrace(ii));
                b =  abs(strTrace(ii));
                noiseMap(:,ii) = boundedButterflyDistr(a, b, c, strMap.Nrows)';
            end
            obj.PhaseMap = obj.PhaseMap ...
                        + .1*abs(noiseMap);
%             obj.PhaseMap = obj.PhaseMap ...
%                         + normrnd(0, obj.MeasNoiseRange,...
%                         [obj.Nrows, obj.Ncols]);
%
        end % add noise to the map

        function AddRotation(obj)
            rotTheta = boundedUniformDistr(obj.RotationRange, 1);
            % pad to rotate
```

```
            padDim = 1400;
            padSize = (padDim-PlungeProcessing.Pixels)/2;
            obj.PhaseMap = padarray(obj.PhaseMap, [padSize padSize], 'replicate', 'both');
            % rotate
            obj.RotateSurf(rotTheta);
            % crop back to size
            cropInd = [padSize,...
                       padSize,...
                       PlungeProcessing.Pixels-1,...
                       PlungeProcessing.Pixels-1];
            obj.PhaseMap = imcrop(obj.PhaseMap, cropInd);
            % cropInd is a vector with form [XMIN YMIN WIDTH HEIGHT];
        end

        function AddPlane(obj)
            vectorAngles = nan(1,3);
            for ii = 1:3
                vectorAngles(ii) = boundedUniformDistr(obj.NormalVecRange, 1);
            end
            % vector normal to the plane being added
            normalVector = makeNormalVector(vectorAngles(1), vectorAngles(2), vectorAngles(3));
            [~, ~, Z] = planeFromNormalVec(obj.XY{1}, obj.XY{2}, normalVector);
            Zoffset = boundedUniformDistr(obj.PlaneOffsetRange, 1);
            obj.PhaseMap = obj.PhaseMap + Z + Zoffset;
        end
    end

end

function vr = makeNormalVector(alpha, beta, gamma)
% rotate a vector using rotation matrices
% euler angles!
% can't rotate about Z first, because the vector is normal to Z!
v = [0 0 1];
% 1: rotate about X (pitch)
% 2: rotate about Y (roll)
% 3. rotate about z (yaw)

sv = size(v);
if sv(1) == 1
    v = v';
end
% this function assumes the input vector originates at [0, 0, 0]

Rx = @(alpha) [1   0              0         ;
               0   cosd(alpha)   -sind(alpha) ;
               0   sind(alpha)    cosd(alpha)];

Ry = @(beta) [cosd(beta)    0   -sind(beta) ;
              0            1    0          ;
             sind(beta)    0    cosd(beta)];

Rz = @(gamma) [cosd(gamma)   -sind(gamma)   0 ;
               sind(gamma)    cosd(gamma)   0 ;
               0             0             1];

vr = Rz(gamma)*Ry(beta)*Rx(alpha)*v;
end

function [X, Y, Z] = planeFromNormalVec(x, y, normalVector)

[X, Y] = meshgrid(x, y);

planeFun = @(x, y, a, b, c) (-a/c).*x + (-b/c).*y;

Z = planeFun(X, Y, normalVector(1), normalVector(2), normalVector(3));

end

function val = boundedUniformDistr(limits, N)
% limits = [ min, max ]
val = limits(1) + (limits(2) - limits(1)).*rand(N);
end

function X = boundedButterflyDistr(a, b, c, N)
% butterfly distribution on the range a to b, centered at c
% https://learnandteachstatistics.files.wordpress.com/2013/07/notes-on-triangle-distributions.pdf
% https://www.mathworks.com/matlabcentral/fileexchange/37698-random-sample-from-discrete-pdf
% a = -1;
% b = 1;
% c = 0;
% pdf = @(x) (0).*(x < a) ...
%          + (2*(c-x)/(b-a)/(c-a)).*(x <= c & x >= a) ...
%          + (2*(x-c)/(b-a)/(b-c)).*(x <= b & x >= c) ...
%          + (0).*(x > b);

x = linspace(a, b, 100000);

cdf = @(x) (0).*(x < a) ...
         + ((a-x).*(a-2*c+x)/(b-a)/(c-a)).*(x <= c & x >= a) ...
         + ((a-c)/(a-b) - (c-x).^2/(a-b)/(b-c)).*(x <= b & x >= c) ...
         + (0).*(x > b);
```

```
183 uniforDistRandomNums = rand(N, 1);

185 X = interp1(cdf(x), x, uniforDistRandomNums', 'linear', 0);
end
```

A.5 Class for plunge processing methods

```
classdef PlungeProcessing < handle

    properties
        MapData       SurfAnalysis
        TraceData     SurfAnalysis
        ResidualData  SurfAnalysis
        DebugData     ProcessingDebug
        PlungeZeroFit double
        FileName      char
        ResidCalcType {mustBeMember(ResidCalcType,{'subtractPlungeZero','subtractFit'})} = 'subtractFit'
        TrimmedPlungeLengths double
        UserSelect(1,1) int8 = 0;
        dzTrim (1,1) double = 0.025;
        TrimZo(1,1) double
        TrimH(1,1) double
        PlungeFitOrder(1,1) double = 2
        ThetaShift(1,1) double
        UnwornSection(2,1) double
    end
    properties (Hidden)

    end
    properties (Constant)
        dxInterp  double = 0.1; % micrometers
        Pixels double = 1024;
        FOV    double = 420; % micrometers
        MapCrop   double = 100;
        R         double = 458.2; % tool radius in micrometers
        % deg, from maxSlope = atand(sqrt(2*doc/(R-2*doc)));
        SlopeTol  double = 8;
    end
    properties (Dependent)
        EdgeFindStartInd double
        PlungeWidths  double
    end
    properties (SetAccess = immutable)
        Nplunges   int8
    end
    properties (Access = private)
        RotCrop           = 100;
        EdgeFindStartDist = 20; % in micrometers
        EdgeFindStartSide {mustBeMember(EdgeFindStartSide,{'l','r'})} = 'l';
    end

    methods
        function obj = PlungeProcessing(inputData)
        % constructor function
        obj.Nplunges = length(inputData);
        FOV = obj.FOV;
        Pixels = obj.Pixels;
        if isstruct(inputData)
            for ii = 1:obj.Nplunges
                obj.MapData(ii) = ...
                    SurfAnalysis(inputData(ii).phaseMap, FOV/Pixels, 'm', 'um');
                obj.TraceData = SurfAnalysis([], FOV/Pixels, 'um', 'um');
                obj.ResidualData = SurfAnalysis([], FOV/Pixels, 'um', 'um');
            end
            obj.FileName = createFilename(inputData);
        else
            obj.MapData = inputData;
            obj.FileName = inputData(1).Name;
            for ii = 1:obj.Nplunges
                obj.TraceData = SurfAnalysis([], FOV/Pixels, 'um', 'um');
                obj.ResidualData = SurfAnalysis([], FOV/Pixels, 'um', 'um');
            end
        end
            obj.TrimmedPlungeLengths = nan(1, length(inputData));
            obj.DebugData = ProcessingDebug(length(inputData));
        end % constructor

        function CheckMapOrientation(obj)
            for ii = 1:obj.Nplunges
                if std(nanmean(obj.MapData(ii).PhaseMap, 2)) < 1
                    obj.MapData(ii).PhaseMap = obj.MapData(ii).PhaseMap';
                end
            end
        end % check all map orientations

        function RemovePlane(obj)
            for ii = 1:obj.Nplunges
                avgSlice = obj.MapData(ii).GetAvgSlice('col');
                % remove slope and dc bias
                % chunk of slice, the array values are in micrometers
                ind = round([10, 50]./obj.MapData(ii).dx);
                avgSlice = removeTilt(avgSlice, ind);
                if obj.UserSelect == 0
                    obj.EdgeFindStartSide = 'l';
                    efStartInd = round(obj.EdgeFindStartDist./obj.MapData(ii).dx);
                    leftEdgeInd = edgeFinder(avgSlice,...
```

```
                                obj.EdgeFindStartSide,...
                                efStartInd,...
                                obj.SlopeTol,...
                                obj.MapData(ii).dx);
            elseif obj.UserSelect == 1
                if ii == 1
                    figure('Units', 'Normalized', 'OuterPosition', [.01 .05 .95 .9]);
                end
                plot(avgSlice)
                title('Remove Plane: Select Flats');
                leftEdgeInd = round(ginput(1));
                leftEdgeInd = leftEdgeInd(1);
            end
            % instead of finding both edges, which is buggy
            % find the plunge width with sag equation
            % then add that to the left index to find the right index
            plungeWidth = ...
                round(sqrt(abs(min(avgSlice))*8*obj.R)/obj.MapData(ii).dx);
            indOffset = round(.1*length(avgSlice));
            maskInd = round([leftEdgeInd - indOffset,...
                             leftEdgeInd + plungeWidth + indOffset]);
            refSurf = SurfAnalysis();
            refSurf.PhaseMap = obj.MapData(ii).PhaseMap;
            refSurf.PhaseMap(maskInd(1):maskInd(2), :) = nan;
            fitPlane = refSurf.FitPlane();
            obj.MapData(ii).PhaseMap = ...
                obj.MapData(ii).PhaseMap - fitPlane;
        end
    end % RemovePlane

    function InterpMaps(obj)
        for ii = 1:obj.Nplunges
            obj.MapData(ii).InterpMap(obj.dxInterp);
        end
    end % interp all plunge maps

    function InterpTraces(obj)
        for ii = 1:obj.Nplunges
            obj.TraceData(ii).InterpTrace(obj.dxInterp);
        end
    end % interp all plunge traces

    function RotateMaps(obj)
        for ii = 1:obj.Nplunges
            frontSliceIndex = round(0.1*obj.MapData(ii).Ncols);
            backSliceIndex  = round(0.9*obj.MapData(ii).Ncols);
            frontSlice = obj.MapData(ii).GetSlice(frontSliceIndex, 'col');
            backSlice = obj.MapData(ii).GetSlice(backSliceIndex, 'col');
            slicePixelDist = backSliceIndex - frontSliceIndex;
            if obj.UserSelect == 0
                obj.EdgeFindStartSide = 'l';
                efStartInd = round(obj.EdgeFindStartDist./obj.MapData(ii).dx);
                frontIndex = edgeFinder(frontSlice,...
                                obj.EdgeFindStartSide,...
                                efStartInd,...
                                obj.SlopeTol,...
                                obj.MapData(ii).dx);
                backIndex = edgeFinder(backSlice,...
                                obj.EdgeFindStartSide,...
                                efStartInd,...
                                obj.SlopeTol,...
                                obj.MapData(ii).dx);
            elseif obj.UserSelect == 1
                plot(frontSlice)
                title('Rotation Front Slice');
                frontIndex = round(ginput(1));
                frontIndex = frontIndex(1);

                plot(backSlice)
                title('Rotation Back Slice');
                backIndex = round(ginput(1));
                backIndex = backIndex(1);
                if ii == obj.Nplunges
                    close(gcf)
                end
            end
            rotAngle = -atand((frontIndex-backIndex)/slicePixelDist);
            obj.MapData(ii).RotateSurf(rotAngle);
            obj.MapData(ii).PhaseMap = ...
                obj.MapData(ii).PhaseMap(obj.RotCrop:end-obj.RotCrop,...
                                         obj.RotCrop:end-obj.RotCrop);
        end
    end % rotate all maps to common coord

    function GetAvgSlices(obj)
        for ii = 1:obj.Nplunges
            obj.TraceData(ii).Trace = ...
                obj.MapData(ii).GetAvgSlice('col');
        end
    end

    function AlignPlungesTrim(obj)
```

```
            if obj.UserSelect == 1
                obj.TraceData(1).Plot()
                title('1st click = z0, |2nd click - 3rd click| = h');
                [~, zGinput] = ginput(3);
                close(gcf)
                obj.TrimZo = zGinput(1);
                obj.TrimH = abs(diff(zGinput(2:3)));
            end

            trimWidth = sqrt(8*obj.TrimH*obj.R);
            trimWidth = obj.dxInterp*round(trimWidth/obj.dxInterp);
            for ii = 1:obj.Nplunges
                % trim to common plunge width
                obj.TraceData(ii).Trace = ...
                    trimPlunge(obj.TraceData(ii).Trace,...
                                trimWidth, obj.dzTrim, obj.TraceData(ii).X, obj.TrimZo);
                % remove DC offset

                obj.TraceData(ii).Trace = obj.TraceData(ii).Trace ...
                                        - max([obj.TraceData(ii).Trace(1),...
                                               obj.TraceData(ii).Trace(end)]);

                obj.TrimmedPlungeLengths(ii) = ...
                    length(obj.TraceData(ii).Trace);
            end
        end

        function AlignPlungesSlope(obj)
                efStartInd = round(obj.EdgeFindStartDist/obj.dxInterp);

                leftInd = edgeFinder(obj.TraceData(1).Trace,...
                    'l', efStartInd, obj.SlopeTol, obj.dxInterp);
                % left and right indices for unworn index should be
                % from the edge of reference plunge
                unwornInd = obj.UnwornSection./obj.dxInterp;
                unwornRef = obj.TraceData(1).Trace(unwornInd(1):unwornInd(2));
                xResid = obj.TraceData(1).X;
                xResid = xResid(1:length(unwornRef));
                iiStart = 2;

            % use calibration found in previous step to figure out the
            % index shift needed to align everything with ref plunge
            for ii = iiStart:obj.Nplunges
                slopeResid = obj.TraceData(ii).Trace(unwornInd(1):unwornInd(2)) ...
                           - unwornRef;
                slopeTheta = polyfit(xResid, slopeResid, 1);
                indexShift = -round(slopeTheta(1)*obj.ThetaShift);
                obj.TraceData(ii).Trace = circshift(obj.TraceData(ii).Trace, indexShift);
            end
            f = sqrt(8*FakeData.PlungeDepth*PlungeProcessing.R);
            fInd = round(f/obj.dxInterp);
            % trim plunge 0 to length, use edge finder on both sides
            leftInd = edgeFinder(obj.TraceData(1).Trace,...
                'l', efStartInd, obj.SlopeTol, obj.dxInterp);
            rightInd = edgeFinder(obj.TraceData(1).Trace,...
                'r', efStartInd, obj.SlopeTol, obj.dxInterp);
            for ii = 1:obj.Nplunges
                obj.TraceData(ii).Trace = obj.TraceData(ii).Trace(leftInd:rightInd);
                obj.TrimmedPlungeLengths(ii) = ...
                    length(obj.TraceData(ii).Trace);
            end

        end

        function GetThetaShift(obj)
            % create fake plunge using obj.R and DOC = 10, dx = 0.1 um
            fakeTrace = FakeData();
            fakeTrace.CreatePlungeTrace();
            fakeTrace.InterpTrace(obj.dxInterp);
            % chop off ends
            efStartInd = round(obj.EdgeFindStartDist/fakeTrace.dx);
            % trim plunges
            leftInd = edgeFinder(fakeTrace.Trace,...
                'l', efStartInd, obj.SlopeTol, fakeTrace.dx);
            rightInd = edgeFinder(fakeTrace.Trace,...
                'r', efStartInd, obj.SlopeTol, fakeTrace.dx);
            z = fakeTrace.Trace(leftInd:rightInd);
            x = obj.TraceData(1).X(leftInd:rightInd);
            x = x - mean(x);
            shiftLim = 16;
            shiftStep = 4;
            obj.ThetaShift = calcIndexShiftVsTheta(x, z, shiftLim, shiftStep);
        end

        function FitFirstPlunge(obj, trim)
            if trim
                efStartInd = round(obj.EdgeFindStartDist/obj.dxInterp);
                leftInd = edgeFinder(obj.TraceData(1).Trace,...
                    'l', efStartInd, obj.SlopeTol, obj.dxInterp);
                rightInd = edgeFinder(obj.TraceData(1).Trace,...
                    'r', efStartInd, obj.SlopeTol, obj.dxInterp);
                z = obj.TraceData(1).Trace(leftInd:rightInd);
```

```
                x = obj.TraceData(1).X;
                x = x(leftInd:rightInd);
            else
                z = obj.TraceData(1).Trace;
                x = obj.TraceData(1).X;
            end
            [fitresult, ~] = fitCircleToTool(x,z);
            obj.PlungeZeroFit = fitresult(x)';
        end

        function CalcResiduals(obj)
            % find shortest z vector. truncate all z and x vectors to that length.
            % remove DC offset from z vectors. shift x vectors to be symmetric
            % should I reinterp all of the vectors to same length instead?
%             maxDelta = max(obj.TrimmedPlungeLengths) - min(obj.TrimmedPlungeLengths);
            minLength = min(obj.TrimmedPlungeLengths);
                switch obj.ResidCalcType
                    case 'subtractFit'
                        for ii = 1:obj.Nplunges
                            obj.ResidualData(ii).Trace = obj.TraceData(ii).Trace(1:minLength) ...
                                                    - obj.PlungeZeroFit(1:minLength);
                        end
                    case 'subtractPlungeZero'
                        for ii = 2:obj.Nplunges
                            obj.ResidualData(ii).Trace = obj.TraceData(ii).Trace(1:minLength) ...
                                                    - obj.TraceData(1).Trace(1:minLength);
                        end
                end
        end

        function PlotSlices(obj)
            figure;
            hold on;
            for ii = 1:obj.Nplunges
                obj.TraceData(ii).Plot();
            end
        end

        function PlotResiduals(obj)
            figure;
            hold on;
            for ii = 1:obj.Nplunges
                obj.ResidualData(ii).Plot();
            end
        end

        function PlotTraces(obj)
            figure;
            hold on;
            for ii = 1:obj.Nplunges
                obj.TraceData(ii).Plot();
            end
        end

        function PlungeWidths = get.PlungeWidths(obj)
            PlungeWidths = nan(1, obj.Nplunges);
            for ii = 1:obj.Nplunges
                obj.EdgeFindStartSide = 'l';
                efStartInd = round(obj.EdgeFindStartDist./obj.TraceData(ii).dx);
                leftEdgeIndex = edgeFinder(obj.TraceData(ii).Trace,...
                                           obj.EdgeFindStartSide,...
                                           efStartInd,...
                                           obj.SlopeTol,...
                                           obj.TraceData(ii).dx);
                obj.EdgeFindStartSide = 'r';
                rightEdgeIndex = edgeFinder(obj.TraceData(ii).Trace,...
                                           obj.EdgeFindStartSide,...
                                           efStartInd,...
                                           obj.SlopeTol,...
                                           obj.TraceData(ii).dx);
                PlungeWidths(ii) = abs(leftEdgeIndex-rightEdgeIndex);
            end
        end

        function FilterRawTraces(obj)
            % filters UNTRIMMED plunges
            for ii = 1:obj.Nplunges
            % find edges
            efStartInd = round(obj.EdgeFindStartDist/obj.dxInterp);
            leftInd = edgeFinder(obj.TraceData(ii).Trace,...
                    'l', efStartInd, obj.SlopeTol, obj.dxInterp);
            rightInd = edgeFinder(obj.TraceData(ii).Trace,...
                    'r', efStartInd, obj.SlopeTol, obj.dxInterp);
            % fit to data bettween edges
            x = obj.TraceData(ii).X;
            z = obj.TraceData(ii).Trace;
            % fit to plunge, ony using data between flats
            [fitresult, ~] = fitCircleToTool(x(leftInd:rightInd),...
                                             z(leftInd:rightInd))    ;
            % subtract the fit, only from data between edges
            zhat = fitresult(x(leftInd:rightInd));
            z(leftInd:rightInd) = z(leftInd:rightInd) - zhat;
```

```
            % filter this array
            z = gauss_filter_robust_1d(z, obj.dxInterp, 4, .001);
            % add the fit back to original array, between edges
            z(leftInd:rightInd) = z(leftInd:rightInd) + zhat;
            obj.TraceData(ii).Trace = z;
            end
        end

        function EdgeFindStartInd = get.EdgeFindStartInd(obj)
            mustBeNonempty(obj.EdgeFindStartDist);
            EdgeFindStartInd = round(obj.EdgeFindStartDist/obj.dxInterp);
        end
    end

end

%% helper functions for the class methods
function fname = createFilename(input_data)

% updated vesion , July 2019. splits the string using a delimiter at 'deg'
if isstruct(input_data)
    fname = strsplit(input_data(1).name, ' deg') ; % get filename from input structure
    fname = [fname{1} ' deg'];
    % parse fname for the components we care about
else
    fname = 'no struct';
end

[serial, theta, brand] = findFilenameParts(fname);
fname = strjoin({brand, serial, theta, 'deg'});

end % createFilename

function [serial, theta, brand] = findFilenameParts(str)

% find serial number
if regexp(str, '[0-9]{6,7}|unknown')
    serial = regexp(str, '[0-9]{6,7}|unknown', 'match');
else
    serial = 'serial not found';
end

% find angle experiment was performed at
if regexp(str, '\s[-]?[0-9]{1,3}([.]|pt)?[0-9]?\s')
    theta = regexp(str, '\s[-]?[0-9]{1,3}([.]|pt)?[0-9]?\s', 'match');
    theta = strrep(theta{1}(2:end-1), 'pt', '.');
else
    theta = 'unknown';
end

% find brand of tool
if regexp(str, 'K.*Y')
    brand = 'KY';
elseif regexp(str, 'ET|E.*h')
    brand = 'ET';
else
    brand = 'unknown';
end

serial = char(serial);
brand = char(brand);
theta = char(theta);

if regexp(str, 'fake data')
    serial = 'fake';
    brand  = 'fake';
    theta  = 'fake';
end

end % find filename parts

function [ ind ] = edgeFinder(z, startSide, startIndex, tol, dx)
% This function finds the left or right hand edge of any given
% "slice" of the PhaseMap data by looking for a sharp dropoff
% in z-position

step = 1;

% logic for starting the loop, based on side of plunge we want
if  startSide == 'l'
    start = startIndex            ;
elseif startSide == 'r'
    start = length(z) - startIndex;
    step  = -step                 ;
end

dz = nan(1, length(z));
for ii = 3:length(z)-2
    % 2nd order accurate finite difference for first derivative
    dz(ii) = atand((-z(ii+2) + 8*(z(ii+1) - z(ii-1)) +z(ii-2))/12/dx);
end

```

```
for ii = start:step:round(length(z)/2)
    deltaZ = dz(ii);
    % difference in z—position from point i to point i + stepSize; if statement
    % below uses this to decide where the edge is based on tol parameter
    if startSide == 'l' && deltaZ < —tol
        ind = ii;
        return
    elseif startSide == 'r' && deltaZ > tol
        ind = ii;
        return
    end
end
error('No edge found; max deltaZ found is %.2f, min is %.2f', max(dz), min(dz));
end

function z = removeTilt(z, ind)
    fs   = z(ind(1):ind(2))                              ; % fit slice
    xFit = linspace(0,length(fs),length(fs))'          ; % x array for fit
    fc   = polyfit(xFit,fs,1)                            ; % fit coefficient
    zFit = polyval(fc,linspace(0,length(z),length(z))) ; % fit polynomial
    z    = z — zFit'                                      ; % z with tilt removed
end

function zPlunge = trimPlunge(zPlunge, trimWidth, dzStep, x, z0)
% Function attempts to find f^2/8r location that is the same for all
% plunges.
% h  — height location to try and locate f at
% dz — amount to step down each loop iteration
% x  — interpolated x data from main script
% z  — interpolated z data from main script
% z0 — position on z axis to begin scanning at
pDepth = x(end)^2/8/500;
for ii = 1:round(pDepth/dzStep)
    % find first and last values in x array that correspond
    % to where z is below the current scan value
    xPair = [x(find(zPlunge < z0, 1, 'first'))  x(find(zPlunge < z0, 1, 'last'))];
    xDist = max(xPair) — min(xPair);
    % if only one value that meets the criteria is found, move down in z
    if length(xPair) == 1
        z0 = z0 — dzStep;
    % round x_dist and f to two decimal places. if x_dist is less than or
    % equal to f, then trim at this location.
    elseif round(xDist, 1) <= round(trimWidth, 1)
        zPlunge = zPlunge(x >= min(xPair) & x <= max(xPair));
        break
    end
%     ii
%     xDist
    z0 = z0 — dzStep;
end
end

function ThetaShift = calcIndexShiftVsTheta(x, z, shiftLim, shiftStep)
padArray = nan(max(shiftLim),1);
z = z';
z = [padArray; z; padArray];
x = [padArray; x; padArray];
% calculate relationship between resid
% slope and index shift
shifts = —shiftLim:shiftStep:shiftLim;
shiftResidual = nan(length(x), length(shifts));
zShift = nan(length(x), length(shifts));
pFit = nan(length(shifts), 2);

leftTrimInd = round(0.2*length(x));
rightTrimInd  = round(0.8*length(x));

for ii = 1:length(shifts)
    zShift(:,ii) = circshift(z, shifts(ii));
    shiftResidual(:,ii) = zShift(:,ii) — z;
    pFit(ii, :) = polyfit(x(leftTrimInd:rightTrimInd),...
                          shiftResidual(leftTrimInd:rightTrimInd, ii), 1);
end
ThetaShift = polyfit(shifts', pFit(:, 1), 1);
ThetaShift = 1/ThetaShift(1);
end

function [fitresult, gof] = fitCircleToTool(x, z)

    [x, z] = prepareCurveData( x, z );

    ft = fittype( '—sqrt(r^2—(x—h)^2)+k', 'independent', 'x', 'dependent', 'y' );
    opts = fitoptions( 'Method', 'NonlinearLeastSquares' );
    opts.Display = 'Off';
    opts.Lower = [—150 400 400];
    opts.StartPoint = [215 500 500];
    opts.Upper = [300 600 600];

    [fitresult, gof] = fit( x, z, ft, opts );
end
```

APPENDIX B: EXPERIMENTAL PROCEDURE

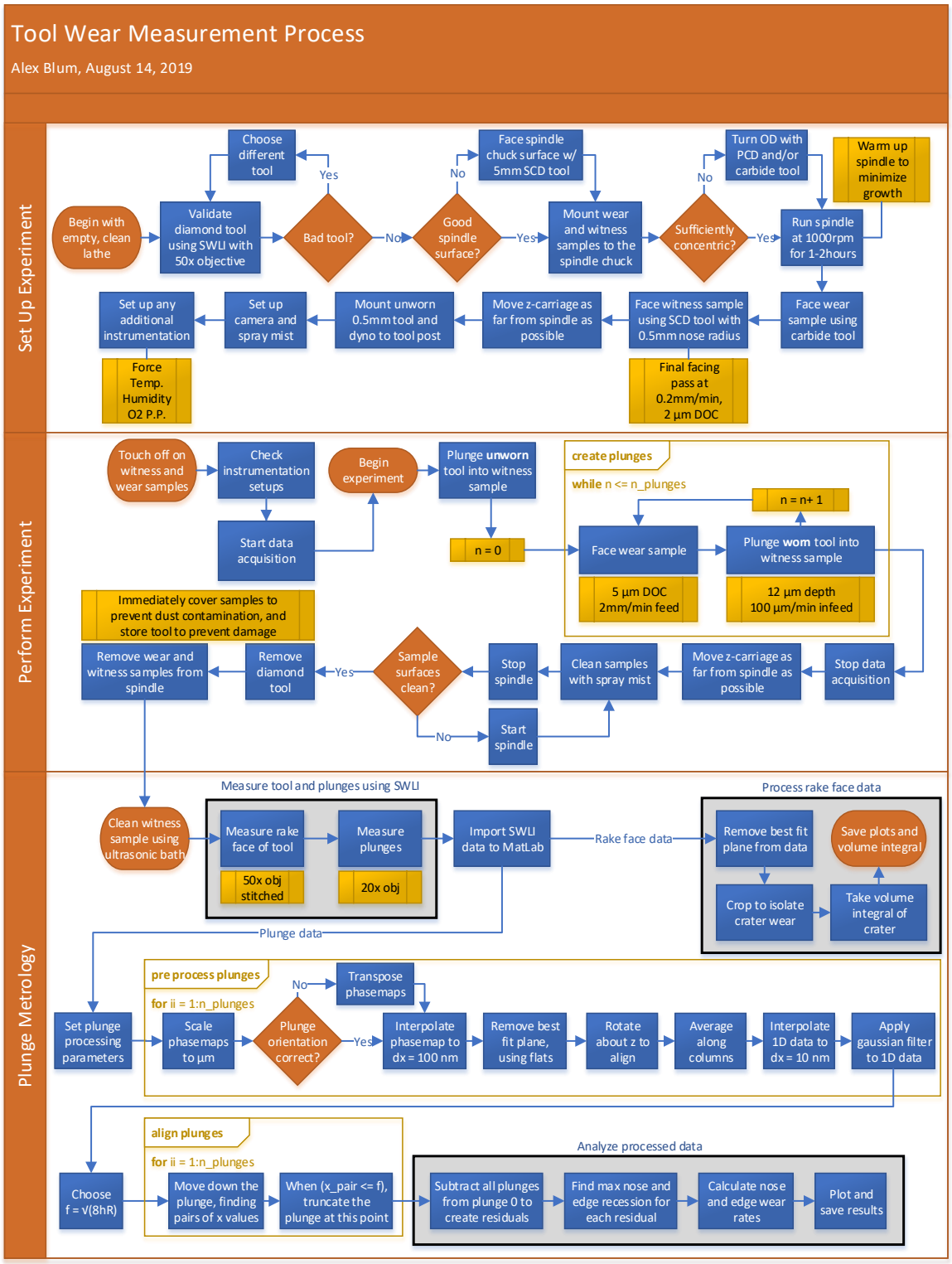

```
;written by Alex Blum
;last updated July 31, 2018
;dimensions are in mm, feeds are in mm/minute
G01 G71 G90 G40 G59

p01 = 0.440   ;distance between witness sample plunges
p02 = 0.012   ;witness sample plunge depth
p03 = 0.0     ;witness sample plunge location

p04 = 0.005   ;facing depth of cut
p05 = 0.0     ;depth of cut variable
p06 = 5       ;number of passes
p07 = 2.0     ;facing feed rate
p08 = 0.01    ;decrease p09 by this amount after each pass
p09 = 8.5     ;distance tool travels in X across wear sample
p10 = 0.0     ;holds the decremented p09

p11 = 1       ;pass counter

M04S1000      ;start the spindle

;first plunge with unworn tool
T6            ;coord system for witness sample
Z50.F1200.    ;move rapidly to Z standoff
X(p03)F1200.  ;move rapidly to X standoff
Z5.F1200.     ;rapid in Z to small standoff
Z1. F600.     ;slow down and get closer
Z.1F50.       ;much slower and even closer
Z.01F10.      ;very slow for final approach
Z(-p02)F.05   ;now down to the plunge infeed rate
G04F1.        ;dwell for one second at plunge bottom
Z.1F10.       ;retract from plunge
Z20.F1200.    ;rapid away from part in Z

WHILE (p11 !> p06)
;part one: facing the wear sample
  T7            ;coord system for wear sample
  X-.1F1200.    ;move to X standoff
  Z1.F1200.     ;move to Z standoff
  p05 = p04*p11;update depth of cut
  G59Z(-p05)    ;increment doc using tool offset
  Z0.F10.       ;moves tool to new cut depth in Z
  ;update facing distance variable
```

```
44   p10 = p09 - (p11 - 1)*p08;
     X(p10)F(p07) ;face the part
46   G59          ;clear tool offsets
     Z20.F1200.   ;back off the part
48
     ;part two:witness sample plunges
50   T6              ;coord system for witness sample
     p03 = p03 + p01;update plunge X location
52   X(p03)F1200.    ;move rapidly to X standoff
     Z5.F1200.       ;rapid in Z to small standoff
54   Z1. F600.       ;slow down and get closer
     Z.1F50.         ;much slower and even closer
56   Z.01F10.        ;very slow for final approach
     Z(-p02)F.05     ;now down to the plunge infeed rate
58   G04F1.          ;dwell for one second at plunge bottom
     Z.1F10.         ;retract from plunge
60   Z20.F1200.      ;rapid away from part in Z
     p11 = p11 + 1   ;increment pass counter
62 ENDWHILE
```

APPENDIX D: SENSORS AND DATA ACQUISITION

Table D.1: Table of sensors used during experiments and their properties.

sensor	adc (bits)	range	resolution	error (% fs)	sample rate* (hz)
capacitance probe	16	500 µm	8 nm	0.2	1000
rtd	15	?	0.03 °c	0.05	1
dynamometer	16	0-250 n	x mn	0.5	1000
o_2 sensor	?	?	100 ppm	?	0.067
microscope	n/a	10x-140x	2-30 µm/pixel	n/a	0.033